

Department of Computer Science

# Environment Awareness with Hyperspectral LiDAR Technologies

---

Yuwei Chen

# Environment Awareness with Hyperspectral LiDAR Technologies

**Yuwei Chen**

A doctoral dissertation completed for the degree of Doctor of Science (Technology) to be defended, with the permission of the Aalto University School of Science, Remote connection link (e.g. Zoom), on 24th Nov 2020

**Aalto University**  
**School of Science**  
**Department of Computer Science**

**Supervising professor**

Prof. Antti Ylä-Jääski, Aalto University, Finland

**Thesis advisor**

Prof. Juha Hyypä, Finnish Geospatial Research Institute

**Preliminary examiners**

Prof. Jouni Pulliainen, Finnish Meteorological Institute, Finland

Prof. Jonathan Li, University of Waterloo, Canada

**Opponent**

Prof. Jouni Pulliainen, Finnish Meteorological Institute, Finland

Aalto University publication series

**DOCTORAL DISSERTATIONS** 156/2020

© 2020 Yuwei Chen

ISBN 978-952-64-0076-1 (printed)

ISBN 978-952-64-0077-8 (pdf)

ISSN 1799-4934 (printed)

ISSN 1799-4942 (pdf)

<http://urn.fi/URN:ISBN:978-952-64-0077-8>

Unigrafia Oy

Helsinki 2020

Finland



Printed matter  
4041-0619

**Author**  
Yuwei Chen**Name of the doctoral dissertation**  
Environment Awareness with Hyperspectral LiDAR Technologies**Publisher** School of Science**Unit** Department of Computer Science**Series** Aalto University publication series DOCTORAL DISSERTATIONS 156/2020**Field of research** new sensing technology for environment awareness**Manuscript submitted** 12 July 2020**Date of the defence** 24 November 2020**Permission for public defence granted (date)** 19 August 2020**Language** English **Monograph** **Article dissertation** **Essay dissertation****Abstract**

LiDAR (Light Detection And Ranging, also known as LADAR) is an active optical remote sensing technique that can measure the distance by counting the time of flight (ToF) of the transmitted laser and acquire other physical properties of a target by illuminating the target with a light source, often using a pulsed laser due to the high spatial and temporal coherence nature. Traditionally a monochromatic laser beam can map physical features with a very high spatial resolution in a non-contact manner. Limited by the employed monochromatic laser source, traditional LiDAR sensors usually operate at one or several discrete wavelength bands. These systems can provide high-accuracy spatial information, but restricted spectral information: compared with a passive spectrometer, the spectral information and spectral resolution are inadequate for some particular remote sensing applications. The motivation of this research is straightforward: investigating SCL-based hyperspectral LiDAR (HSL) technology, more specifically: investigating HSL technique with different system configuration, confirming their accuracy both in spatial and spectral measurements, and conducting various feasibility studies towards environmental awareness applications, more specific, in in forestry, plant science and mining. The emphasis was on system development and methodology development. The specific aims of this dissertation based on six prototyped hyperspectral LiDAR were as follows:

- to investigate different hardware techniques including optics, electronics, and post-processing techniques for HSL system development covering the spectrum from visible to near-infrared (VNIR) to shortwave infrared (SWIR) (for better eye-safety operation) with discrete or continuous spectral channels for remote sensing applications;
- to develop methods to evaluate the performance of the HSL systems concerning the spectral measurement accuracy, the range stability and resolution over the covered spectral range ;
- to assess the feasibility of the developed methods in forestry, mining and plant sciences related environment awareness applications with the point clouds or range measurement containing the spectral information.

**Keywords** Remote Sensing, Hyperspectral LiDAR, Environment Awareness, Mining, Forestry, Plant Science**ISBN (printed)** 978-952-64-0076-1**ISBN (pdf)** 978-952-64-0077-8**ISSN (printed)** 1799-4934**ISSN (pdf)** 1799-4942**Location of publisher** Helsinki**Location of printing** Helsinki **Year** 2020**Pages** 162**urn** <http://urn.fi/URN:ISBN:978-952-64-0077-8>



# Acknowledgements

The 11 years research life of my second doctoral study is truly a long journey, far beyond my initial estimation of the difficulty for pursuing a PhD degree in the Department of Computer Science, Aalto University. During the last 11 years, there are more than thousands times I have the idea that I should quit the program. However, the generous support from good colleagues, friends and, most important, family members resulted in this thesis possible as a happy ending.

First, thanks to my instructor, Prof. Juha Hyypä, from the FGI, for guiding my research work. I was fortunate to be instructed by a world-famous scientist on laser scanning research. Prof. Juha was always there to listen to me and to give me his insight advice. His patience and support helped me to overcome many challenges not only in research but also in daily life and finish this thesis.

I owe my deepest gratitude to my supervisor, Prof. Antti Ylä-Jääski, for his advice, encouragement and support during the entire 11 years duration of my doctoral study. He was always there to provide support for every step of the way towards the completion of this thesis.

Thanks to Prof. Ruizhi Chen during my work in Department in Navigation and Positioning, Finnish Geodetic Institute. I am grateful to him for the long discussions about my career plan and also for sharing his expertise and experience.

Special thanks go to Prof. Risto Kuittinen who was the director-general of Finnish Geodetic Institute, for giving me the opportunity to work and study in FGI and experience great Finnish culture from 2005.

Thanks to Teemu Hakala, Sanna Kaasalainen, and Juha Suomalainen with whom I made my first two publications. I am grateful to them for sharing the hyperspectral LiDAR ideas with me and for igniting my work in this direction. I am also indebted to Eetu Puttonen, Changhui Jiang, and Wei Li for co-authoring the publications included in this thesis. Thanks to Prof. Chuanrong Li and Prof. Lingli Tang, for hosting my visits to the Academy of Opto-Electronics, Chinese Academy of Science and joint applications for financial support to this research in China.

I also would like to extend my thanks to Prof. Jouni Pulliainen from Finnish Meteorological Institute, Finland and Prof. Jonathan Li from the University of Waterloo, Canada, for their highly valuable comments and advice. Thanks to the previous and current staff of Department of Remote Sensing and Photogram-

metry and Department of Navigation and Positioning, Finnish Geospatial Research Institute for their help in my thesis work. Particularly, thanks to Prof. Jarkko Koskinen, Prof. Antero Kukko, Prof. Harri Kaartinen, Dr Xiaowei Yu, Dr Lingli Zhu, Ms Ziyi Feng, Prof. Ling Pei, Prof. Liang Chen, Prof. Yi Lin.

I appreciate the financial support from the Academy of Finland, Strategic Research Council at the Academy of Finland, the Chinese Academy of Science, and the Ministry of Science and Technology, China. Thanks to all teachers both in Aalto University and FGI, who cultivated my interest in learning and encouraged me to create.

Most importantly, I wish to express my gratitude to my parents for their endless support and encouragement. Especially to my father, due to some family reasons, he could not continue his study after primary school, even he was one of the best students in his class. His lifelong learning spirit encouraged me to continue my second PhD. To him, I dedicate this thesis.

Last but not least, I wish to thank my wife, Yiwu Wang. You are not only a colleague, a schoolmate but soulmate, together with Pentti and Leo.

Kirkkununmi, December 20, 2018

Yuwei Chen

Uneasy lies the head that wears a crown.

- William Shakespeare

# Contents

1.	Introduction.....	13
1.1	Motivation.....	15
1.2	Objectives of the Study and Hypothesis .....	17
1.3	Methodology of Research .....	17
1.4	Structure of the dissertation .....	18
1.5	Contributions .....	18
2.	Background and Literature Review.....	21
2.1	Forestry inventory methodology.....	23
2.2	Plant science methodology .....	26
2.3	Mining methodology.....	28
2.4	Optech Titan .....	30
2.5	Eye safety .....	33
3.	Methodology .....	35
3.1	Transmitting .....	37
3.2	Receiving.....	39
4.	Results .....	41
4.1	New HSL technology.....	41
4.1.1	Spectrograph-Based HSL .....	41
4.1.2	Optical-Filter-Based HSL.....	43
4.1.3	LCTF-based HSL.....	50
4.1.4	AOTF-based HSL .....	52
4.2	Range Results.....	54
4.2.1	Range results of optical-filter-based systems .....	56
4.2.2	LCTF-based HSL.....	58
4.2.3	AOTF based HSL.....	59
4.3	Spectral Results.....	60
4.3.1	Forestry inventory.....	62
4.3.2	Plant Science .....	65
4.3.3	Mining .....	72
5.	Discussion.....	77

5.1	More outputs .....	79
5.2	The Goal of the Dissertation.....	83
5.3	Future Research.....	84
6.	Summary .....	87

# List of Abbreviations and Symbols

AC	Alternating Current
A/D	Analogue-to-Digital
ADC	Analogue-to-Digital Converter
ALS	Airborne Laser Scanning
AOTF	Acousto-Optic Tunable Filter
AOE	Academy of Opto-Electronics
APD	Avalanche Photodiode
AVHRR	Advanced Very-High-Resolution Radiometer
AVIRIS	Airborne Visible and Infrared Imaging Spectrometer
CAS	Chinese Academy of Sciences
CCD	Charge-Coupled Device
CNSA	China National Space Administration
DGPS	Differential Global Positioning System
DOMs	Digital Orthophoto Maps
DSM	Digital Surface Models
FCD	Feature Contribution Degree
FGI	Finnish Geospatial Research Institute
FOV	Field of View
FRS	First-order Reflectance Slope
FWHM	Full Width at Half Maximum
GPS	Global Positioning System
GNSS	Global Navigation Satellite System
HgCdTe	Mercury Cadmium Telluride

HSL	Hyper-Spectral LiDAR
IMU	Inertial Measurement Unit
InGaAs	Indium Gallium Arsenide
LCTF	Liquid Crystal Tunable Filter
LET	Linear Extrapolation Technology
LFPIIT	Linear Four-Point Interpolation Technology
LiDAR	Light Detection and Ranging
LOLA	Lunar Orbiter Laser Altimeter
LSB	Least Significant Bit
LWIR	Longwave Infrared
MIR	Middle-Infrared
MLS	Mobile Laser Scanner
MSLS	Multi-Spectral Laser Scanner
MOF	Micro-structured Optical Fibre
NASA	National Aeronautics and Space Administration
NEAR	Near-Earth Asteroid Rendezvous
NOAA	National Oceanic and Atmospheric Administration
Nd:YAG	Neodymium-doped Yttrium Aluminium Garnet
NDVI	Normalized Difference Vegetation Index
PMT	Photomultiplier Tube
REA	Red-Edge Area
REP	Red-Edge Position
RES	Red-Edge Slope
RMSE	Root Mean Square Error
RTK	Real-time Kinematic
SAR	Synthetic Aperture Radar
SCL	Supercontinuum Laser
SLAM	Simultaneous Localization and Mapping
SNR	Signal-to-Noise Ratio
STD	Standard Deviation
SVM	Support Vector Machine

SWIR	Shortwave Infrared
TLS	Terrestrial Laser Scanning
ToF	Time of Flight
VNIR	Visible and Near-Infrared
VRS	Virtual Reference Station



# List of Publications

This doctoral dissertation consists of a summary and of the following publications which are referred to in the text by their numerals

- 1.** Chen Yuwei , Rääkkönen Esa, Kaasalainen Sanna, Suomalainen Juha, Hakala Teemu, Hyyppä Juha, and Chen Ruizhi. "Two-channel hyperspectral LiDAR with a supercontinuum laser source." *Sensors* 10, no. 7 (2010): 7057-7066. DOI:10.3390/s100707057
- 2.** Hakala Teemu, Suomalainen Juha, Kaasalainen Sanna, and Chen Yuwei. "Full waveform hyperspectral LiDAR for terrestrial laser scanning." *Optics Express* 20, no. 7 (2012): 7119-7127. DOI:10.1364/OE.20.007119
- 3.** Wang Zhen, Chen Yuwei, Li Chuanrong, Tian Mi, Zhou Mei, He Wenjing, Wu Haohao, Zhang Huijing, Tang Lingli, Wang Yiwu, Zhou Hui, Puttonen, Eetu, Hyyppä Juha. "A Hyperspectral LiDAR with Eight Channels Covering from VIS to SWIR." In *IGARSS 2018-2018 IEEE International Geoscience and Remote Sensing Symposium*, pp. 4293-4296. IEEE, 2018. DOI: 10.1109/IGARSS.2018.8517741
- 4.** Chen Yuwei, Jiang Changhui, Hyyppä Juha, Qiu Shi, Wang Zhen, Tian Mi, Li Wei, Puttonen Eetu, Zhou Hui, Feng Ziyi, Yuming Bo, Zhijie Wen. "Feasibility study of ore classification using active hyperspectral LiDAR." *IEEE Geoscience and Remote Sensing Letters* 15, no. 11 (2018): 1785-1789. DOI: 10.1109/LGRS.2018.2854358
- 5.** Li Wei, Jiang Changhui Jiang, Chen Yuwei, Hyyppä Juha, Tang Lingli Tang, Li Chuanrong, and Wang Shao Wei. "A Liquid Crystal Tunable Filter-Based Hyperspectral LiDAR System and Its Application on Vegetation Red Edge Detection." *IEEE Geoscience and Remote Sensing Letters* 16, no. 2 (2018): 291-295. DOI: 10.1109/LGRS.2018.2870143
- 6.** Chen Yuwei, Li Wei, Hyyppä Juha, Wang Ning, Jiang Changhui, Meng Fanrong, Tang Lingli, Puttonen Eetu, and Li Chuanrong. "A 10-nm spectral

resolution hyperspectral LiDAR system based on an acousto-optic tunable filter." *Sensors* 19, no. 7 (2019): 1620. DOI:10.3390/s19071620

Additional publications by the author that touch upon the topic of this dissertation include those on microwave remote sensing, seamless navigation and positioning. They are cited where appropriate in this dissertation. The total publication number during this doctoral study is more than 120. As of 28 May 2019, the papers of the author have received 2269 citations in Google Scholar. As of the same date, paper 2 has received 181 citations, and paper 1 has received 77 citations. Others are too recent that the numbers of citations are not relevant.

# Author's Contribution

## **Publication 1:** “Two-channel Hyperspectral LiDAR with Supercontinuum Laser Source”

The author was one of the major contributors to conceptualizing the paper under extensive help from co-authors. The author carried out the field test and set up the two-channel hyperspectral LiDAR (HSL) system together with co-authors. He analysed the collected waveforms for Norway spruce and standard reflection board and carried out object discrimination with the normalized difference vegetation index (NDVI) parameter extracted from the collected waveform.

## **Publication 2:** “Full Waveform Hyperspectral LiDAR for Terrestrial Laser Scanning”

The author was involved in system integration, especially electronics design and participated in writing the paper. The research demonstrates the 3D point clouds with backscattered reflectance and spectral indices collected from a Norway spruce with an 8-channel full-waveform terrestrial hyperspectral LiDAR.

## **Publication 3:** “A Hyperspectral LiDAR with Eight Channels Covering from VIS to SWIR”

The author was the primary contributor to the conceptualization of the paper with the co-authors and emphasized that spectral coverage in the shortwave infrared (SWIR) band was essential for further applications. The author applied joint international cooperation funding to initialize the hyperspectral LiDAR research in the Academy of Opto-Electronics, Chinese Academy of Science. He designed the laboratory conditions and instructed young scientists.

## **Publication 4:** “Feasibility Study of Ore Classification Using an Active Hyperspectral LiDAR”

The author proposed the concept of optical filter-based HSL for ore classification, especially in the shortwave infrared band. A seventeen-channel HSL based on an optical filter group was designed and tested for that application. The field test was carried out by the author together with co-authors, and the author also proposed and fulfilled the support vector machine (SVM)-based ore classification method and wrote the whole paper with contributions from all the co-authors.

**Publication 5:** “A Liquid Crystal Tunable Filter-Based Hyperspectral LiDAR System and Its Application on Vegetation Red Edge Detection”

The author proposed the concept of using Liquid Crystal Tunable Filter-based Hyperspectral LiDAR for agriculture applications, more specifically, red-edge detection together, with the co-authors. And he carried out the field tests and analysis of the data together with the developed prototype LiDAR system enabling 17 continuous spectral channels with a 10-nm spectral resolution from 500 nm-670 nm. In addition, he jointly wrote the paper with the first author.

**Publication 6:** “A 10 nm Spectral Resolution Hyperspectral LiDAR System Based on Acousto-optic Tun-able Filter.”

The key idea was developed primarily by the author with help from the co-authors. The author proposed the concept of acousto-optic tunable filter based Hyperspectral LiDAR to obtain continuous spectral data covering the 500-1000-nm spectral range. He described the principle and advantages of this novel solution and evaluated the performance both in range stability and spectral measurement and wrote the whole paper with contributions from all the co-authors.

# 1. Introduction

LiDAR (Light Detection And Ranging, also known as LADAR) is an active optical remote sensing technique that can measure the distance by counting the time of flight (ToF) of the transmitted laser and acquire other physical properties of a target by illuminating the target with a light source, often using a pulsed laser due to the high spatial and temporal coherence nature. A monochromatic laser beam can map physical features with a very high spatial resolution in a non-contact manner. Thus LiDAR can be used to target a wide range of materials, including metallic and non-metallic objects, vegetation, rocks, rain, chemical compounds, aerosols, clouds and even single molecules and the traditional LiDAR technology is applied in various fields, such as agriculture, transportation, autonomous vehicles, geomatics, forestry, archaeology, geography, geology, mining, rock mechanics, seismology, remote sensing, military and atmospheric physics.

LiDAR technology originated in the early 1960s shortly after the first laser was built in 1960. Then the public became aware of the accuracy and usefulness of LiDAR gradually. Various LiDAR ranging systems were developed for aircraft and spacecraft as well as for such non-aerospace conveyances for both military and non-military units. Commercial altitude measuring systems were flown by aeroplanes, and airborne commercial LiDAR systems for ground surveying have been extensively used ever since. LiDAR can also be used to accurately track satellites and space vehicles from the earth by the installed retroreflective prisms or retroreflectors, which provides distance measurements of millimetre-level precision. Since the installation of a retroreflector array by the crew of Apollo 11, we can track the moon with greater range accuracy, providing highly accurate measurements and a better understanding of the dynamics of the Earth/Moon system.

During the Apollo 15 mission of National Aeronautics and Space Administration (NASA) in 1971, a laser altimeter was used to map the topography of the moon by measuring the altitude of the Apollo vehicle from the moon's surface, and basic knowledge about geometry information about the moon was derived afterwards (Kaula et al., 1973; Sjogren and Wollenhaupt, 1973). After that, the laser altimeter became a "standard" payload for lunar missions and missions of exploring other planets to determine their surface topography, such as Clementine (Williams et al., 1998), CE (Chang'E) series spacecraft (Zhang et al., 2006; Wang et al., 2010; Zhao et al., 2014), SELENA (Araki et al., 2009), Chandrayaan-1 (Goswami et al., 2009; Kamalakar et al., 2010), Lunar Orbiter Laser

Altimeter (LOLA) (Smith et al., 2017), and NLA in the Near-Earth Asteroid Rendezvous (NEAR) mission for asteroid detection (Cheng et al., 2000). Both NASA and the China National Space Administration (CNSA) have identified LiDAR as a critical technology for hazard avoidance and enabling the safe landing of future robotic and crewed lunar-landing vehicles with autonomous precision (Johnson et al., 2001; Amzajerdian et al., 2011). Furthermore, Chinese scientists have successfully employed the LiDAR supported autonomous safe landing both in CE-3 and CE-4 missions (Wan et al., 2013; Zhou et al., 2017).

In addition to spaceborne altimeters, NASA and other organizations have initialized several airborne LiDAR systems for measuring various terrains, such as sea ice, to fully utilize the range capability for pilot research (Ackerman et al., 1967; Link 1969; Tooma and Tucker 1971). The accuracy and ease of use of airborne LiDAR systems for topography and hydrography were preliminarily demonstrated. Due to the missing of reliable and robust positioning technology until the early 1990s, non-scanning profiling LiDAR was used for meteorology, bathymetry, forestry and other environmental applications ever since. (Fredriksson et al., 1981; Nelson et al., 1984; Schreier et al., 1985; Muirhead and Cracknell 1986).

Generally, a typical LiDAR system consists of 1) a monochromatic laser source, 2) transmitting and receiving optics, 3) photodetector(s) and receiver electronics, and 4) an optional optomechanical scanner. Usually, a monochromatic laser source from 500-1100 nm is common for various applications with more advanced detector technology, such as silicon avalanche photodiode (APD) detectors. However, the maximum transmitted power of the laser source should be considered for eye safety issues. In general, the 1550-nm laser is a common alternative. The wavelength higher than 1.4  $\mu\text{m}$  is eye-safe at relatively higher power levels (approximate two to three orders of magnitude higher) since such a wavelength is not strongly absorbed by the tissue of eyes, which operates in the infrared spectrum at a relatively long wavelength that allows for longer ranges. However, the detectors operating that spectrum process less sensitive, for example, indium gallium arsenide (InGaAs) APD detectors. Other laser settings include the laser repetition rate, which determines the data collection speed and operation efficiency (without a beam splitter), and the pulse width, which controls the range resolution (a shorter width for better range resolution), provided that the photodetector and electronics have sufficient bandwidth (generally a few hundred MHz). Transmitting and receiving optics designs affect the angular resolution of the system and the maximum range that can be detected. A Cassegrain telescope and a parabolic mirror are options for collecting reflected optical signals that are sensed and converted into electric signals by high-speed photodetectors. Various photodetector technologies, such as photodiodes, APD, and photomultipliers (PMT), are utilized for receiver electronics to determine the range. The scanning mechanism is optional to steer laser beams to targets and mainly determines the sensing scope for each application.

The full operation of global positioning system (GPS) and other global navigation satellite systems (GNSSs) and the development of inertial sensors at the

1990s made that the absolute position and orientation measurement by the sensors easy to use, which triggered the increased development of the laser scanning technique. Supported by advanced GNSS technologies, such as differential global positioning system (DGPS), real-time kinematic (RTK) and virtual reference station (VRS), decimetre- or even centimetre-level absolute position accuracy can be achieved. The prototypes of commercial airborne laser scanning (ALS) dedicated to topographic mapping was introduced afterwards. Supported by a position and orientation unit and an optomechanical scanner, 1) a range is established by measuring the ToF and multiplying it by the speed of light as a constant with a LiDAR unit; 2) an orientation measurement is determined by the roll, pitch, and heading measurements observed by an inertial measurement unit (IMU) and the angular output of the optomechanical scanner; 3) an absolute position in the global coordinates of the laser scanner observed by GNSS. Based on the range, orientation and position measurements, the positioning of the target can be accurately calculated. As a result, the output of the ALS is a georeferenced point cloud in three dimensions, representing the geometry of ground targets (e.g., objects, vegetation, plants, buildings and landscapes) together with intensity information at the selected wavelength and possibly waveform information of the returned echoes (Wehr and Lohr, 1999). In addition to ALS, the laser scanner can be installed on a tripod to scan the nearby environment, which is called terrestrial laser scanning (TLS), or on a kinematic platform, such as a vehicle or a vessel, which is called mobile laser scanning (MLS). Both TLS and MLS become a more accessible technology in the last two decades for various close-range three-dimensional related application. Combined with the altitude measurements of the IMU and the absolute position collected by GNSS, the MLS can generate an accurate geospatial point cloud  $(x, y, z)$  of the surveyed target area with an accuracy of tens of millimetres when the GNSS observation condition is good (Kaartinen, 2013). The intensity value of echoes is also recorded for each point, either as an amplitude. As a result, the intensity or amplitude is proportional to the number of photons received by the detector of the system over a given period, or as the complete echo waveform recorded by a high-speed digitizer or an analogue-to-digital converter (ADC). As a result, the point cloud  $(x, y, z, R(\lambda))$ , where  $R(\lambda)$  is the backscattered reflectance  $R$  at the monochromatic laser operating wavelength  $\lambda$ , can be generated.

All applications mentioned above follow the same basic physical principle with slight variations. It is possible to measure the distance, position, and velocity with extreme precision by transmitting a monochromatic, high-power and low-divergence laser beam out, reflecting it, and detecting its return echoes using a photodetector.

## 1.1 Motivation

Limited by the employed monochromatic laser source, traditional LiDAR sensors usually operate at one or several discrete wavelength bands (Wang and Philpot 2007; Wang et al., 2014; Douglas et al., 2015; Fernandez et al., 2016).

Typical commercial products of multiple wavelengths LiDAR are the SHOALS system (Irish et al., 1999; Wang et al. 2007) and Titan multispectral mapping LiDAR (Van Rees 2015; Matikainen et al., 2017). The SHOALS is mainly used for coastal area mapping, is known as bathymetric LiDAR, and the system consists of wavelengths of 1064 nm (infrared) and 532 nm (green) with a pulse width of ~6 ns and a pulse repetition rate of 400 Hz. Two laser beams are projected onto a fast-rotating mirror, which creates a circular pattern of points on the sea surface. One of the beams (green) penetrates the seawater and detects the bottom surface of the water under favourable conditions, and another one (infrared) measure the sea surface. Titan was the first multispectral commercial system developed by Optech, combining three wavelengths (532, 1,064 and 1,550 nm) into a single system framework with a maximum laser measurement rate of 300 kHz per channel. These systems can provide high-accuracy spatial information, but restricted spectral information: compared with a passive spectrometer, the spectral information and spectral resolution are inadequate for some particular remote sensing applications. A point cloud containing accurate spatial information with abundant spectral profiles can contribute to a more efficient object classification than the traditional LiDAR sensors operating with a single-wavelength laser source.

With the rapid technological advances in fibre optics, commercial supercontinuum laser (SCL) sources were created and could transmit coherent broadband laser pulses with wavelengths ranging from 450 nm to 2400 nm (Tabirian et al., 2003; Hakala et al., 2012; Puttonen et al.,2015). The motivation of this research is straightforward: investigating SCL-based hyperspectral LiDAR (HSL) technology, more specifically: investigating HSL technique with different system configuration, confirming their accuracy both in spatial and spectral measurements, and conducting various feasibility studies towards environmental awareness applications.

Compared with passive optical remote sensing, active LiDAR remote sensing technology is different. Firstly, in passive optical remote sensing, sunlight or other light sources provide illumination to the target, and the light sources are usually a continuum in the spectral domain. In LiDAR remote sensing, the spectral channel configuration of the system is determined by the employed laser sources. Secondly, multispectral passive remote sensing works with 2-10 spectral channels, whereas hyperspectral refers to the number of channels exceeding 10. With LiDAR, similar separation is not applied. A laser is usually a monochromatic light source due to its unique physical nature.

In this dissertation, the multispectral LiDAR has been defined as a LiDAR system employing multiple monochromatic laser sources, whereas the hyperspectral LiDAR refers to a LiDAR system employing supercontinuum laser source, which is also the scope of this dissertation. However, these separations have not officially been confirmed in other related publications.

## 1.2 Objectives of the Study and Hypothesis

The primary objectives of the research, conducted during 2010-2018, was to develop various hyperspectral LiDAR techniques for environmental awareness using an SCL as a light source and to evaluate the feasibility of the developed method in its application, more specifically in forestry, plant science and mining. The emphasis was on system development and methodology development. The specific aims of this dissertation were as follows:

- to investigate different hardware techniques including optics, electronics, and post-processing techniques for HSL system development covering the spectrum from visible to near-infrared (VNIR) to shortwave infrared (SWIR) (for better eye-safety operation) with discrete or continuous spectral channels for remote sensing applications;
- to develop methods to evaluate the performance of the HSL systems concerning the spectral measurement accuracy, the range stability and resolution over the covered spectral range ;
- to assess the feasibility of the developed methods in forestry, mining and plant sciences related environment awareness applications with the point clouds or range measurement containing the spectral information.

Based on these specific objectives, the primary hypotheses of the study are as follows:

- HSL system with satisfactory range stability and spectral measurement accuracy for sensing the environment can be accomplished by latest developed techniques in electronics, optics and data processing to generate the spatial point cloud containing extensive spectral information with a single instrument.
- Combining with spatial information due to the range capability of LiDAR, the spectral information derived from the same HSL is feasible for the application on forestry, mining and plant science.

## 1.3 Methodology of Research

Over the last few decades, LiDAR has become an accessible technology for the direct acquisition of geospatial information. With the increasing utilization of this technology in various applications ranging from space exploration missions, agriculture, archaeology, atmosphere, forestry, biology, geology, and physics, its ability to collect topographic data has been thoroughly investigated.

It is straightforward if a LiDAR can transmit a “white” laser that contains multiple wavelengths; then, the generated point clouds will contain a multispectral presentation of targets and will provide many spectral features, which will undoubtedly be beneficial for further processing, for example, in classification. However, the so-called “white” laser concept contradicts the nature of the temporal coherence for laser. In this research, an SCL source is used to generate ultra-wideband laser pulses ranging from 400 nm to 2400 nm (Tabirian et al., 2003; Buchter et al. 2004 and 2011). Based on the latest developed SCL source, six different HSLs with different spectroscopic devices are proposed, designed and tested with feasibility studies. Among these HSLs, the number of channels

increases from two to eight to seventeen and finally to fifty-one channels; the ranging distance increases from several metres to several tens of metres, even close to one hundred metres. The spectroscopic devices utilized in this research are optical filters (Publications I, III, and IV), a spectrograph (Publication II), a liquid crystal tunable filter (LCTF) (Publication V) and an acousto-optic tunable filter (AOTF) (Publication VI).

## 1.4 Structure of the dissertation

This dissertation consists of a summary and six original publications. In Chapter 2, the background of the LiDAR system and the state-of-the-art technology combining active LiDAR with passive hyperspectral imagers and the multispectral LiDAR are generally reviewed with restricted scopes of three primary research directions: forestry, plant science, and mining. The methods employed in this dissertation are summarized in Chapter 3. In Chapter 4, the results of the original publications are summarized. The discussion, conclusions and future directions are presented in Chapter 5, and finally, Chapter 6 presents the summary

## 1.5 Contributions

In general, there is considerable interest in the scientific research community in novel active remote sensing approaches, of which one possible approach combining the capabilities of collecting spatial and spectral information of the environment within a single framework, namely, HSL technology, is extensively investigated in this research. Automation in point cloud classification supported by additional spectral information collected by HSL might trigger a revolution in context awareness and environmental awareness and understanding. The primary contributions of this dissertation are novel proposals for various HSL solutions. We present HSL technology with different spectroscopic devices, different electronics using SCL as a light source and evaluate the feasibility of the developed method in environmental awareness applications.

The number of channels of the HSL described in this dissertation increases from 2 (Publication I) to 8 (Publication II, III), 17 (Publication IV), 18 (Publication V), and 51 (Publication VI) using different spectroscopic devices, more specific, optical filters (Publications I, III, and IV), a spectrograph (Publication II), an LCTF (Publication V) and an AOTF (Publication VI). In our latest published paper, the number of channels increases to 91 with continuous spectral coverage (Shao et al., 2019) with the AOTF device. The spectral resolution increases from 40 nm to 5 nm. The research gradually starts from a less discrete spectral channel to a more discrete spectral channel (Publications I, II, III, and IV) to continuous spectral coverage (Publications V and VI). The investigated spectral ranges

from VNIR (Publications I, II, V, and VI) to SWIR (Publication III, IV). The capability of HSL for object classification generally increases with higher spectral and spatial resolutions, and the latest developed HSL can provide 91 spectral bands with a spatial resolution of  $0.4 \text{ milliradian} \times \text{range}$ . The spatial resolution can be further improved with an optimized design for the optical sub-systems (Shao et al., 2019).

To be more specific, the contribution of each publication is as follows.

Publication I presented the world's first two-channel, spectral-range-finding system based on an SCL source and using optical filters as the spectroscopic component. The prototype system was built using commercial components. Moreover, besides the range accuracy evolution of the prototyped system, it was used to determine its potential application in distinguishing the normalized difference vegetation index (NDVI) for Norway spruce, a coniferous tree, with a standard reflection board by the collected waveforms at 600 nm and 800 nm.

Publication II extended the aforementioned two-channel system into an eight-channel system covering the VNIR spectrum by using a spectrograph as the spectroscopic component. It presented the design of the world's first full-waveform HSL and the first demonstrations of its application in remote sensing. 3D point clouds with backscattered reflectance and spectral indices were presented for a specimen of Norway spruce to demonstrate the potential of the instrument in the remote sensing of forestry.

In Publication III, an eight-channel HSL covering the VNIR-to-SWIR spectrum was reported. The echoes of the HSL signals were divided into two sections and were detected by the different optoelectronic devices. The HSL detection experiment was carried out in the laboratory, and the accuracy of the spectral measurement of the HSL was evaluated by comparing with the reference spectrum collected by a spectrometer.

Publication IV extended the eight-channel HSL covering the VNIR-to-SWIR spectrum in Publication III into seventeen channels version, and the spatial and spectral information of seven different ore samples were obtained under a controlled laboratory environment using seventeen channels HSL. We investigated the feasibility of the ore classification application using spectral measurements with multiple support vector machine (SVM) classification methods, and the results were promising.

In Publication V, an eighteen-channel HSL with a 10-nm spectral resolution and continuous spectral coverage from 550 nm - 720 nm was designed and tested, in which an LCTF was installed before the APD detector to continuously select the wavelength of the backscattered echoes in the temporal dimension. The laboratory experiments for vegetation red-edge detection were investigated with the prototype HSL to assess its feasibility in plant science applications. The HSL equipped with LCTF, called as LCTF-HSL in the rest of the dissertation, measured yellow and green leaves from aloe and dracaena plants for detecting the corresponding "red edge position" against the referenced spectral profiles measured by an SVC® spectrometer.

In Publication VI, a tunable HSL technology using an AOTF as the spectroscopic device was proposed, designed and tested. By tuning the spectroscopic

device in the temporal dimension, the proposed AOTF-based hyperspectral LiDAR, called AOTF-HSL in the rest of the dissertation, can achieve backscattered echoes with continuous coverage of the spectrum of VNIR, more specific, 500-1000 nm, which has the unique characteristics of a continuous spectrum in the VNIR regions with a 10-nm spectral resolution. Both the general range precision over the covered spectral range and accuracy of spectral measurement were evaluated.

## 2. Background and Literature Review

LiDAR instruments utilise the extreme directionality of laser light, which enables the measurement of distances with high spatial accuracy with a monochromatic laser source. Traditionally, intensity data have mainly been used for matching images and laser strips and the rough classification and recognition of points and objects after radiometric calibration. Some advanced LiDARs have the capability of full-waveform analysis by extracting the range information and additional attributes of targets from digitised echo signals. A full-waveform analysis is carried out during post-processing on the digitised echo signals from a LiDAR instrument during data acquisition on a high-speed data recorder. Thus, the inherent Least Significant Bit (LSB) error of an analogue-to-digital (A/D) converter for digitising the waveform is inevitable during data acquisition.

LiDAR measures the range to a target by illuminating the target with laser light and measuring the reflected echo with a sensor, similar to sonar and radar but with light. Two kinds of LiDAR detection schemes are usually utilised: "incoherent" and direct energy detection, which principally measures amplitude changes in the reflected light, and coherent detection, which principally measures changes in the phase of the reflected light. In this paper, we mainly discuss the direct energy detection scheme. The principle of LiDAR is straightforward: it transmits a pulse of laser and records the returned pulse of the laser, substrates the recorded time to calculate the ToF. Differences in the range measurement can be used to build digital 3D representations of the target. It can record the geospatial environment at speeds of thousands to millions of points per second by recording the target position together with the intensity of the selected wavelength.

HSL possesses the advantages of both range detection embodied by traditional single-wavelength LiDAR and hyperspectral detection capability, by detecting ranging and spectral information synchronously with a single HSL system. Due to its unique optical-mechanics design, data registration between the range measurement and spectra is totally avoided, which prevents complex data fusion between a spectral sensor and a spatial sensor.

To achieve hyperspectral recording of return laser signals, scientists traditionally utilise fusion technique to combine the spatial measurements with spectral measurement collected by different remote sensing payloads. For example, combine the laser-scanner derived point cloud with passive spectrometry collected by aerial images or passive imaging spectrometry (Glenn et al., 2008).

Academy of Opto-Electronics (AOE) of Chinese Academy of Sciences (CAS) proposed and designed an airborne remote sensing instrument to combine active push-broom style LiDAR and passive spectrometric imaging sensors by sharing the same optical system to generate 3D spectral images (Chen et al., 2004; Li et al., 2013). However, In addition to a complex data processing to combine two datasets from active and passive sensors, the spectrometry is not immune to changes in the illumination conditions and has a reduced capability to preclude the shadow region. Because the spectrometric images were generally collected in a passive manner which detects natural energy that is reflected from the observed scene, and the variance of natural energy would inevitably affect the final detection results (Zhang et al., 2015).

Using separated semiconductor laser diodes as the laser source is another traditional technique for producing 3D point clouds with limited spectral intensity information (Erdody et al., 2010) and SHOALS is a very typical system dedicating for coastal area mapping application (Irish et al., 1999; Wang et al. 2007). Wang et al. (2014) investigated the potential of using dual-wavelength (1064nm and 1550nm) airborne LiDAR data to classify land cover: Optech ALTM Pegasus HD400 LiDAR offered the point cloud data at 1064 nm while Riegl LMS-Q680i offer the point cloud in middle-infrared (MIR). An SVM was used to classify six types of suburban land cover: road and gravel, bare soil, low vegetation, high vegetation, roofs, and water bodies. Results show that using dual-wavelength LiDAR-derived information could compensate for the limitations of using single-wavelength LiDAR information. Eitel et al. (2014) assessed the crop foliar nitrogen using a tractor-mountable, dual-wavelength laser system with separate laser sources (green 532 nm and red 658 nm). Douglas et al. (2015) designed a dual-wavelength LiDAR to record the full-time series of returns at a half-nano-second sampling rate from two co-aligned 5-ns pulsed lasers at 1064 and 1548 nm wavelengths for the characterisation of fine-scale forest structure and biomass content. Muller and Yuen (2008) analysed the possibility of multispectral point cloud data acquisition by using two monochrome laser sources operating at 532 nm and 1064 nm based on simulation, and two narrow-band optical filters were used to separate the spectral echoes that were acquired by APD sensors (Muller and Yuen, 2008). Morsdorf et al. (2009) also conducted simulations on multispectral full-waveform canopy LiDAR to assess both the structural and physiological information. The research team at the University of Edinburgh proposed a 4-wavelength multispectral canopy LiDAR system with four lasers operating in the green, red and near-infrared wavelengths (531 nm, 550 nm, 660 nm and 780 nm) for virtual forest monitoring. The designed 4-wavelength multispectral LiDAR system was used to detect the normalised difference vegetation index (NDVI) and other spectral indices, for vegetation detection (Woodhouse et al., 2011). Gong et al. (2012) also developed a multi-wavelength canopy LiDAR prototype, which operates at multiple wavelengths covering the spectrum range most sensitive to retrieving vegetation characteristics. They employed four wavelengths system configuration covering three visible light bands (556, 670, and 700 nm) and one infrared light band (780 nm) by synthesising four semiconductor laser diodes into a single beam. The developed prototype is

mainly used for vegetation remote sensing and object classification (Gong et al., 2015; Chen et al., 2017). Such a multispectral laser scanner (MSLS) system is a combination of several standalone LiDARs operating at different wavelengths, sharing the optical system. The advantage of multiple laser-based solutions is that the system can be quickly built with commercial products for proof-of-concept studies, and another significant advantage is eye safety, which is the primary concern of using white/supercontinuum laser. However, the disadvantages are also obvious: 1) the availability of monochrome laser source restricts the spectral band; 2) the laser-emitting system becomes bulky when the number of channels increases; 3) the synthesis from multiple laser sources into a single beam requires considerable efforts on the system design, especially when more spectral bands are anticipated and the overall laser source diversity increases. Such technical restrictions might explain why there are no multiple laser-based MSLSs with more than four spectral channels.

The supercontinuum light source was patented in 2003 (Tabirian et al. 2003). The ideas leading to hyperspectral LiDAR were published in Kaasalainen et al. (2007b). Chen et al. (2010) (author) implemented the first two-channel hyperspectral LiDAR prototype and performed the first tests with forestry inventory application.

In the following literature review, the author mainly investigates state-of-the-art remote sensing methods in forestry inventory, plant science and mining with either standalone passive hyperspectral/multispectral imaging technique or active ranging technology, such as single-wavelength LiDAR and microwave radar, or by fusion of laser scanning and hyperspectral imaging data from two separated sensors.

## 2.1 Forestry inventory methodology

Airborne photogrammetric methods have inventoried forests since the 1940s. However, such visual interpretation based on expertise is time-consuming and expensive. Commonly, different tree species have similar spectral and/or spatial features (Puttonen E. 2012). There is a trade-off between the spectral and spatial performance depending on the camera used, and most beneficial approaches have often combined image information with data from other sources, for example, data from multiple spectral or hyperspectral imagers (Meyera et al., 1996; Martin et al., 1998; van Aardt 2000; Zhu et al., 2014). Spectral imagery is also extensively utilised to investigate forest canopy reflectance and in modelling (Jacquemoud et al., 2000; Rautiainen et al., 2009). Both the biochemical and biophysical components of a forest can be extracted and mapped from spectral information (Schlerf et al., 2005; Kokaly et al., 2009). Passive optical remote sensing systems mainly collect the reflected nature energy (sunlight) from the exterior canopy surface and are almost unable to acquire the information inside the canopy due to topographical occlusion. Various restrictions, such as the limited employed spectral range, and the variance and reduced illumination conditions generally pose a negative impact on final inventory performance.

ALS data has become increasingly available since the early 1980s, and some pilot studies have been carried out to investigate the height profiles, tree heights, stem volumes and biomass in the case studies (Nelson et al., 1984; Aldred et al., 1985; Schreier et al., 1985) due to the ranging capability of the small footprint on the ground. However, due to the restrictions of the positioning performance, a large-area forestry inventory with laser scanning technology was not available until the 1990s when GPS and IMU sensors enter maturity, to be integrated into an airborne platform for guaranteeing positioning accuracy robustly. Because the beam divergence of the employed laser is typical at the sub-milliradian level, the generated laser spot on the ground is between several decimetres to several metres in diameter assuming that the operational altitude is 1000-10000 metres, which is competitive compared with other airborne sensors. The laser pulse interacts with different layers of the tree canopy when it passes through the trees and generates multiple returning echoes. Thus, it can improve forest parameter extraction at both the tree and plot levels. Small-footprint LiDAR data have been widely applied for a variety of forest inventory applications, including terrain detection (Kraus et al., 1998; Vosselman 2000), height estimation (Popescu et al., 2008), counting the number of trees and volume estimation (Naesset 1997; Hyyppä et al., 1999a), and forest change detection (Hyyppä et al., 2003; Yu et al., 2004). Based on case studies performed in boreal forests, Hyyppä et al. (1999b) revealed that the accuracy of ALS-based forest inventories was higher than that of optical remote sensors in stand attribute retrieval. ALS has also been extensively utilised for tree species classification based on point cloud combining with intensity information (Brandtberg et al., 2003; Holmgren et al., 2004; Donoghue et al., 2007; Kim et al., 2009; Ørka et al., 2009).

Various multidisciplinary studies have been carried out to investigate the potentialities of different remote sensing sensor for forestry inventory by integrating passive multispectral and hyperspectral sensors with an active ranging sensor such as LiDAR and synthetic aperture radar (SAR). All these passive/active sensors, with their unique peculiarities, can reveal different characteristics of the accessed forest. (Popescu et al., 2004; Dalponte et al., 2008, 2012; Ke et al., 2010; Jones et al., 2010; Clark et al., 2011; Alonzo et al., 2014). As airborne/spaceborne multi/hyperspectral data and airborne LiDAR data provide complementary information: hyperspectral data reveals horizontal spectral reflectance, and LiDAR data offers vertical structure information, respectively. A promising and challenging approach is to fuse these data in the information extraction procedure for forestry inventory of various climate zones ranging from boreal forest to tropical rain forest landscape.

Popescu et al. (2004) explored the feasibility of using small-footprint LiDAR data and multispectral imagery to estimate forest volume and biomass on small plots by measuring individual trees. Moreover, found by using the fused data set, LiDAR and multispectral imagery, as opposed to using LiDAR data alone, always improved biomass and volume estimates for pines and in some cases for deciduous plots. Ke et al. (2010) evaluated the synergistic use of high spatial resolution multispectral imagery and low-posting-density LIDAR data for forest

species classification using an object-based approach. Furthermore, the results showed the integration of spectral and LIDAR data, in both image segmentation and object-based classification improved the forest classification compared to using either data source independently. Jones et al. (2010) assessed the utility of airborne hyperspectral imagery and small-footprint discrete return LiDAR data for mapping 11 tree species in coastal South-western Canada. The research showed that the joint solution using a pixel-level fusion of hyperspectral imagery with LiDAR-derived height and volumetric canopy profile data increased both producer's and user's accuracies comparing with hyperspectral imagery standalone solution which yielded producer's and user's accuracies for most species. Dalponte et al. (2008) proposed an analysis of the joint effect of hyperspectral data and LiDAR data to classify the complex forest areas in Italy. They found that joint use of hyperspectral data and LIDAR data could improve the accuracy of classification of complex forest areas, and the elevation channel of the first LIDAR return (canopy height) was useful for the separation of species with similar spectral signatures but different mean heights.

Meanwhile, the SVM classifier proved to be very robust and accurate in the exploitation of the considered multisource data. Dalponte et al. (2012) continued their research to fuse very high geometrical resolution airborne/spaceborne hyperspectral/multispectral images and low/high point density LiDAR data. They declared that the experimental results showed that the set-up based on hyperspectral only data was effective with general macro-classes, forest types, and single species, reaching high kappa accuracies. Regarding LiDAR data, the experimental analysis showed that high-density LiDAR data provided more information for tree species classification concerning low-density data, when combined with either hyperspectral or multispectral data. Alonzo et al. (2014) fused airborne high-spatial-resolution (3.7 m) hyperspectral imagery collected by the 224-channel Airborne Visible and Infrared Imaging Spectrometer (AVIRIS) system covering 365 and 2500 nm with waveform LiDAR data which had an average last-return point density of 22 points/m<sup>2</sup>. And the ALS data was collected by a Riegl Q560 laser scanner at the individual crown object scale to map 29 common tree species in Santa Barbara, California, USA. Both species-level and leaf-type level maps were produced with respective satisfactory overall accuracies with hyperspectral data. Furthermore, the combination with LiDAR data resulted in an improvement in the final classification accuracy of 4.2 percentage points against standalone spectral data. The added value of the LiDAR structural metrics for urban species discrimination became evident, especially when the mapped crowns were either small or morphologically unique, such as tall palm species. Clark et al. (2011) evaluated the fusion of small-footprint, discrete-return LiDAR and hyperspectral sensors, to estimate of the aboveground biomass in a Costa Rican tropical rain forest landscape. LiDAR data were from an airborne sensor which measured the first single-return height above noise level in small footprints with a 0.9- $\mu$ m laser and a typical density of 9 points/m<sup>2</sup> in autumn, and hyperspectral data was collected by the airborne hyperspectral imaging sensor which measured 210 bands covering from 400-2500 nm region of the spectrum with 1.6 meters spatial resolution in spring. Clark et al. (2011)

found that standalone hyperspectral metrics provided lower accuracy in estimating biomass comparing with the metrics derived from LiDAR data; furthermore, the best model using two LiDAR metrics were better than models combining a single LiDAR with hyperspectral metric. This study also supported conclusions that LiDAR is a premier instrument for mapping biomass (i.e., carbon stocks) across broad spatial scales not only for tropical rain forest but also for other climate zones.

The major disadvantage for fusing hyperspectral data with LiDAR data is that, in most research cases, sensors were flown at different seasons and different period. The registration of active and passive data becomes problematic, and in other words, fusion accuracy cannot be fully guaranteed.

However, since most operating LiDAR systems adopt a monochromatic laser source, their ability to acquire spectral information from the LiDAR intensity is generally underestimated. In previous researches, LiDAR data is mainly used to extract the vertical structure, rather than an imager illustrated by a monochromatic light source. Compared with traditional passive imagers, such illustration is immune to the change of sunshine and incident angle. However, there are still some sound studies about radiometric calibration of LiDAR intensity have been performed (Kaasalainen et al., 2005, 2007a 2007b and 2009; Ahokas et al., 2006; Höfle et al., 2007; Briese et al., 2012; Du et al., 2019). Such researches lay the cornerstone for the further hyperspectral LiDAR research for using LiDAR-derived intensity for forest inventory.

In this dissertation, we investigated the feasibility of using HSL for detecting the tree plant with derived NDVIs. More vegetation indices could be obtained from the measured hyperspectral point cloud from the single-tree level, for example, the water concentration index and the modified chlorophyll absorption ratio index.

## 2.2 Plant science methodology

Classifying and mapping vegetation is a primarily technical task for managing various natural resources because vegetation provides a biological base for all living beings and also plays an increasingly important role in experiencing global climate change. Multi-temporal vegetation mapping presents valuable information for understanding natural environments by quantifying vegetation cover from regional (Schroeder et al., 2006) national (Huang and Siegert, 2006) continental (Cabral et al., 2006) and global scales (Townshend et al., 1991) in a cost-effective manner (Goetz et al., 1985; Langley et al., 2001; Nordberg and Evertson 2003).

Various imagery remote sensing technologies are known for their differences in spectral, spatial, radioactive and temporal characteristics and thus are suitable for different vegetation mapping purposes. The author will not cover the very details of the state-of-the-art vegetation remote sensing methods by all kinds of remote sensing technologies, and the literature review section mainly discusses

how spectrometry imagery and LiDAR remote sensing technologies support vegetation research.

In vegetation remote sensing research, the "red edge" refers to a rapid change region within the reflectance of vegetation or an inflection point of the reflectance slope in the red-band electromagnetic spectrum. This phenomenon results in the NDVI and is extensively utilised in the form of vegetation indices. An increasing amount of experimental results reveal that the "red edge" could be used as an indicator of botanical stress and plant senescence. The spectral position of the red edge is considered particularly important. (Collins 1978; Horler et al., 1983; Pu et al., 2003; Darvishzadeh et al., 2009). An analysis methodology to derive the red-edge variations from airborne multispectral images was introduced decades ago (Hare et al., 1984; Miller et al., 1990). The techniques related to the "red edge" are essential topics in remote sensing research communities (Dawson and Curran 1998; Cho and Skidmore 2006; Shafri and Hamdan 2009).

Vegetation has unique spectral features. Such spectral signatures can be identified from remote sensing imagery according to their distinctive characteristics to estimate photosynthetically and non-photosynthetically active vegetation. The radiance in the red and near-infrared region can be incorporated into the spectral vegetation indices (Asrar et al., 1984; Galio et al., 1985). The NDVI might be one of the spectral vegetation indices mostly investigated due to its availability from multiple spectral imagers. The physical principle of applying the NDVI in vegetation mapping is that vegetation is highly reflective in the near-infrared and highly absorptive in the visible red ranges. The contrast between these channels can be used as an indicator of the status of the vegetation. A global 8-km fractional vegetation cover dataset for 1982–2000 was also derived from the data of advanced very-high-resolution radiometer (AVHRR) of National Oceanic and Atmospheric Administration (NOAA) Land Pathfinder sensor (Zeng and Rao, 2003). Maselli and Chiesi (2006) also used data from AVHRR to study Mediterranean forest productivity based on NDVI.

The physical principle for mapping vegetation cover from remote sensing images relies on the unique spectral features of different vegetation types. Thus, hyperspectral imagery with a higher spectral resolution contains more vegetation information and can be used for more accurate vegetation mapping compared with multispectral imagery. The hyperspectral measurements from spaceborne and airborne platform such as AVIRIS, and Hyperion can be utilised for more sophisticated vegetation extraction on a regional scale, and recently, vegetation extraction from hyperspectral imagery has been increasingly studied. (Varshney and Arora 2004; Galvao et al., 2005; Li et al., 2005; Rosso et al., 2005). Li et al. investigated the possibility of classifying salt marshes both in China and in San Pablo Bay, California, using AVIRIS imagery, and the results were satisfactory, with a 93.8% overall accuracy in classifying two main marsh vegetation species. Galvao et al. (2005) discriminated five dominated Brazilian sugarcane varieties with Hyperion imagery, which might be impossible with multispectral images. Hyperion images were also utilised to estimate the salinity stress in a sugarcane field, for example, S. Hamzeh et al. (2013) found that

vegetation indices related to chlorophyll absorption bands or those based on a combination of chlorophyll and water absorption bands had the highest correlation with soil salinity.

However, conventional spectrometry imaging sensors also have inherent limitations for vegetation applications. Spectrometry imagery produces only two-dimensional images, which cannot fully represent the three-dimensional structure of vegetation, which might be critical for ecology research (Lefsky et al., 2002; Wagner et al., 2008). LiDAR is an alternative active remote sensing technology that increases the accuracy of biophysical measurements and extends the spatial analysis into the third dimension. LiDAR sensors directly measure the three-dimensional distribution of vegetation, thus providing high-resolution topographic maps and highly accurate estimates of the vegetation height and cover. Vegetation structure parameters can be derived from LiDAR data to improve carbon estimation (Ni-Meister et al., 2010). ALS systems can be used to map wetland topography, produce beach profiles and bathymetric maps for corresponding vegetation and ecological research (Ramsey 1995; Genç et al., 2004; Purkis and Klemas 2011). LiDAR measurements can also be used to model relationships between birds and vegetation structures (Bradbury et al., 2005; Goetz et al., 2010). Combined with other optical sensors, a more accurate assessment of vegetation on various terrains can be built (Bork and Su 2007; Huang et al., 2013); for example, G. W. Geerling et al. (2007) fused the data from a spectral imager and LiDAR to classify floodplain vegetation; the integration of hyperspectral imagery and LiDAR-derived elevation has also significantly improved the accuracy of mapping salt marsh vegetation and provides a better understanding of the topography, bathymetry, and hydrologic conditions (Yang and Artigas 2010).

In this study, two HSLs are used to determine the red-edge position of plants utilising high-spectral-resolution tunable filters to offer a consecutive spectral response: the first HSL uses an LCTF with a spectral range from 550 nm to 720 nm, and the second HSL uses an AOTF with a more extensive spectral range (500-1000 nm). We also compared the spectral responses collected from the HSL with the referenced data offered by a commercial spectrometer after calibration.

### **2.3 Mining methodology**

Remote sensing techniques have been used routinely in geologic interpretation for mineral and energy exploration, plant siting, and waste disposal, ever since the spaceborne remote sensing payloads were launched in the early 1960s, due to their cost efficiency, quick response and coverage compared with traditional methods (Goetz et al., 1981). The physical principle is straightforward: multi-spectral or hyperspectral remote sensing technologies discriminate among minerals based on the general differences that exist among their spectral properties collected through a non-contact manner (Hunt 1977). The advent of imaging spectrometry providing many hundreds of images of one single scene acquired

in a large number of spectral bands represents a significant improvement in remote sensing research and a challenge in processing and interpretation. The abundance of imaging spectrometry data allows researchers to seek new analytical methods (Goetz et al., 1985; Elachi et al., 2006).

Passive hyperspectral sensors can distinguish the reflected energy on multiple spectral bands, whose spectrum generally ranges from the VNIR to longwave-infrared (LWIR) bands. In addition to large-area geologic surveys based on spaceborne and airborne platforms, hyperspectral imaging has been widely used in mineral identification and outcrop geology (Murphy et al., 2012; Bauer and León, 2015). Automated mineral rock classification or identification based on spectral features extracted from hyperspectral measurements is extensively performed (Kurz et al., 2013). Bauer and León (2015) investigated mineral identification using hyperspectral fluorescence imaging. Kurz et al. (2013) presented the workflow and methods that use close-range hyperspectral imaging to study geological fields, which demonstrated the potential of hyperspectral imaging to describe rock characteristics in a non-contact manner and at a variable scale. However, such passive sensors cannot prevent the influence of changing illumination conditions and have a reduced ability to preclude shadows. Meanwhile, some underground mining sites face the practical problem that there is no available natural light source for imaging.

LiDAR can collect high-resolution spatial data due to its small footprint. The calculation of ore volumes can be accomplished by periodic scanning in areas of ore removal, especially open pits, then comparing the surface data to the previous scan. Naturally, 3D model reconstruction and measurement of open pits has been extensively investigated (Little 2006; Oparin et al., 2007) and will become a standard operation in the foreseeable future. The LiDAR can scan the entire surface mine with a line-of-sight condition. With reliable GNSS observations, an accurate 3D model can be built by a single scan or multiple scans (Sheng et al., 2010). LiDAR has been applied to generate DSMs (Digital Surface Models) and DOMs (Digital Orthophoto Maps) (Tong et al., 2015). Furthermore, it is used for various applications, such as the extraction of contour lines and fracture mapping (Slob et al., 2007); slope characterisation and stability assessments (Sturzenegger et al., 2007); production accounting; analysis of ore formations (Slob et al., 2004, 2005); and determining coal layer heights. Such effective 3D modelling capabilities can also be utilised beyond mining operations, such as monitoring coal gangue dumps (Shuang 2011), measuring mining subsidence (Palamara et al., 2007), and landslide warnings (Guoliang Zhao, 2009; Abellán et al., 2014).

The LiDAR is also a popular tool for outcrop investigations (Sturzenegger et al., 2009; Buckley et al., 2013; Hodgetts, 2013; Hartzell et al., 2014; Penasa et al., 2014). Buckley et al. (2013) investigated the fusion of laser scanning and hyperspectral imaging and demonstrated its important implications for improving geological data collection. Hartzell et al. (2014) used a multispectral LiDAR system for automated rock-type identification and descriptions. However, the multispectral LiDAR scans were fulfilled based on three standalone terrestrial laser scanning systems using different wavelengths rather than a single laser

source. The LiDAR configuration in this architecture restricted the spectral information. Besides, this method presented extra complexities in data registration. The need for constructing an accurate virtual underground mining world with relative ease and in a cost-effective manner has persisted through the last few decades. Integration of indirect georeferencing techniques such as IMU-aided simultaneous localisation and mapping (SLAM) and forward-backwards loop closure approaches would lead to precise 3D modelling of the underground environment (Konolige 2010; Kohlbrecher et al., 2011). Kinematic MLS can provide a multi-temporal record to build a 3D model of an ore mine and to potentially observe long-term deformations (Chen et al. 2016).

To build a precise and accurate spatial model of a mine with the latest developed monochromatic LiDAR is no longer impossible. Furthermore, by combining the spectral information, the LiDAR technique can support in situ ore classification for grade control and waste management for greener mining. In this study, the author investigated the feasibility of using the coverage spectrum of HSL from the VNIR to SWIR bands (450 nm-1600 nm) for ore classification. A standard SVM classifier is utilised to classify seven ores when all 17 spectral measurements are used. Furthermore, a 91-Channel AOTF based HSL with 5 nm spectral resolution is designed to successfully classify the coal/rock/gangue with three multi-label classifiers (Shao et al., 2019).

## 2.4 Optech Titan

A new airborne multispectral laser scanner system with three different wavelengths (532 nm, 1064 nm and 1550 nm), Optech Titan X (Teledyne Optech, Vaughan, ON, Canada), has been commercially available since 2015 during the period of this research. Comparing with the previous SHOAL system, the Optech Titan X enables a SWIR channel (1550nm). The 1550-nm wavelength is selected because of the ease in complying with eye-safety regulations; the 1064 nm wavelength is mainly for terrestrial mapping, and the 532 nm wavelength is mainly for bathymetry mapping, resulting in nearly equally spaced (500 nm) spectral sampling wavelengths. Another reason that 532 nm wavelength is selected is that 532-nm wavelength pulses can be obtained by adopting a frequency-doubling crystal on the output of a 1064-nm neodymium-doped yttrium aluminium garnet (Nd:YAG) laser.

Titan is the first operational multispectral airborne laser scanner that collects range, intensity and optionally full-waveform return data at three different laser wavelengths (1550, 1064, and 532 nm) through a single scanning mechanism. Titan is capable of capturing discrete and full-waveform data from all three channels, having a combined ground-sampling rate of 900K. With three independent channels in the visible, near-infrared and SWIR bands, scientists can use the intensity variations of various surface targets for material differentiation beyond previous topographic measurements. The detailed specifications of Titan can be found in Table 2.1. Its operational wavelengths and hardware appearance are presented in Figure 2.1. Such an instrument opens the door for active

multispectral imaging of the environment. When using the multispectral laser scanner, spectral information underwater, down in the canopy or shadows can be revealed. Naturally, this information might be very well suited for various ground object classification tasks and simultaneous topographic/bathymetric applications.

**Table 2.1** Specification of the Titan airborne system (Fernandez-Diaz et al. 2016)

	Visible	NIR	SWIR
Wavelength (nm)	532	1064	1550
Beam divergence (1/e)	0.35 mrad	0.35 mrad	0.7 mrad
Observation angle (degree)	7° forward	nadir	3.5° forward
Pulse Width (ns)	~3.7	3-4	~2.7
Pulse Energy (μJ)	~30	~15	50-20
Pulse repetition frequency	Programmable 50-300 K at 25-kHz intervals, 900 kHz total		
Field of View (FOV)	Programmable 0-60° maximum		
Effective scan frequency	Programmable 0-210 Hz		
Laser Classification	Class IV		
Elevation accuracy	<5-10 cm; 1δ		
Operation altitude	300-2000 metres		
Positioning and orientation system	POSAV AP50 (OEM); 220-channel dual-frequency GNSS receiver		
Roll compensation	Programmable; ±5° at 50° FOV; increasing with decreasing FOV from 50°		
Waveform capture	12 bit, 1 Gs/sec (optional)		
Range capture	Up to 4 range measurements for each pulse		
Power	800 W (nominal)		
Weight	Sensor head ≥ 71 kg, Control rack ≥ 45 kg		

Since Optech Titan has recently become available, various feasibility studies can be carried out. For example, land cover classification (Matikainen et al. 2017; Chen et al. 2018; Pan et al. 2019), vegetation mapping and tree species classification (St-Onge et al. 2015; Axelsson et al. 2018; Budei et al. 2018; Kukkonen et al. 2019), road mapping (Karila et al. 2017) and map updating (Ahokas et al. 2016). Volker et al. (2015) evaluated the potential of Titan data for topographic mapping and land cover classification. The dataset used is a single flight strip of a 3-km<sup>2</sup> area covering a city, and the results show that the dataset is suitable for conventional geometrical classification and mapping procedures. Additional classes, such as paved and unpaved ground, can be separated with high classification accuracy. Karila et al. (2017) investigated the feasibility of road mapping using Titan data, and the results demonstrated that the multispectral ALS data are feasible for automatic road detection, and a significant improvement is achieved compared to the use of optical aerial imagery (80.5% vs 71.6%, respectively). Matikainen et al. (2017) discussed the potential of this active remote sensing technique in map updating, especially in automated object-based land

cover classification and change detection in a suburban area. An object-based random forest analysis suggests that the multispectral ALS data are beneficial in land cover classification, considering both elevated classes and ground-level classes. The overall accuracy of the land cover classification results with six classes was 96% compared with the validation points. Budei et al. (2018) also used Titan data to identify ten tree species of single trees with random forest classifiers using both spatial and intensity data. The classification accuracy reached 75%, and the intensity information of the 1550-nm channel is the most useful variable.

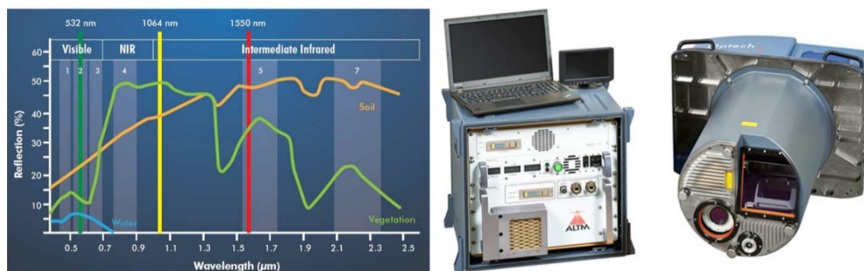


**Figure 2.1** The Titan system's operational wavelengths (left) and hardware (right)

The Titan system can perform simultaneous mapping in terrestrial and shallow-water environments and the visible "green" channel - the second harmonic 532-nm Nd:YAG laser is mainly for this purpose. The penetration depth is less than several tens of metres under very clean water-quality circumstances. Thus, scientists can research bathymetry, river morphology, hydrology, aquatic ecosystem and archaeology.

Scientists can produce false colour active imagery derived from the return intensities of the three-channel LiDAR system. By merely combining three independent intensity images into a false colour image, it is possible to access the multidimensionality of the colour space, which can highlight features that are not easily identified in a greyscale intensity image derived from a traditional single-wavelength LiDAR system.

Some advantages and limitations of Titan over traditional passive images have been summarised by Fernandez-Diaz et al. (2016). Its multispectral capabilities provide spectrally rich and consistent outputs that were not available before by other commercial single-wavelength LiDAR systems. However, the first commercial multispectral airborne laser scanning sensor operates on the different principle as what we purposed in this dissertation: 1) the footprint size on the ground are different for different wavelength and the footprint of SWIR band (1550 nm) is twice as other two wavelengths; 2) the angle of incidence is different, and only NIR band observes the nadir direction, which might cause some mismatched problem for different terrains and complex ground targets; 3) the wavelength selection is determined without any flexibility. However, with HSL, both the geometry and spectral information on the target are available from a single laser source without any inaccurate registration problem when matching the range measurements from different wavelengths.

## 2.5 Eye safety

A laser differs from other natural light sources in that it emits a high coherent energy beam which is high-power and low divergence. The hazard associated with high power is self-explanatory. Industrial cutting and welding applications have presented the utility of a high-power directional energy beam, and even a laser beam with much lower intensity can still destroy living tissue, for example, skin and eyes.

Low beam divergence means that, unlike familiar light sources that radiate uniformly, the delivered energy density of the laser beam decreases as the square of the distance based on LiDAR equation. The laser beams maintain their directionality well both near field and far field and remains a hazard for the eye even over greater distances. The directionality of the beam focuses the high-power energy onto a minimal retinal area, resulting in varying degrees of visual damage (Dillon and Parker 1969).

Lasers with the employed wavelengths longer than 1.4  $\mu\text{m}$  are generally regarded as "eye-safe" laser because the light in that wavelength spectrum range is strongly absorbed by the cornea and lens of the eyes and therefore cannot reach the retina. As a result, lasers source with an operating wavelength of 1.55  $\mu\text{m}$ , which is very popular in telecom systems, or 2.013- $\mu\text{m}$  thulium lasers for the surgical instrument are far less dangerous than the laser source who wavelength is less than 1.4  $\mu\text{m}$ , for example, 1.064  $\mu\text{m}$  Nd:YAG lasers with similar power outputs. Instead, the absorption length of the cornea reaches minimal values (well below 0.1 mm) at longer wavelengths, thus, lasers with emitting wavelengths of 3  $\mu\text{m}$  or 10  $\mu\text{m}$  (near the wavelength of CO<sub>2</sub> lasers) are less eye-safe than lasers emitting wavelengths in "eye-safe" region.

Laser and laser products have been classified into four classes and a few subclasses by wavelength and maximum output power since the early 1970s. Laser products are classified according to their ability to damage exposed personnel, from class 1 (no hazard during regular use) to class 4 (a severe hazard for eyes and skin)

However, scientists should note that the laser power alone (or the intensity at the laser output) is not sufficient enough to assess the possible intensity in the eye, which also depends on other factors, such as the beam quality and beam divergence. The beam divergence is relevant only in the "far-field", away from any focus of the beam. The laser's beam divergence is an angular measurement to describe the relationship between the increase in the beam diameter and the distance from the optical aperture from which the laser beam is transmitted. Therefore, one cannot merely state a power or intensity limit for eye safety at a given wavelength.

Since the spectral range of the current SCL source is 0.4~2.4  $\mu\text{m}$ , the particular concern should be taken into account for eye safety at this wavelength of the optical spectrum; eye safety is still a concern in both terrestrial or airborne platforms to assure that the maximum receiving power is below the threshold of

eye-safe peak power over all employed spectra. (Irish et al., 1999; Pfennigbauer et al., 2011). If a higher laser pulse energy is required, wavelengths must be considered for which the eye is less sensitive (Wehr et al., 1999). It is strongly recommended that an optical filter be installed at the exit of the laser transmitter to mitigate the power density of the emanating laser beam. If it is technically possible, the spectroscopic device, for example, the optical filter array, the AOTF device, or the LCTF device, should be placed on the transmitting part optics rather than receiving part when building an HSL system.

### 3. Methodology

Generally, the system configuration of HSL is similar to a typical LiDAR system, which usually consists of five subsystems: the first subsystem is a laser source and more specifically, is a supercontinuum laser source. The second subsystem is the transmitting and receiving optics, and the third subsystem is composed of the photodetector which converts the optical signal into an electrical signal, and the photodetector might be a single element detector or an array detector (Chen et al. 2004; Hakala et al. 2012) and receiver electronics. The fourth subsystem is an optional optomechanical scanner to steer a transmitted laser beam in the desired direction. The last subsystem is the spectroscopic device, which disperses the light according to its wavelength. Moreover, the spectroscopic device is typically installed and integrated within the transmitting or receiving optics. There is a meaningful difference if eye safety is a concern; integration of spectroscopic devices in transmitting optics are preferable since less electromagnetic radiation is transmitted. However, this configuration might be impossible for some spectroscopic devices, for example, spectrographs. The laser source and the spectroscopic device are unique components for HSL development compared with traditional LiDAR technology. The following flowchart, presented in Figure 3.1 explains the logical relationships among the components. The SCL pulse is emitted from a micro-structured optical fibre (MOF) and collimated using an achromatic lens before being transmitted and steered to illuminate the target. A minimal part of the transmitting pulse is sampled by a photodiode to start the time-of-flight measurement and also record the waveform of the transmitted pulse. The reflected pulse is collected by receiving optics and focused on photodetectors, converting the laser echo into an electric signal. The converted signal is sampled and recorded using a high-speed oscilloscope (sampling rate from several to tens of giga-points per second) and stop the ToF measurement for range determination. After covering all wavelengths, the stored digital records result in a set of spectrally resolved waveform echoes of the same target. Moreover, scientists can derive both the range and reflected radiation of the illuminated area on the target from the stored digital waveforms, then steps the scanner to scan the next point on the target. By repeating the scanning processing repeatedly, all desired targets are fully scanned to generate point clouds containing a hyperspectral presentation of targets.

The significant difference for various systems developed in this paper is how various spectroscopic devices/solutions should be integrated with traditional LiDAR system configuration to develop a novel HSL system. They can be inte-

grated into either transmitting optics or receiving optics as the green blocks presented in Figure 3.1, basically resulting in spectral-multiplexing solution and time-multiplexing solution. More specifically, Publications I, III, and IV mainly investigate the optical filter HSL technique for forestry, vegetation and mining applications. Publication II explores the spectrograph-based HSL for forestry applications. Publication V studies to use the LCTF device as spectroscopic devices in HSL for vegetation research and Publication VI examines how the AOTF device can be used in HSL systems for vegetation research. In summary, HSL technology opens the door for various environmental awareness applications by offering both high-spatial-resolution and high-spectral-resolution information within a single framework that can be utilised but not limited to forestry, plant science and mining applications.

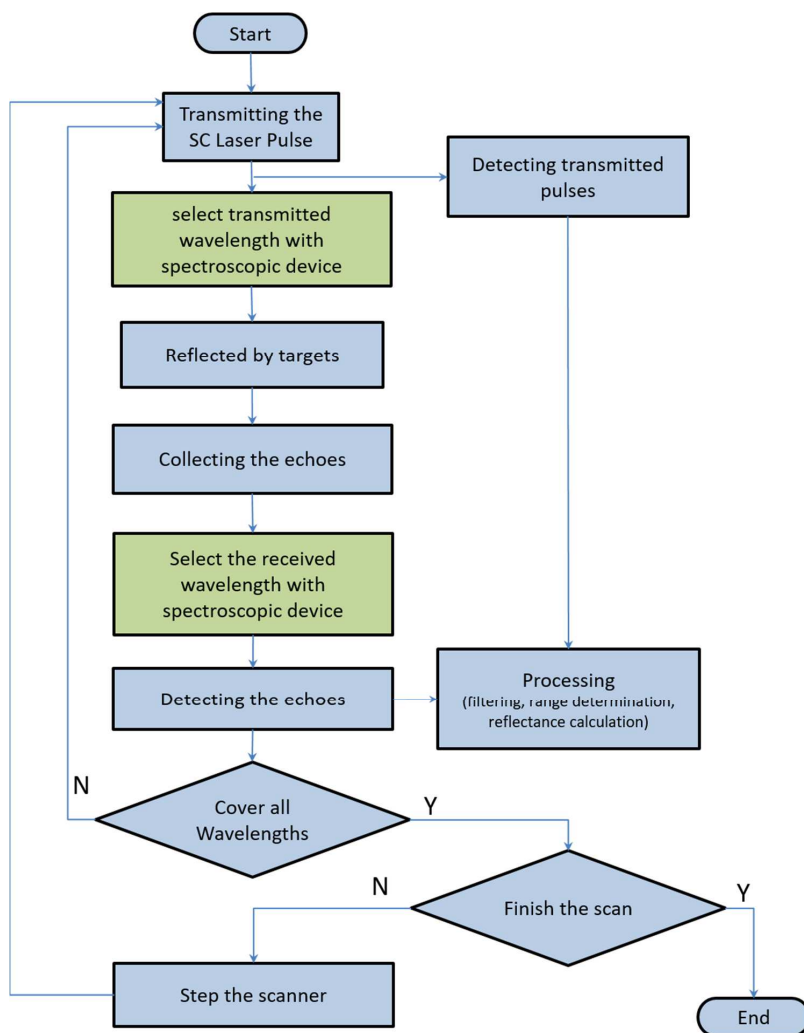


**Figure 3.1.** General flowchart of the developed HSL for environmental awareness purposes (the spectroscopic device can be integrated into transmitting optics or receiving optics as the green blocks are present).

### 3.1 Transmitting

Advancements in nonlinear fibre optics and compact pulsed lasers in recent years have brought to the market novel light sources: SCL sources, which are extremely broadband, yet as directional as a laser. These SCL sources produce coherent and directional broadband light by making use of cascaded nonlinear optical interactions in an optical fibre (Johnson et al., 1999; Dudley et al., 2006), and they can be used to simultaneously measure the range and the reflectance spectrum (Kaasalainen et al., 2007a).

Typically, a commercial SCL continuously covers the VNIR to SWIR spectrum, which is ideal for applications in which continuous spectral coverage is involved. However, with SCL, a spectroscopic device is inevitably necessary to separate the ultra-wideband laser spectrally. Such devices can be optical filter arrays (Muller and Yuen, 2008; Chen et al., 2010; Sun et al. 2017; Chen et al., 2018; Wang et al., 2018), spectrographs (Hakala et al., 2012; Sun et al. 2017), LCTFs (Li et al., 2018), and AOFTs (Wallace et al. 2016; Chen et al. 2019; Shao et al., 2019). The Finnish Geospatial Research Institute (FGI) began research on HSL technology based on SCL sources in 2007 for forestry applications (Kaasalainen et al., 2007a). In 2010, FGI demonstrated SLC-based two-channel hyperspectral LiDAR using optical filters (Chen et al., 2010), and in 2012, FGI created the first SLC-based full-waveform HSL system using a grating spectrograph to generate eight spectral signals ranging from 450-1000 nm simultaneously (Hakala et al., 2012). The full-waveform hyperspectral LiDAR was used to acquire hyperspectral information for extracting vegetation parameters, including the water content, chlorophyll content, NVDI. Both experimental results showed that the device could acquire spectral information and target-ranging information. FGI and AOE, CAS jointly designed a 17-channel HSL covering the visible-to-SWIR spectral range (450-1600 nm) using optical filter groups for ore classification, and the classification results were promising (Chen et al., 2018). Most of the developed HSLs all have a limited and discrete spectral channel, which severely hinders the understanding and further applicability of the newly developed technology. We also investigated the HSL solutions that can offer continuous spectral coverage in this dissertation: a tunable HSL based on the AOTF, called an AOTF-HSL, and another tuneable HSL based on the LCTF. FGI and AOE also jointly designed an LCTF-based HSL system to detect the red edge for vegetation-related applications, and significant correlation coefficients of the two spectral profiles collected by the HSL and the referenced spectrometer on the same vegetation could be observed (Li et al., 2018). LCTF-based HSL can offer continuous spectral coverage compared with the optical filter solution. However, due to the restricted spectral range of the employed LCTF component together with a low power density of the transmitting “white” laser pulse at 450-550 nm, only the data from 18 spectral channels were available for a better signal-to-noise ratio from 550 nm to 720nm with a 10-nm spectral resolution. In addition to being lightweight and having low power consumption, the image quality of LCTFs makes them ideal candidates for remote sensing applications. However, a potential disadvantage of LCTF-based solutions is the tuning speed. And the tuning speed of LCTF usually is several tens of milliseconds, mainly

determined by the switching speed of the liquid crystal elements, which will restrict its application for a fast-speed platform, for example, ALS or MLS applications. As a result, multiple LCTFs in separate optics paths are required in optical designs for MSLs applications.

The AOTF-HSL was proposed, designed and tested, covering the VNIR spectral range (500-1000 nm) with a spectral resolution of 5-10 nm. Due to the maturity of the applied AOTF component, the complexity, dimensions and hardware investment of HSL are considerably reduced, and a continuous spectrum with an excellent spectral resolution can be achieved. The AOTF enjoys a quicker tuning speed (microseconds) and broader wavelength ranges than the LCTF, which is also critical for ALS and MLS applications. Moreover, multiple simultaneous frequencies can be applied to the AOTF device without excessive intermodulation. This feature allows controlled wavelength mixing, which is preferable for HSL. However, AOTFs rely on the acousto-optic effect of sound waves to diffract and shift the frequency of light.

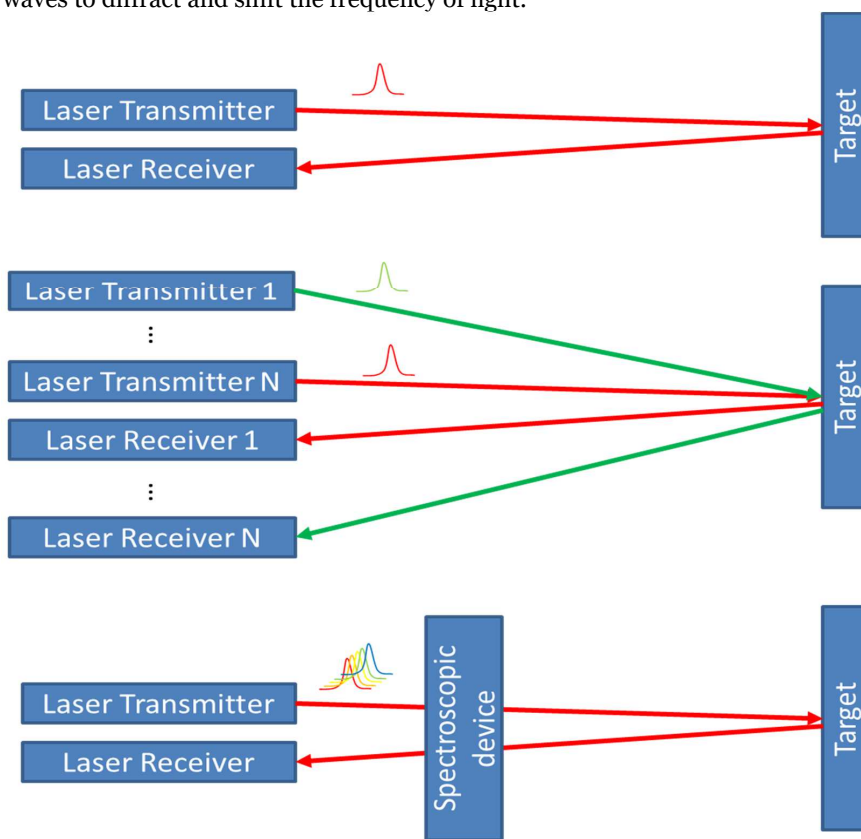


**Figure 3.2** The concept illustrations of traditional LiDAR, MSLS based on several monochromatic lasers and hyperspectral LiDAR

Figure 3.2 presents the differences and similarities between traditional LiDAR and MSLS based on multiple monochromatic lasers and HSL-based SCL. The

advantages and disadvantages of using different spectroscopic devices are preliminarily concluded in Table 3.1,

**Table 3.1.** The advantages and disadvantages of different spectroscopic devices based on HSL

	Multiplexing	Flexibility	Size	Cost	Spectral Range	Development difficulty
Optical filter(s)	Spectral multiplexing	High	Medium	Medium	Wide	Medium
Spectro-graph	Spectral multiplexing	Medium	Large	High	Medium	High
LCTF	Temporal multiplexing	Low	Small	Low	Narrow	Low
AOTF	Temporal/Spectral multiplexing	Medium	Small	Low	Medium	Low

### 3.2 Receiving

To convert light photons into a current in the receiving part, the photodetectors utilised in LiDAR can be a charge-coupled device (CCD), a photodiode, an APD, or a PMT. Because traditional LiDAR for TLS, MLS and ALS operates in the VNIR, a conventional silicon photodetector can be used with low multiplication noise by exploiting the photoelectric effect. An InGaAs detector, with an absorption window of approximately 1.1–1.7  $\mu\text{m}$ , can be used to detect infrared pulses out to a SWIR wavelength. It operates in the infrared spectrum at a relatively long wavelength that allows for considerably higher power density and longer ranges, even though the InGaAs detector is less sensitive than silicon detectors. From the viewpoint of eye safety, InGaAs detector covers partial less hazardous wavelengths (1.4 $\mu\text{m}$ -1.7 $\mu\text{m}$ ) than the conventional silicon detectors (0.4 $\mu\text{m}$ -1.1 $\mu\text{m}$ ). Mercury Cadmium Telluride (HgCdTe) photodetectors can cover a broad bandwidth from MIR (~3-5 $\mu\text{m}$ ) to LWIR spectral ranges (8-12 $\mu\text{m}$ ) with high quantum efficiency typically at liquid nitrogen temperature (~77K) to reduce thermal noises, and very low excess noise can be achieved with such a system configuration (Sun et al., 2017). However, an extra bulky and sophisticated cooling system is required to control the temperatures of the sensor. Another disadvantage of HgCdTe photodetectors is the expensive hardware investment which might restrict the massive applications. Besides, 2D materials have attracted significant interests in photodetection applications in the last decade. They possess various unique advantages, such as strong light-matter interaction for high efficiency, large absorption bandwidth for broad operation bandwidth, and easy fabrication and integration for new possible functions (Sun et al., 2016), for example, graphene is a well-known example of an excellent 2D material with great potential to manufacture the further broad bandwidth photodetector. However, there is still no commercial photodetector based on 2D material available by far. Nevertheless, it is widely accepted that the missing of high-performance photodetectors with an ultra-extended spectral response considerably limits the wavelengths (typically ~400-1100nm) of HSL LiDAR systems and their applications.

The developed HSL systems cover the spectrum from VNIR to SWIR. Thus, the detectors used in this research are silicon APD (Publications I, III, IV, V, and VI), InGaAs APD (Publications III and IV), and silicon APD array (Publication II) with high-voltage power supplies. The current converted by the photodetector is recorded by a high-speed digitiser to generate the echo waveform for further analysis. The high-speed digitiser can be an oscilloscope (Publications I, III, IV, V and VI) or an analogue-to-digital converter (Publication II). The sampling rate and resolution of the digitiser determine the range resolution, and the resolution of the echo intensity and also decide the post-processing algorithms, for example, waveform fitting and range determination. Both the general range precision and accuracy of the spectral measurement were evaluated against reference values collected by commercial laser telemeters and spectrometers.

All the processing is based on the collected waveform of the transmitted signal and the receiving echo. Usually, the waveform detected by the APD sensors will be converted into a digital waveform by a high-speed oscilloscope or digitiser (at a sampling rate of several GHz to twenty GHz). The collected waveforms are generally pre-processed in MATLAB. The pre-processing includes, for example, Gaussian filtering, range determination, and reflectance calculations. Meanwhile, SVM-based data processing carried out in the dissertation is performed in Python based on different AI packages, such as the Scikit-learn Python package.

## 4. Results

The primary aims of this research are to develop various new HSL techniques and investigate their feasibility in forestry, vegetation and mining applications. Thus, the results of the research include

- 1) the feasibility of the developed HSL hardware;
- 2) the accuracy of the range measurement;
- 3) the accuracy of the spectral measurements and how we can utilise such measurements in forestry inventory, plant science and mining applications.

### 4.1 New HSL technology

#### 4.1.1 Spectrograph-Based HSL

The optical setup of the spectrograph-based HSL is presented in Figure 4.1. The receiving optics and electronics are similar to that of a spectrograph-based passive hyperspectral imager, more specifically, the system configuration of the spectrograph, and the parallel narrow-echo pulse detection and ADC subsystem is identical.

The SCL (NKT Photonics, SuperK) produces  $\sim 1$ -ns pulses at a repetition rate of 24 kHz and an average power of 100 mW spreading over a spectral range of 480–2200 nm. The ultra-broadband output laser is collimated using a refracting collimator. The collimated beam passes through a beam sampler, which takes a part of the beam to trigger the time-of-flight measurement. An off-axis parabolic mirror (a 50.8-mm diameter, a 152.4-mm effective focal length and a  $90^\circ$  off-axis angle) is used as the primary collecting optic to collect the echo. Two 4-mm holes are drilled through the mirror, one parallel to the optical centreline and one towards the focal point. This configuration allows the main beam to be passed through one hole to the target, while the light for triggering waveform collection is guided directly to a spectrograph (Specim, ImSpector V10) through the other hole. A 16-element silicon APD array module (Pacific Silicon Sensor) is used to convert the spectrally separated light to analogue voltages. The APD module has built-in trans-impedance amplifiers (Analog Devices, AD8015) with a bandwidth of 240 MHz, producing an unambiguous resolution of approximately four nanoseconds. Eight 12-bit ADCs (SP Devices, ADQ412), with a 1-GHz sampling rate, are used for digitising 8 of the 16 available spectral channels to fulfil the full-waveform collection capability. The scanning geometry is de-

finied by the two rotators (Newport URS75BCC and URS100BCC) with an absolute accuracy of  $\pm 0.0115^\circ$ . The rotators are attached with one performing the azimuth rotation and the other sweeping the laser over the target area in vertical passes.

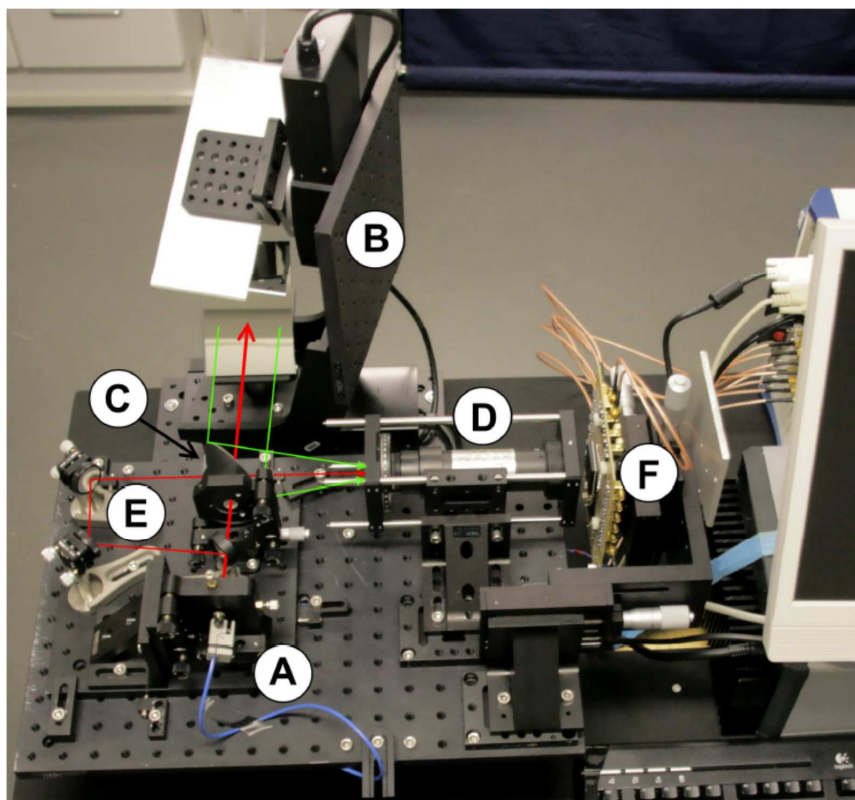


**Figure 4.1.** The optical setup: a laser pulse from a photonic crystal fibre (A) is collimated and sent to a 2D scanner (B). An off-axis parabolic mirror (C) is used as the primary light-collecting optic. A spectrograph (D) disperses the colours of the trigger (E) and echo pulses to an APD array, which converts the light to analogue voltage waveforms.

The channel selection and the spectral channel configuration are presented in Figure 4.2. The current configuration produces a spectral full width at half maximum (FWHM) of approximately 19 nm for each APD element and a spectral sampling interval of 34 nm. With a 16-element APD array sensor, the spectral range is 470-990 nm. However, the sensitivity of both the silicon APD array and the intensity of SCL below 550 nm are low, and the SNRs of collected waveforms below that threshold are poor. Therefore, the first channel was set to 542 nm, followed by 606, 672, 707, 740, 775, 878 and 981 nm. Such channel selection has been optimised for the measurement of vegetation focusing on “red-edge” detection as a bold solid curve presenting the spectral profile of Norway spruce collected by the passive spectrometer in Figure 4.2 (Hakala et al., 2012). A monochromator (Oriel, Cornerstone 74125) was used to calibrate and guarantee the spectral responses of each APD element. By using a Spectralon reflection board (Labsphere, Inc.) with 99% reflectance as a reference target at various distances

and Gaussian function fitting, the original waveform collected by the ADC can produce the backscattered reflectance waveforms of the targets. (Hakala et al., 2012).

The optical design of the spectrograph-based HSL is similar to passive spectral imagers. The major disadvantage of such a design is the hardware investment for high-speed ADC. Such a spectral-multiplexing system configuration will significantly increase the system size, power consumption and complexity in addition to the cost when the channel members increase due to its parallel read-out electronics design requiring extreme high-performance A/D conversion.

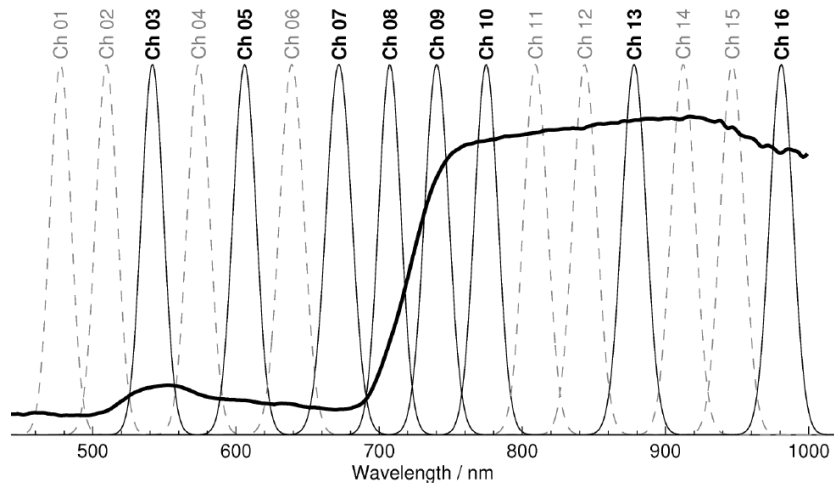


**Figure 1.2.** Spectral channel configuration and the eight selected channels (with solid curves) for vegetation applications

#### 4.1.2 Optical-Filter-Based HSL

The major disadvantage of spectrograph-based HSL is the system cost, especially for the receiving electronics. By using a beam splitter and bandpass optical filter configuration, it is possible to modify the system for several specific experiments by merely changing the bandpass optical filter groups. An ADP made of a material other than silicon can extend the spectrum of the HSL from VNIR to SWIR bands. Based on the first prototyped two-channel HSL based on an optical filter, the system configuration can be easily extended to encompass a multi-channel solution only if 1) the receiving optical configuration is modified; 2) a bandpass filter group filters the response echoes with different settings, and 3) another APD made of other materials is introduced. We first demonstrate an optical filter-based two-channel version HSL and then extend it into an eight-channel version and later to a seventeen-channel version.

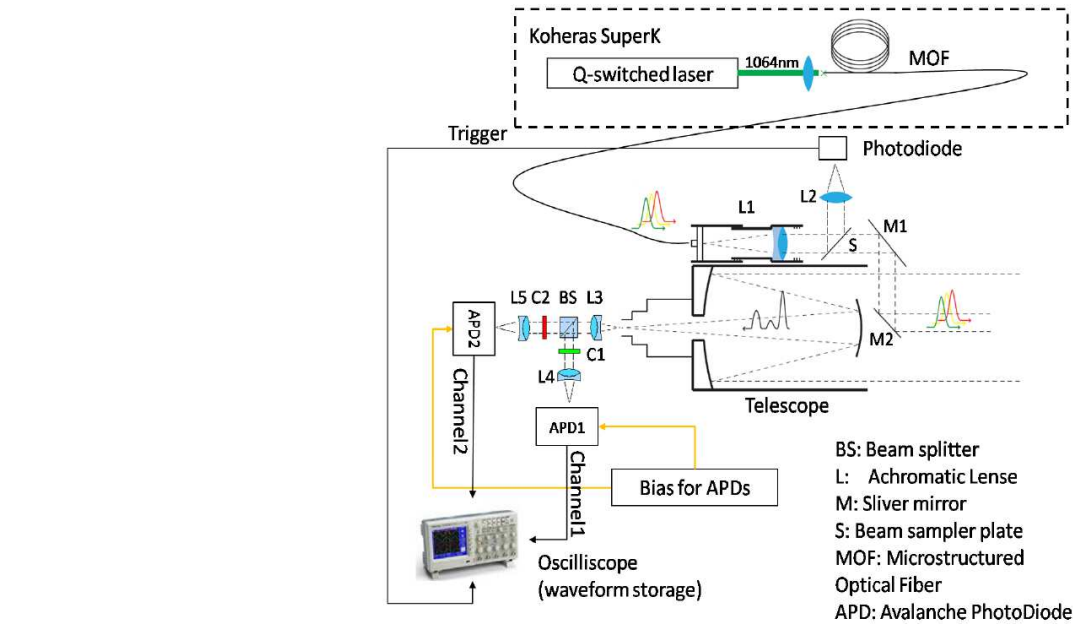
#### A: Two-Channel, Optical-Filter-Based HSL

Figure 4.3 presents the schematic of the two-channel, optical filter-based HSL. The light source used is a supercontinuum laser source (Koheras, SuperK) with

a wavelength range of 600 to approximately 2,000 nm and average output power of 100 mW. The pulse rate is 20–40 kHz with a 1–2-ns pulse width. The ultra-wideband laser pulse is emitted from a MOF with a high divergence angle. Therefore, it is collimated using an achromatic lens (L1 in Figure 4.3) before being transmitted to the object. The collimated beam is reflected towards the target employing two silver mirrors (M1 and M2 in Figure 4.3). Mirror M2 is placed at the optical axis of the receiving telescope. A photodiode sensor is situated beside a beam sampler plate (S in Figure 4.3), which is used to collect the sample of the transmitting laser beam reflected from the beam sampler plate. The collected signal is applied to trigger a high-speed oscilloscope to archive the waveforms of both the transmitting pulse and the receiving echoes, whereby the ToF measurement could be carried out using a post-processing program.

A Cassegrain telescope (with a 1,000-mm focal length and a 10-cm aperture diameter) collects the scattered laser pulse from the target. The focal point of the telescope is imaged onto two avalanche photodiode sensors (APD1 and APD2 in Figure 4.3) via a beam splitter (BS in Figure 4.3) and three achromatic lenses (L3, L4 and L5 in Figure 4.3). The split beam is filtered using a bandpass colour filter (C1 and C2 in Figure 4.3 with a bandwidth of 40 nm and a peak transmission of 600 nm and 800 nm for channel1 and channel2, respectively). The filtered beam is focused via the achromatic lens onto the high-voltage-biased APD sensor, which converts the laser echo into an electronic signal. The output signals from the APD sensors are sampled and recorded using a high-speed oscilloscope (a sampling rate of 5 giga-points per second, a bandwidth of 500 MHz, and four channels), resulting in a set of spectrally resolved waveform echoes (two channels in this case). Therefore, the prototype system measures the ToF and the spectrum of the returning echoes by post-processing the recorded waveform from each channel. The experiment demonstrates the instrument's ability to distinguish vegetation (the Norway spruce target) from inorganic material through the NDVI parameter. The spectral response of the APD sensor is typical for silicon APD with a peak spectral response at 800 nm. There is typically an increase in the reflectance at approximately 700 nm for vegetation targets, which is known as the "red edge", resulting in NDVI values greater than zero (Glenn et al., 2008). Furthermore, the characteristic of the peak spectral response at 800 nm can increase the SNR of the near-infrared measurement. Therefore, spectral bands of 600 nm and 800 nm provide the best SNR and distinguish Norway spruce from inorganic material.

The two-channel hyperspectral LiDAR (Figure 4.4) was tested at the Geodesy Laboratory of FGI in December 2009. The laboratory has a 12-metre concrete table, which enabled the targets to be placed at a measured distance of ~11 metres from the laser source. Two sets of experiments were designed to measure the precision of the hyperspectral LiDAR system. The goal of these experiments was to demonstrate the feasibility and applications of hyperspectral range-finding measurements and to evaluate the performance of the prototype system.



**Figure 4.3** Schematic setup of the two-channel optical-filter-based hyperspectral LiDAR

The first experiment evaluated the performance of the system as a laser range finder based on time-of-flight measurements. A Spectralon (Labsphere, Inc.) reflection board (reflection rate: 99%) was placed 11 metres from the aperture of the telescope along the optical axis of the telescope. The target was replaced at a position of 10 metres, and the time difference between these two measurements was determined using a high-speed oscilloscope.

The feasibility of the simultaneous range and spectral measurements was demonstrated in the second experiment. A Norway spruce tree target was placed at a distance of 9.3 metres in front of the Spectralon reflection board placed at a distance of 10.7 metres. The transmitting laser pulse passed through the branches of the spruce tree and was projected onto the reflection board. The main part of the pulse was reflected by the spruce and the remaining part by the Spectralon panel, thus producing multiple echoes. This method enabled the distances and reflectances at 600 nm and 800 nm for both targets to be compared.

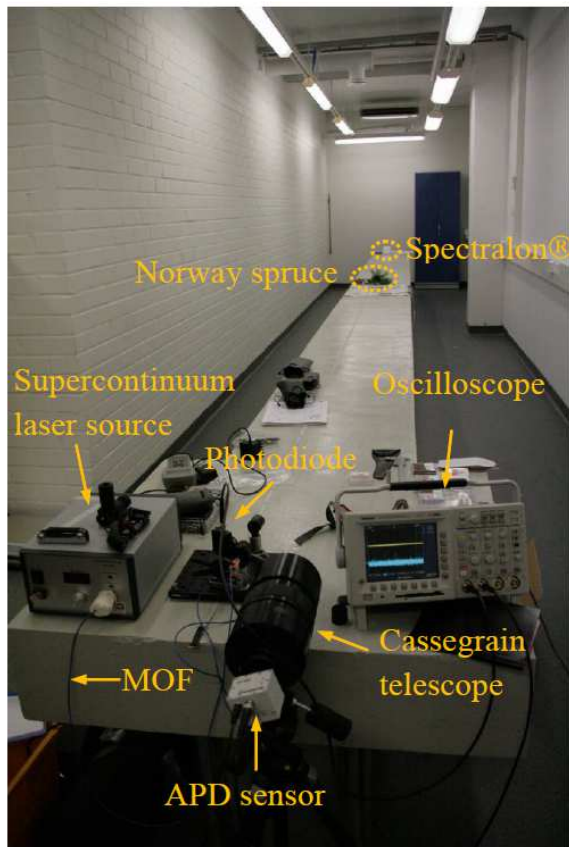


**Figure 4.4** Two-channel optical-filter-based hyperspectral LiDAR used in the laboratory test

### **B: Eight-channel optical-filter-based HSL**

A two-channel HSL based on an optical filter is a conceptual demonstration of HSL that can collect spatial and spectral information within a single system framework. However, the two-channel configuration is insufficient for most remote sensing applications. Thus, a more complex 8-channel optical-filter-based HSL covering the VNIR to SWIR bands was designed and tested. The spectral channel selection was accomplished by turning the wheel where the eight optical filters were installed. The prototype HSL can be upgraded into eight authentic channels with parallel electronics as a spectrograph-based HSL.

The proposed HSL system is shown in Figure 4.5. An SCL (Leukos© SCM 30-HE-450) outputs a broadband laser with a spectral range of 450-2400 nm. The broadband laser beam is led in a fibre collimator through the output fibre. The fibre collimator outputs the collimated beam. A beam sampler reflects a part of the collimated beam for triggering the start of the ToF measurement using a silicon APD (Menlo Systems APD 210). The main beam transmits through the beam sampler and passes through a hole of a 90° off-axis parabolic mirror (76.2-mm diameter) to a scanning mirror. The hole is parallel to the optical centreline of the parabolic mirror. The scanning mirror also reflects the echoes of the targets to the parabolic mirror. The off-axis parabolic mirror collects and focuses the echoes to the spectroscopic devices. At present, a device could rarely cover

a wide spectral range from the VNIR to the SWIR bands. Therefore, a long-pass dichroic mirror, installed between the parabolic mirror and the spectroscopic device, is used as a spectral beam splitter. The cut-off wavelength of the long-pass dichroic mirror is 950 nm.

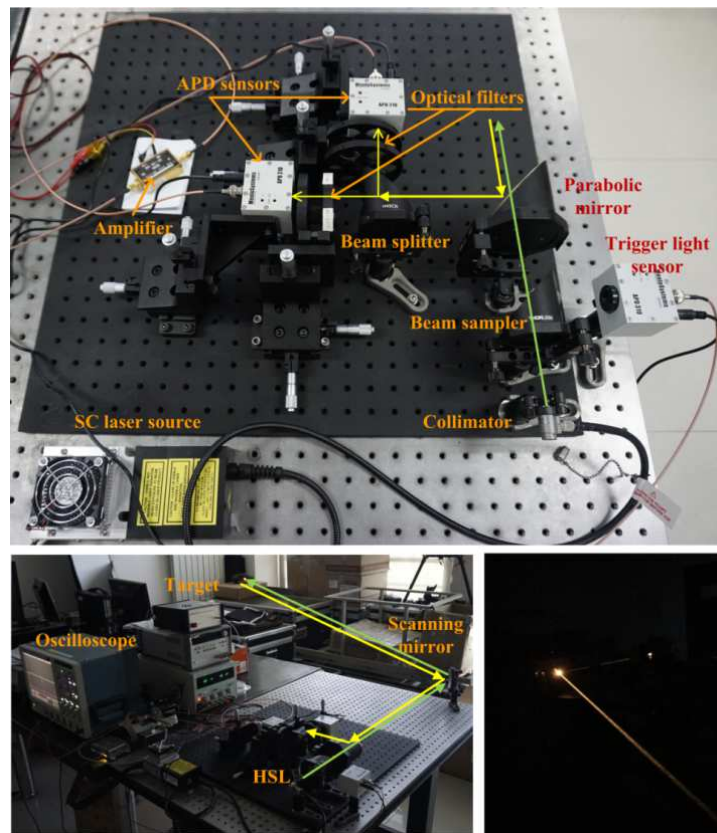


**Figure 4.5.** The 8-channel and 17-channel HSL system and the experimental scene

The beam splitter reflects the VNIR echoes, and the SWIR echoes are transmitted. In the HSL, eight narrow-bandpass optical filters, divided into a VNIR section and a SWIR section, are installed before the APD sensors. The central wavelength  $\lambda$  and the bandwidth  $\Delta\lambda$  of these optical filters are listed in Table 4.1. The optical filters are used as the spectroscopic devices to select the wavelength of the echoes. A Si APD (Menlo Systems APD210) sensor and an InGaAs APD (Menlo Systems APD310) sensor are used to detect the VNIR echoes and SWIR echoes, respectively. An extra amplifier was used to amplify the signals collected by the InGaAs APD due to its lower sensitivity (the sensitivity of the Si APD is one order of magnitude higher than that of the InGaAs APD). The output signals of the two APD sensors and the trigger signal are recorded and sampled by a high-speed oscilloscope, of which the sampling rate is 5 GS/s.

**Table 4.1.** The central wavelengths and the bandwidths of the filters

	VNIR			SWIR				
$\lambda$	540 nm	670 nm	800 nm	990 nm	1064 nm	1100 nm	1225 nm	1460 nm
$\Delta\lambda$	20 nm	20 nm	20 nm	15 nm	15 nm	15 nm	11 nm	10 nm

In the experiment, the HSL detected several targets, including the reflection boards (the 5%, 20%, 40%, 70% and 99% reflection boards), *Scindapsus* plants, plagioclase samples, and white ceramic cups. The targets were placed at a measured distance of 3 metres from the HSL system. A standard spectrometer measured the target's spectra as a reference value, to evaluate the accuracy of HSL-derived spectral profile. The first test is an evolution-of-range measurement. A white ceramic cup and a 99% reflection board are placed at approximately 3- and 5-metre distances to examine the range performance of the HSL system and its capability of discriminating different "white" shades based on the echo's amplitude. The second test is to evaluate the hyperspectral capability by comparing the measured spectral curves with the spectrometer reference measurements of the targets. Gaussian fitting is utilised to process the echo waveform in this research. With the standard 99% reflection board (whiteboard), the target's reflectance spectrum can be obtained according to the ratio of the echo intensity at each channel of each target to the coincident measurements of the whiteboard.

### C: 17-channel optical-filter-based HSL

Based on the 8-channel optical filter-based HSL prototype, we quickly extended it to a 17-channel version by modifying the optical filter group for a more specific feasibility study: ore classification. We investigated the feasibility of the ore classification application using HSL with 17 spectral channels covering the VNIR to SWIR spectral ranges. A multiple SVM classifier was used to classify the spectral profiles collected from ore samples. Seven types of ore samples (apatite, calcite, fluorite, olivine, orthoclase, plagioclase, and quartz, as Figure 4.6 presents) were measured using HSL to acquire the spectral profiles and distance information.

**Table 4.2.** The details of the spectral configuration of the optical filter based on 17-channel HSL

Channel (VNIR)	Wavelength /nm	Channel (SWIR)	Wavelength /nm
1	450	10	1070
2	540	11	1120
3	615	12	1230
4	670	13	1300
5	700	14	1360
6	750	15	1420
7	800	16	1557
8	845	17	1600
9	925		

We obtained range measurements and hyperspectral information simultaneously from the waveforms collected via the developed HSL system under a controlled laboratory environment (Figure 4.5), which covered 17 spectral channels from 450 to 1600 nm. It was an upgraded version of the 8-channel HSL system by modifying the optical filter groups. The details of the spectral configuration of optical filters are listed in Table 4.2. In total, seven ore samples and a reference whiteboard with 99% reflectivity were measured during the laboratory test. We placed the ore samples in front of the 17-channel HSL system. The ore samples were placed at a measured distance of 3 metres from the HSL due to the low SNR of channels lower than 550 nm. They were observed under the condition that the dimension of the ores was considerably larger than the footprint of the laser in a dark environment, as Figure 4.5 shows, to mitigate the influence from other light sources even though the high-speed oscilloscope collected the signals in an AC coupling mode. In this research, we used a Gaussian model to fit the collected signals to obtain the amplitude peak of the waveform. We selected 35 of these ore samples (five samples of each ore) as a training dataset and 1,750 samples as a testing dataset for the designed multiple SVM. Besides, the SVM parameters were identical for the objective comparison of the classification performances of different feature vectors. Second, we attempted to optimise the system design to have a lower cost and system complexity based on the feature contribution degree (FCD) method, and the normalised variances in the reflectance values for different ore samples at the same wavelength were calculated and treated as the FCD. Two groups of feature vectors, called minvectors and maxvectors, were selected using the FCD values sorted two different ways: ascending and descending.



**Figure 4.6.** Seven standard ore samples from a geological research institute

### 4.1.3 LCTF-based HSL

Most of the developed HSLs have a limited and discrete spectral channel, which actively hinders the understanding and further applicability of the developed technology. Since the SCL transmits a supercontinuum laser pulse with a spectral wavelength ranging from 450 nm to 2400 nm, it is natural to investigate the possibility of developing an HSL that can continuously cover the full spectrum. An LCTF is an optical bandpass filter whose centre wavelength is tunable by electronically controlled liquid crystal (LC) elements to transmit a selectable wavelength of light and exclude others (Gat N. 2000). LCTFs are known for enabling high image quality and allowing relatively easy integration concerning optical system design and software control, and they are widely used in multi-spectral snapshot imagers for earth observation (Nag, S. et al., 2017). The major disadvantage of LCTF is lower peak transmission values than conventional fixed-wavelength optical filters due to the use of multiple polarising elements. We investigate the feasibility of detecting the red edge utilising a consecutive and high-spectral-resolution active remote sensing technique, more specifically, the LCTF-based HSL system. In this system, an LCTF was installed before a silicon APD module (APD 210) for electronically and consecutively selecting the wavelength of the backscattered echoes. This component enables the HSL to generate consecutive and high-spectral-resolution measurements. To the best of knowledge, this is the prototype LCTF-HSL system based on SCL sources for remote sensing research.

The spectral performance of the prototyped LCTF-HSL system is evaluated in this feasibility research. Furthermore, laboratory experiments of vegetation red-edge detection are also investigated with the prototyped LCHF-HSL system to assess its feasibility for agricultural applications. The LCTF-HSL system measures two plants (aloe and dracaena) with yellow and green leaves. The spectral profiles of each sample are also collected by an SVC spectrometer (SVC HR-1024) as a reference for comparison.

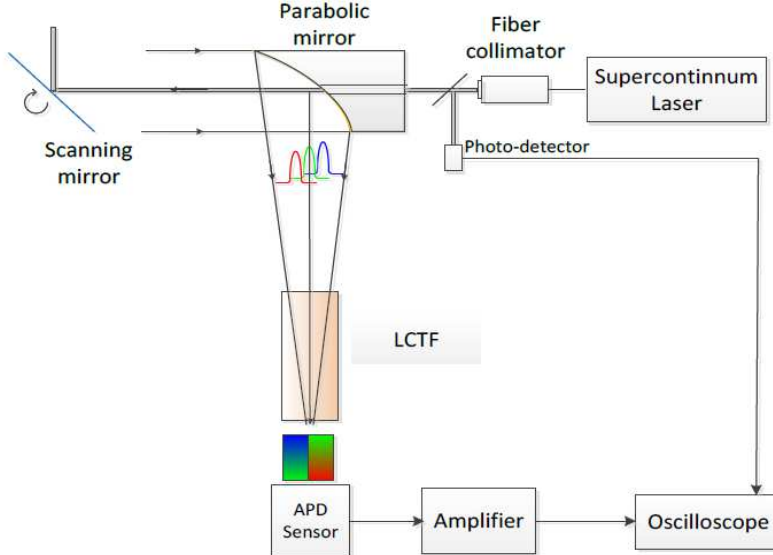


Figure 4.7. Schematic diagram of the LCTF-based HSL system

Figure 4.7 presents an illustrative diagram of the proposed LCTF-HSL system. The major components are similar to the optical-filter-based HSL, except the spectroscopic component from optical filters are replaced with an LCTF device. The parameters of the employed LCTF device (CRI© VariSpec VIS) can be found in Table 4.3. Besides, the LCTF device can equip the HSL with a high spectral resolution better than 10 nm, and in the performance evaluations, a 10-nm spectral resolution is selected, which is a compromise between the spectral resolution and a proper SNR measurement. It is evident that LCTF is a technique for temporally dividing multiple spectral filters; its mechanism is different from grating and the optical-filter-based HSL solution: the APD sensor can only detect the echo of the selected spectral channel at a time. However, such a time-multiplexing technique can substantially save hardware investments and decrease the size, power consumption and complexity of the HSL system. It is also a suitable solution for laboratory tests, especially in a feasibility study. The LCTF-HSL hardware prototype was set up in the laboratory (Figure 4.8) for a system performance evaluation by placing the vegetation samples at a distance of 3 metres. The laboratory experiments mainly evaluated the spatial and spectral capabilities of the proposed LCTF-HSL system by examining its range accuracy, validating the reflectance value and detecting the red-edge position of vegetation.

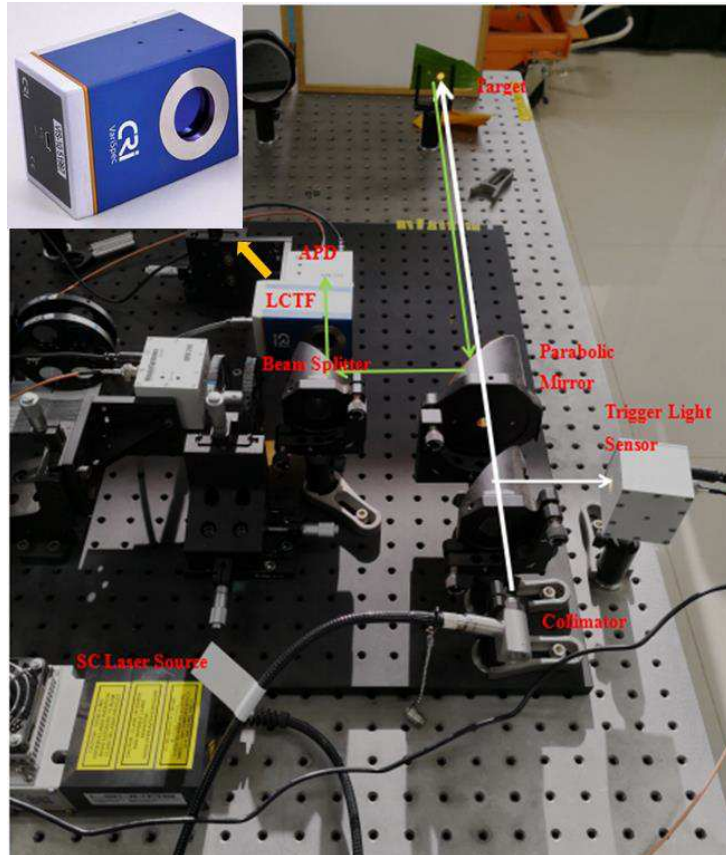


Figure 4.8. LCTF-HSL prototype

**Table 4.3.** Technical specifications of the LCTF device

Model	VariSpec VIS	Wavelength Accuracy	Bandwidth/8
Spectral Range	400-720 nm	Maximum Optical Throughput	500 mW/cm <sup>2</sup>
Aperture	20/35 (mm)	Response Time	50 ms
Visual Angle	7.5°	Bandwidth FWHM	7/10/20 nm

#### 4.1.4 AOTF-based HSL

LCTF-HSL offers the possibility of generating continuous hyperspectral data; however, due to technical restrictions on both the SCL and the LCTF spectroscopic device, it only covers the spectrum from 550 nm to 720 nm with a 10-nm spectral resolution for better SNR measurements. Another potential disadvantage is the response time of the LCTF device. The tuning speed of the LCTFs usually is generally several tens of milliseconds, mainly determined by the switching speed of the liquid crystal elements, which will restrict its application for airborne HLS applications. As a result, multiple LCTFs in separate optics paths operating as an optical filter are required for optical designs in HLS applications. We also consider HSL solutions that can generate genuinely continuous hyperspectral data. We selected the AOTF device as the spectroscopic device.

An AOTF is a tuneable bandpass narrow-band filter with a bandwidth of several to tens of nanometres. This type of filter uses the acousto-optic effect to diffract and shift the frequency of light using sound waves, usually a radio frequency (RF) signal, and the selected wavelength is determined by Eq. 4.1.

$$\lambda = \frac{\Delta n V}{f} [\sin^2 2\theta_i + \sin^4 \theta_i]^{1/2} \quad (4.1)$$

where the selected wavelength ( $\lambda$ ) is a function of the difference in the refractive indices due to birefringence ( $\Delta n = n_i - n_d$ ), the frequency of the applied RF signal ( $f$ ), the incident angle ( $\theta_i$ ) between the source laser beam and the crystal material to be modulated in the radio frequency of  $f$  and the speed of acoustic waves in the crystal material ( $V$ ).

The AOTF device is used to rapidly and dynamically select a specific wavelength from the broadband white laser source. As the applied RF frequency on the AOTF device is varied, the filtered wavelength changes, and the “tuning” of the wavelength costs typically tens of microseconds or less, which is four orders of magnitude faster than the LCTF device. It is ideal for future terrestrial and low-speed mobile HSL development with satisfactory operation efficiency.

The AOTF-HSL system is designed based on the schematic illustration in Figure 4.9. The upgraded laser source is a YSL© SC-OEM SCL from YSL Photonics with a maximum power of a single pulse exceeding 1.9  $\mu$ J. The pulse rate of the SCL is 0.01 MHz-1 MHz with a 2-3-ns full width at half maximum (FWHM) over the wavelength range (450-2400 nm). The beam divergence is 0.2 mrad, and the beam diameter is 10 mm. By considering the eye-safety issue, the ultra-wideband laser pulse emitted from the MOF is first filtered by the AOTF device (YSL© AOTF-Pro model), which is a wavelength selection module based on the

acousto-optic crystal. A beam expander is used to collimate the filtered beam with a high divergence angle before being transmitted to the object. Instead of the off-axis parabolic mirror used in the LCTF-HSL system, a Cassegrain telescope (with a 700-mm focal length and a 100-mm aperture diameter) collects the scattered laser pulses from the targets. The AOTF-HSL system tunes its outputs with a 10-nm spectral resolution, resulting in a set of 51 channels of spectrally resolved waveform echoes covering 500 nm-1000 nm for the sampling points on the target.

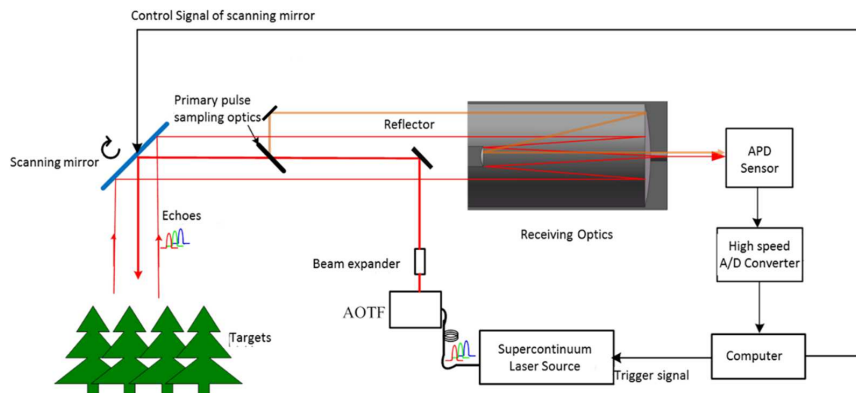


**Figure 4.9** Schematic setup of the AOTF-HSL system

Two tests were carried out to evaluate the range precision and the precision of the collected spectral profile of the designed AOTF-HSL system, which was installed on a 2-dimensional turntable for the field test, as Figure 4.10 shows. The range precision or stability was evaluated instead of the range accuracy by measuring the same range (37.50 metres) of 4 standard greyboards (20%, 40%, 70%, and 100%) with perpendicular laser beams. Also, 37.50 metres was measured by a commercial Leica laser telemeter (Leica D8) by measuring the range between the receiving optics (Cassegrain telescope) and the targets, which was used as the referenced range to evaluate the range performance.

Aloe (*Aloe arborescens* Mill.), dracaena (*Dracaena Angustifolia*), rubber (*Ficus elastica* Roxb. ex Hornem.) and Radermachera (*Radermachera hainanensis* Merr.) plants were selected for the spectral profile test due to their various leaf properties. The continuous spectral profiles with 10-nm resolution were collected from 6 different leaves (four green-leaf samples and two yellow-leaf samples) of 4 species plants in a range from 500 nm to 1000 nm assisted with a white reflectance standard with 99% reflectivity. The collected spectral profiles were compared with the reference data collected by the SVC spectrometer. The distance between the plants and the AOTF-HSL system was approximately 6 metres to collect better SNR ratio waveforms, especially in the 500-650 nm range.



**Figure 4.10.** AOTF-HSL system for the field test on a two-dimensional turntable.

## 4.2 Range Results

In this dissertation, the range measurement of the HSL is based on measuring the ToF of transmitted short ultra-broadband laser pulses. The recorded waveforms with post-processing algorithms measure the ToF, for example, by simple maximum Gaussian fitting to extract the pulse transmission time and pulse-receiving time. By subtracting the pulse transmission time from the pulse-receiving time, the ToF can be measured. The measured ToF is multiplied by the speed of light to obtain the range, as shown in Eq. 4.2.

$$R = \frac{c \times \Delta t}{2} = \frac{c \times (t_r - t_t)}{2} \quad (4.2)$$

where  $R$  is the range between the target and LiDAR,  $c$  is the speed of light,  $\Delta t$  is the time of flight, and  $t_r$  and  $t_t$  are the epochs of the pulse transmission and pulse-receiving times, respectively.

To carry out the range calculation correctly and with high accuracy, the speed of the light is known with high precision. However, the speed of light is affected by various environmental parameters, such as temperature, pressure, and humidity. Thus, atmospheric correction should be considered if highly accurate range measurements are required.

Laser ranging of HSL is accomplished by measuring the ToF of a “white” laser signal from the supercontinuum laser transmitter to the target and back to the receiver. For all HSL instruments investigated in this research, the laser signal

is pulsed. As mentioned above, the range to the target R is subsequently counted from the ToF ( $\tau$ ) measurement and the Eq. 4.3 can be modified to

$$R = C_g \frac{\tau}{2} = \frac{C_o}{n_g} \frac{\tau}{2} \quad (4.3)$$

where  $C_g$  is the speed of light in the medium in which the laser pulsed is propagating, and  $\tau$  is the group velocity in the medium at the selected wavelength for the HSL range. The group velocity differs from the speed of light in a vacuum ( $C_o$ ) by a factor of  $n_g$ , which is called the group velocity index of refraction. The group velocity index in the air is a function of temperature, pressure, and humidity. Moreover, it exhibits high stability and only small fractional changes with changes in the atmospheric parameters. Therefore, such minor changes are generally described in units of ppm (parts per million). For example, a change of 100 ppm in  $n_g$  results in a range measurement of 100 mm at a target range of 1000 metres at the selected wavelength. One issue should be addressed here: the atmospheric influence on the index of refraction at different wavelengths may vary. The following simplified formula can describe the group refractivity  $N_g$  determined by Eq. 4.4

$$N_g = 287.6155 + \frac{4.88660}{\lambda^2} + \frac{0.06800}{\lambda^4} \quad (4.4)$$

at the conditions of 0 °C, standard atmosphere and 0% relative air moisture, where  $\lambda$  is the laser wavelength in  $\mu\text{m}$ .

The group refractivity at ambient moist air for a given temperature T (in Kelvin), the pressure P (in millibars) and the water vapour pressure E (in millibars) is

$$N_L = \frac{273.15}{1023.25} \frac{N_g P}{T} - \frac{11.27 E}{T} \quad (4.5)$$

The group index of refraction  $n_g$  in Eq. 3 can be described as

$$n_g = 1 + N_L 10^{-6} \quad (4.6)$$

In general, the influence of the three aforementioned atmospheric parameters on the range measurements can be concluded with the following approximations for practical usage:

- a change in temperature of 1 °C results in a 1-ppm correction, and as the temperature decreases, the light will propagate slower;
- a change in air pressure of 10 millibars yields a correction of 2.7 ppm, and higher pressure results in a slower speed of light;
- a variation in moisture from 0% to 100% results in a correction of 0.5 ppm, which can be ignored in most cases.

HSL systems are usually tested in a laboratory environment. The maximum range measurement is less than 50 m, and the best range resolution equals 7.5 mm (20-G/s sampling rate). Assuming that the temperature has been measured with an accuracy of  $\pm 5$  °C, the pressure within  $\pm 50$  millibars, the total atmospheric correction is 10 ppm  $\pm$  13.5 ppm. A target range of 50 metres results in a change of 0.1175 mm, which is small compared to the 7.5-mm range resolution. However, for further airborne, even spaceborne applications, the atmospheric correction should be carefully modelled.

The range results from various HSL systems are presented in the following context to evaluate the capability of spatial information collection.

#### 4.2.1 Range results of optical-filter-based systems

##### A: Two-channel optical-filter-based HSL

The results of the ToF experiment are illustrated in **Error! Reference source not found.**, which shows the echoes from the two APD sensors at both target distances. Assuming the peak position of the echo waveform represents the range of the target, both channels indicate a range of 11.625 metres and 10.665 metres (which correspond to 77.5 ns and 71.1 ns, respectively, as the measured time-of-flight values). The infrared band echo (800-nm) is higher than that of the green band (600 nm), which is caused by the combined effect of the more substantial laser output and the higher spectral response of the APD sensor on the 800-nm band.

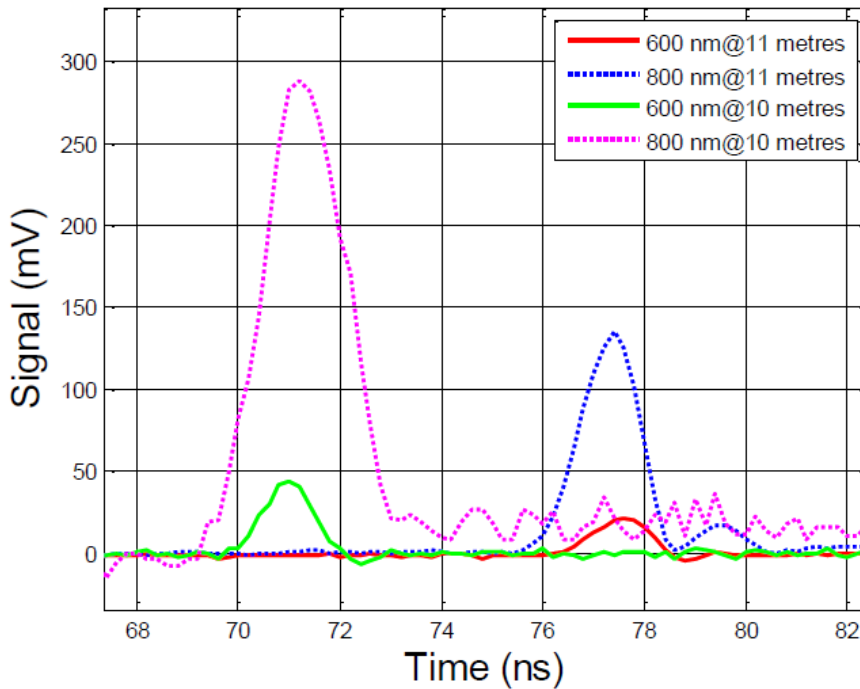


**Figure 4.11** The echoes of the two-channel hyperspectral LiDAR from the Spectralon® reflection board at ranges of 10 and 11 metres.

The measured range difference between the two measurements is slightly less than 1 metre, while the actual difference is 1 metre during the experiments. The following are explanations for what may have caused the inaccurate distance measurement:

1. The sampling rate of the oscilloscope is five giga-points per second, i.e., the range resolution of the system, in this case, is 3 cm (0.2 ns), resulting in a 3-cm random quantisation error for every single range measurement and a maximum

error of 6 cm for the range difference measurement. Averaging multiple waveforms from the same target at the same range can improve the SNR for better range performance.

2. The bandwidth of the oscilloscope is 500 MHz, which is slightly less than that of the echoes, and this discrepancy may partly distort the echo waveform.

3. The oscilloscope is triggered by the rising edge of the transmitting pulse signal collected by the photodiode at a fixed trigger level. The power of the transmitting pulse varied during the experiment. The increase in the echo amplitude is not proportional to the distance, as can be observed in Figure 4.11 by comparing the echoes at different distances. The variance in the transmitting power caused a shift in the rising edge of the triggered signal. As a result, an extra error is introduced into the distance measurements.

4. The cement table on which the prototype system is set is not meant for precise optical measurements. Consequently, the reference measurement of the distance is carried out on a rough surface by a measuring tape, which may introduce some degree of error. A commercial laser telemeter is recommended to collect the reference ranges.

#### **B: 17-channel optical-filter-based HSL**

Table 4.4 shows the standard deviations of the distances of the different spectral channels, which are obtained from the averaging ten calcite sample measurements for each spectral channel. The calcite sample was measured at a range of 3 metres. The Si APD and the InGaAs APD are used to detect the reflected laser pulses of different spectral bands, to expand the spectral range of HSL to SWIR. An extra amplifier was used to amplify the signals collected by the InGaAs APD due to its lower sensitivity. The range measurement differences between the different spectral channels are minor, especially after averaging ten measurements. Thus, we compare the standard deviation (STD) of the range measurements and list the results in Table 4.4. From the table, it is observed that the distance measurements of the APD sensors fabricated in different material are similar to each other, considering that the range resolution is 3 cm and that the additional amplifier does not introduce extra range noise in the range measurements. The range resolution is determined by the sampling rate of the oscilloscope (5 GHz), and the time interval is 200 ps.

**Table 4.4.** Standard deviations of the distance of each spectral channel of the 17-channel optical-filter-based HSL system (calcite case)

Channel (VNIR) Si APD	STD /cm	Channel (SWIR) InGaAs APD	STD /cm
1	0.66	10	0.12
2	0.14	11	0.08
3	0.27	12	0.94
4	0.97	13	0.76
5	0.31	14	0.81
6	0.36	15	0.77
7	0.07	16	1.10

8	0.45	17	0.03
9	0.41		

#### 4.2.2 LCTF-based HSL

The range accuracy was evaluated by measuring the vegetation target rather than a flat reflection board. A green plant was placed in front of the LCTF-HSL approximately 3 metres for ranging performance evaluation. A group of processed waveforms of all the spectral channels collected by the LCTF-HSL are shown in Figure 4.12, and the sampling rate of the selected oscilloscope was 10 GHz, which equalled a 1.5-cm range resolution. The distance was measured by detecting the position of the maximum amplitude of the transmitting pulse (as shown in the sub-figure of Figure 4.12) and the echo waveform to determine the pulse flying time of each spectral waveform. From Figure 4.12, it could be observed that the spectral power density from 450 nm-550 nm was considerably lower than 550 nm-720 nm.

Meanwhile, the sensitivity of the silicon APD sensor from the 450 nm-550 nm spectral range was also inferior. Only echoes from 550 nm-720 nm were utilised for analysis to prevent the saturation of the waveform, as in previous research. Table 4.5 shows the distance measurements from different spectral channels starting from 550 nm with 10-nm bandwidths. The difference in the range measurements from the different spectral channels was negligible, and the 4.5-cm range difference among different wavelengths indicated that the authentic range might be between 3.06 m and 3.105 m. With the current optical setup, the referenced truth of range was not available; however, the range measurement can be calibrated with traditional methods. The standard deviation of the range measurements of the 18 spectral channels was approximately 1.72 cm. We found that both the stability and variance in the range measurements of all spectral channels are worse than those of the optical filter-based solution. The LCTF's internal design was supposed to contribute to the uncertainty in the range measurements due to its time-multiplexing characteristics.

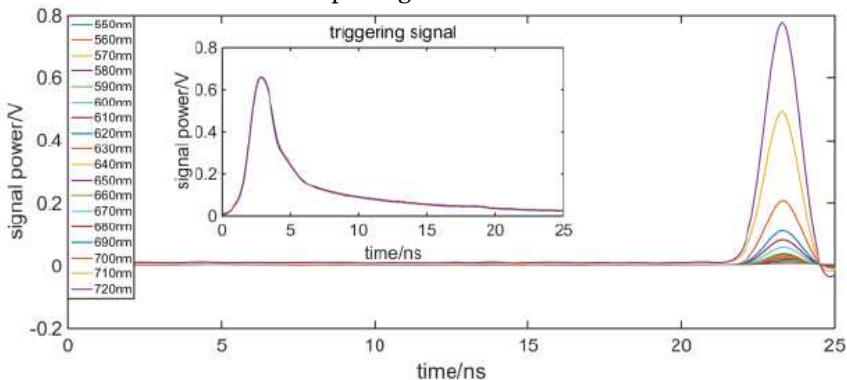


**Figure 4.12.** Processed spectral waveforms of a green plant collected by the 18-channel LCTF-HSL system

**Table 4.5** Range measurements from the different spectral channels

Wavelength/nm	Range/m	Wavelength/nm	Range/m
550	3.105	640	3.075
560	3.105	650	3.075
570	3.105	660	3.060
580	3.105	670	3.075
590	3.105	680	3.060
600	3.090	690	3.075
610	3.105	700	3.075
620	3.075	710	3.075
630	3.060	720	3.075

#### 4.2.3 AOTF based HSL

Standard greyboards were placed at a distance of more than 37.50 metres from the AOTF-HSL to test the uniformity of the range measurements over the spectral channels. For each greyboard, the centre point of the greyboard was selected for the range measurement because of perpendicular laser beams. The range precision was evaluated based on the range measurements covering the full spectrum (51 spectral channels). For each spectral channel, 16 measurements (waveforms) were collected under the same conditions, and the range result of each spectral channel is the average result of its 16 measurements. The ToF measurements of different spectral channels were calculated based on the collected waveforms recorded at ten giga-samplings per second with a simple maximum algorithm.

The range is calculated based on the simple maximum algorithm by subtracting the peak position of the echo pulse with the corresponding peak positioning of the primary pulse from the original waveform. It can be observed from Figure 4.13 that the range measurements of the standard greyboards differ from 37.53 m to 37.575 m and that the variances of the range measurements over the 36 channels are 2.5 mm (20%), 7.2 mm (40%), 7.5 mm (70%) and 7.1 mm (100%). Promising uniformity in the range measurements over the spectral channels can be observed for the selected single greyboard. The range error with any single board is 1.5 cm, which equals the random quantisation error of a 10-GHz sampling rate. The LSB error in the A/D converter for digitising the waveform is the only stochastic noise source that affects the range measurements for any single greyboard. However, the range error increases to 4.5 cm when all the range measurements of all the greyboards are calculated.

One issue that must be addressed is that due to the current AOTF-HSL system configuration, the authentic value of the range to the standard reflectivity board is not available. It can be concluded from the conducted range evaluation that with ten giga-samplings per second and the derived range resolution from the ToF measurements for different bands is 1.5 cm, which might be insufficient for some applications, and more advanced post-processing algorithms should be investigated to improve the range resolution.

The random range error (maximum of 45 mm) from different reflectivity boards should also be mitigated by more sophisticated waveform processing if

better range precision is needed, e.g., some forms of the averaging algorithm to increase the SNR and Gaussian fitting. However, the tendency that can be observed is that the range measurement increases with decreasing target reflection. In Figure 4.13, the measurements of the spectral channels from 500–650 nm are missing due to the low sensitivity of the APD sensor and the low transmitted power intensity of the SCL below 650 nm.

The range stability results evaluated in this section raise another concern of range calibration for HSL offering continuous spectral data.

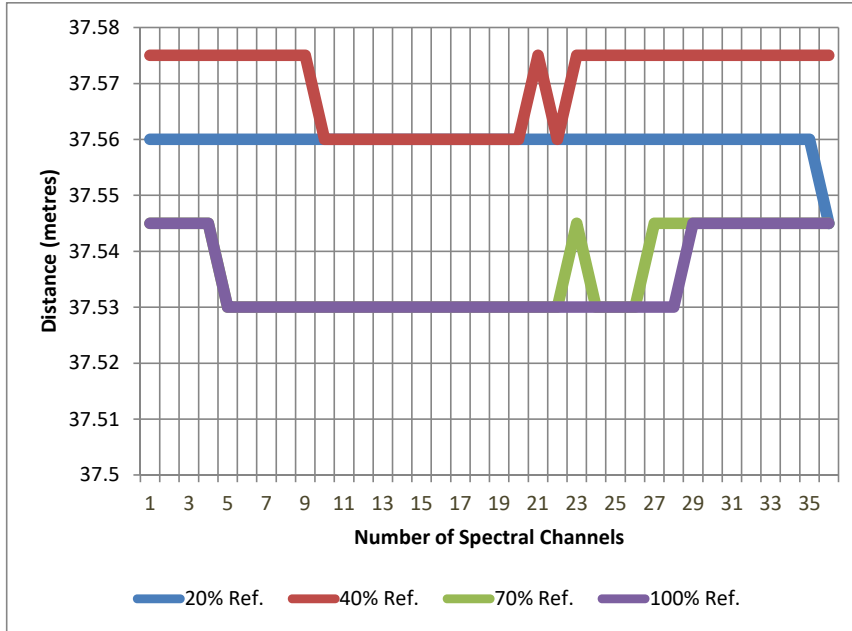


**Figure 4.13** Range measurements of the AOTF-HSL system from 650 nm to 1000 nm on four standard targets with different reflectivities at 37.5 metres from the AOTF-HSL system.

### 4.3 Spectral Results

The LiDAR intensity refers to the received power of the returned pulse from the targets. Some intrinsic and extrinsic parameters always influence the LiDAR intensity; more specifically, the intrinsic parameters include the power of the emitted laser beam and the atmospheric attenuation, and the extrinsic parameters include the reflectivity of the target, the transmitting range and the incident angle. By considering these factors, a standard model is given in Eq. 4.7.

$$P_R = \frac{\pi P_E \rho \cos(\theta)}{4R^2} \eta_{stm} \eta_{sys} \quad (4.7)$$

Where  $P_R$  refers to the received signal power;  $P_E$  is the emitted signal power,  $\rho$  is the reflectance of the target;  $\theta$  is the incident angle between the target surface normal vector and the laser beam incident on the target.  $R$  is the range between the target and the LiDAR system.  $\eta_{stm}$  and  $\eta_{sys}$  describe the systematic and atmospheric factors, respectively.

Assuming there are  $N$  spectral channels available with this HSL configuration (by considering the data storage and practical hardware investment, two to several tens of channels are selected in this dissertation), and thus, the received power at wavelength  $\lambda$  can be written as Eq. 4.8 according to the intensity model of Eq. 4.7:

$$P_{\lambda}^R = \frac{\pi P_{\lambda}^E \rho_{\lambda} \cos(\theta)}{4R^2} \eta_{\lambda}^{stm} \eta_{\lambda}^{sys} \quad (4.8)$$

where  $P_{\lambda}^R$  is the received signal power,  $P_{\lambda}^E$  is the emitted signal power, and  $\rho_{\lambda}$  is the reflectance of the target.  $\theta$  refers to the incident angle between the target surface and the laser beam projected on the target.  $\eta_{stm}$  and  $\eta_{sys}$  describe the systematic and atmospheric factors, respectively.  $R$  refers to the range between the target and the LiDAR system.

All the spectral channels of the HSL system have an identical incident angle  $\theta$  and range  $R$  for a selected target. A ratio is defined in by Eq. 4.9 using a channel as a reference (the channel selection can be random).

$$ratio_{\lambda} = \frac{P_{\lambda}^R}{P_{ref}^R} = \frac{P_{\lambda}^E}{P_{ref}^E} \frac{\rho_{\lambda}}{\rho_{ref}} \frac{\eta_{\lambda}^{stm} \eta_{\lambda}^{sys}}{\eta_{ref}^{stm} \eta_{ref}^{sys}} \quad (4.9)$$

Where  $ratio_{\lambda}$  is the defined ratio for a channel with wavelength  $\lambda$ ;  $P_{ref}^R$  is the received signal power of the selected referenced spectral channel;  $\eta_{ref}^{stm}$  and  $\eta_{ref}^{sys}$  describe the systematic and atmosphere factors, respectively, for the reference channel;  $\rho_{\lambda}$  is the reflectance of the target for a spectral wavelength  $\lambda$ ;  $P_{\lambda}^R$  is the received signal power of spectral channel  $\lambda$ ;  $\eta_{\lambda}^{stm}$  and  $\eta_{\lambda}^{sys}$  describe the systematic and atmosphere factors, respectively, for the spectral channel  $\lambda$ .

According to Eq. 9, the ratio is determined by three major parts: the emitted power of the laser beam, the reflectivity of different materials for distinct spectral wavelengths, and the systematic and atmosphere factors. Figure 4.14 shows the power density for corresponding spectral wavelengths ranging from 450 nm to 2400 nm of a selected SCL, and the emitted signal strength varies for different spectral wavelengths. However, the laser source has an almost fixed power density curve, and the emitted power strength is stable.

$\frac{P_{\lambda}^E}{P_{ref}^E}$  can be addressed a constant value,  $k_{\lambda}$ , which is associated with the specific spectral wavelength.

Concerning the systematic and atmospheric factors, the  $\frac{\eta_{\lambda}^{stm} \eta_{\lambda}^{sys}}{\eta_{ref}^{stm} \eta_{ref}^{sys}}$  can also be regarded as a constant value,  $\eta_{\lambda}$ , which differs slightly in distinct spectral wavelengths. Hence, Eq. 4.9 can be simplified as follows:

$$ratio_{\lambda} = k_{\lambda} \frac{\rho_{\lambda}}{\rho_{ref}} \eta_{\lambda} \quad (4.10)$$

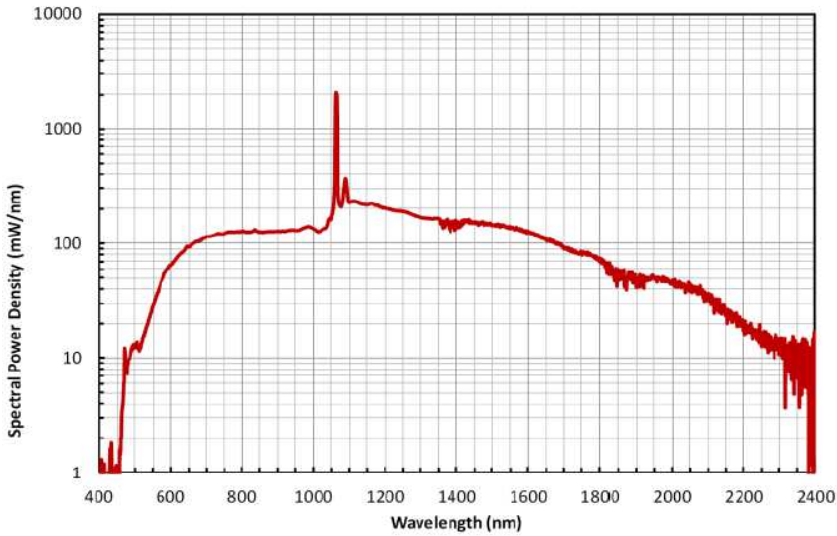


**Figure 4.14** The spectral power density of the SC laser source

Such a ratio can evolve into more complex forms, such as the NDVI. The NDVI is defined as follows:

$$\text{NDVI} = [\text{NIR} - \text{RED}] / [\text{NIR} + \text{RED}], \quad (4.11)$$

where NIR is the target reflectance within the near-infrared wavelength range, and RED is the reflectance within the visible wavelength range. Compared with currently available dual- or multi-wavelength LiDAR applications based on several monochromatic laser sources with fixed wavelengths, a system employing a supercontinuum laser source is different. It presents a more flexible and optimal spectral channel selection because the wavelengths can be arbitrarily selected from within the supercontinuum (or detector) wavelength range of its source. The bandwidth of the spectral channels can be optimally modified based on the specific requirements of a given application.

#### 4.3.1 Forestry inventory

Figure 4.15 shows the multiple echoes from the target spruce tree and the Spectralon panel in the experiment by the two-channel optical-filter-based HSL system. Since the transmitting power varied during the test, we calculated the results by averaging the 16 measurements to mitigate the effect of this variation and to improve the SNR. We observed the following phenomena:

1. The prototype system is capable of processing multiple hits, which it can extract from multiple targets from one echo. It is a critical feature for forestry applications.
2. The difference in the NDVI for the Spectralon reflection board and the Norway spruce tree sample is visible in this experiment (see Figure 4.16). The NDVI of the Norway spruce tree is approximately 0.8, and the curve is moderately flat. Likewise, the NDVI of the Spectralon panel is relatively close to 0, which is in

agreement that from the Spectralon panel with a flat reflection rate at all wavelengths. The authors approximated the near-infrared and visible parts of the spectrum with reflectance values at 800 nm and 600 nm, respectively. The spikes in the NDVI curve for the Spectralon panel at 74 and 77 ns are caused by the uneven spectral response feature between the two APD sensors, which can be calibrated when conducting future research. The results are in agreement with earlier observations of high NDVI values for vegetation.

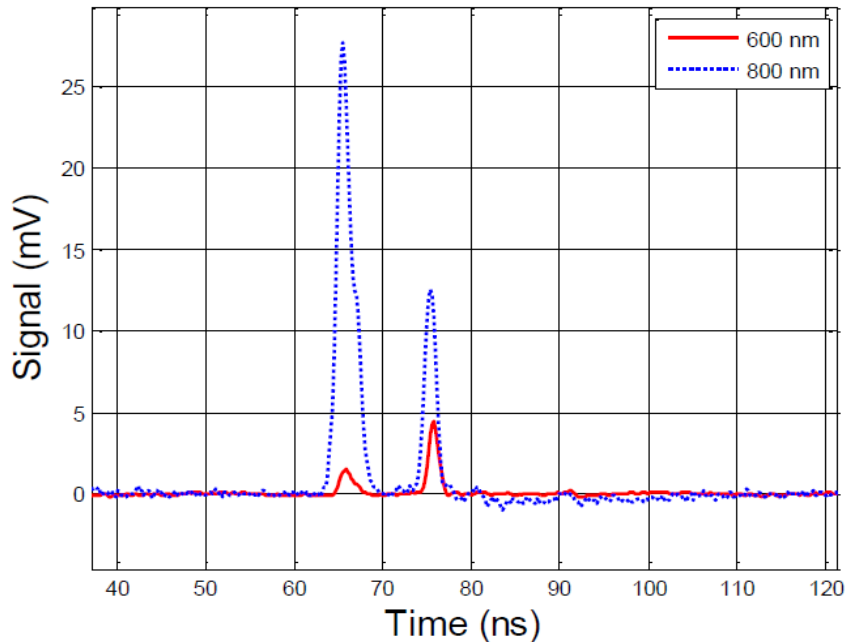


**Figure 4.15** The echoes of the two-channel hyperspectral LiDAR system for two targets (Spectralon panel behind the Norway spruce tree), averaged across 16 measurements.

Nevertheless, these results demonstrate the feasibility of the hyperspectral range finder for simultaneous range and spectral measurements: the instrument is capable of discriminating between a Norway spruce target and inorganic material based on the NDVI while simultaneously obtaining the target's range.

In addition to the NDVI, more vegetation indices can be obtained from the measured hyperspectral point cloud, such as the water concentration index (Peñuelas et al., 1993) and the modified chlorophyll absorption ratio index (Haboudane et al., 2004), and more complex and precise models can be set up when both the number of spectral channels and the spectral resolution increase, as Figure 4.17 shows.

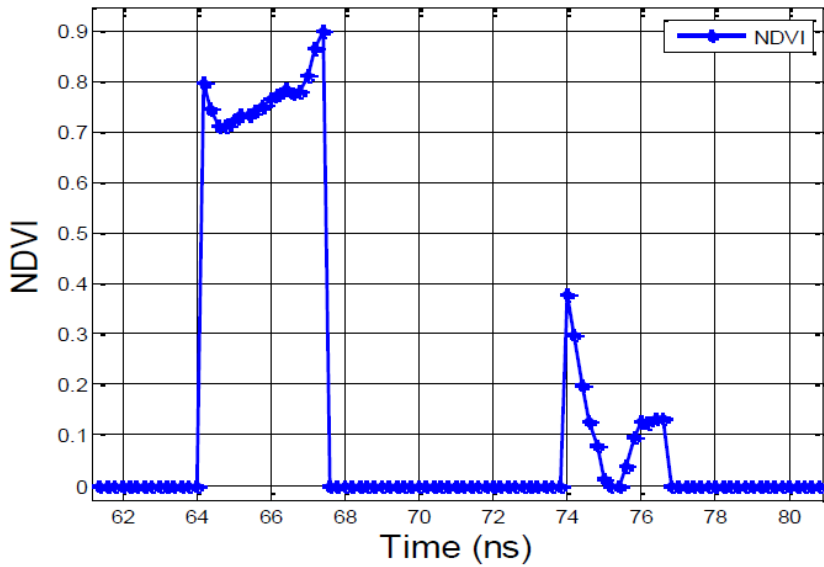


**Figure 4.16** The NDVI of the echoes from the two-channel hyperspectral LiDAR system for two targets (Spectralon panel behind the Norway spruce tree), averaged across 16 measurements and the echoes after normalisation.

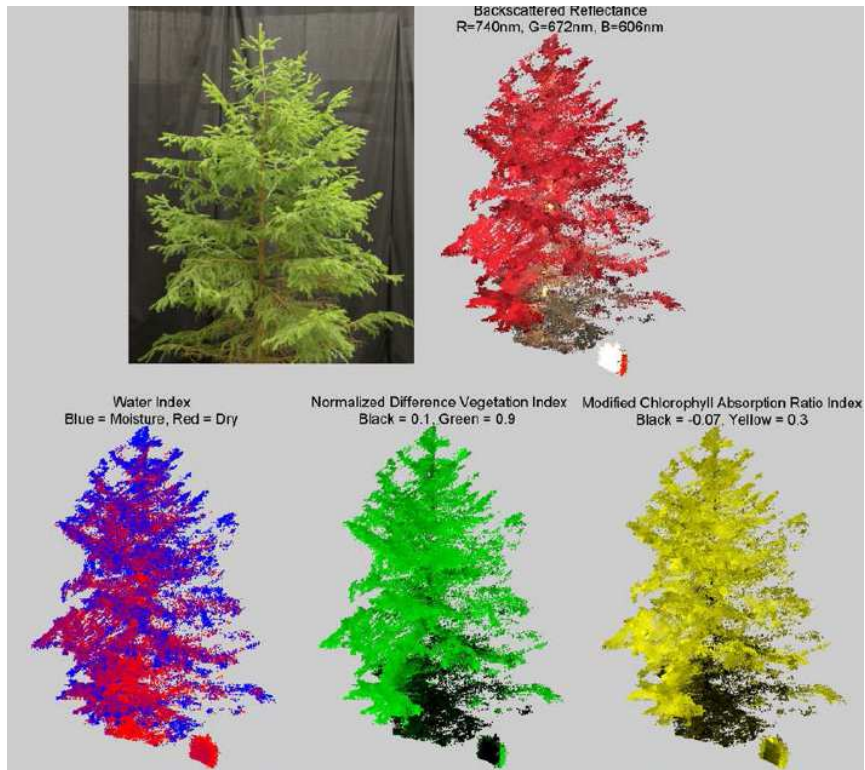


**Figure 4.17.** From the upper-left corner: (1) A photograph of the Norway spruce, and 3D point clouds demonstrating (2) the backscattered reflectance (3) the water Index, (4) the NDVI and (5) the MCARI

### 4.3.2 Plant Science

#### A: Spectral profile collected by the 8-channel optical-filter-based HSL system

Figure 4.18 presents the spectrum reflectance (blue) of the three *Scindapsus* plants against the reference measurements collected by the spectrometer. From Figure 4.18, two healthy *Scindapsus* plants (one plant was grown in soil, and the other plant was grown in water) exhibit a similar spectrum profile. However, the *Scindapsus* grown in water has higher reflectance at 800 nm. The dry *Scindapsus* plant presents a different spectrum profile, which has a higher reflectance (0.6) from VNIR to SWIR. It can also be observed that the HSL measurement mainly coincides with the spectrometer measurement. However, the variances between the HSL and the spectrometer measurements are more noticeable. The explanations for the variances are 1) For a flat object, such as the reflection board, the variance is minor; 2) for the plants, the sample point on the target might be slightly different during the test due to the measurement procedure that all objects are measured by the HSL system first and then by the spectrometer; and 3) the incidence angle might also vary during the test.

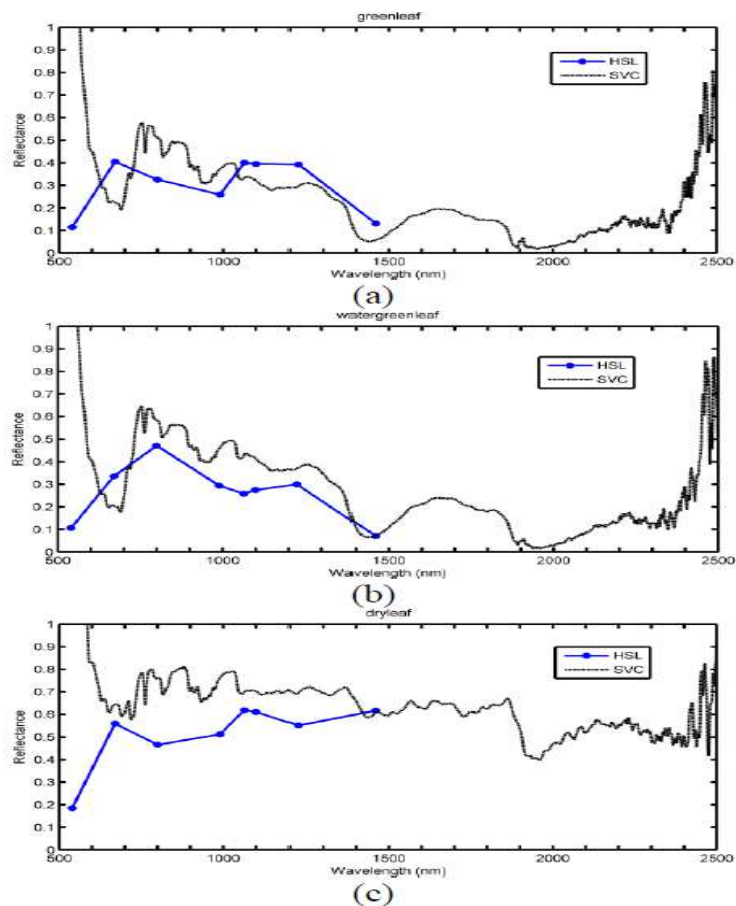


**Figure 4.18.** The spectrum reflectance (blue) of the *Scindapsus* plants ((a) a healthy *Scindapsus* plant grown in soil, (b) a healthy *Scindapsus* plant grown in water, (c) dry and withered *Scindapsus* plant) collected by the HSL and by the spectrometer

### B: Spectral profile collected by the LCTF-HSL system

Researchers suggest that the cellular structure and chlorophyll content of vegetation determine a major part of the reflectance values and influence the shifting behaviours of the red-edge position. The red-edge position is usually located in the red-band spectrum from 680 nm to 720 nm because chlorophyll contained in vegetation absorbs a large amount of light in the visible spectrum and becomes nearly transparent at wavelengths greater than 700 nm. Various experimental results have revealed that the red-edge position shifts towards longer wavelengths when a plant is healthy and has adequate chlorophyll content; when it suffers from diseases resulting in insufficient chlorophyll content, the red-edge position shifts towards shorter wavelengths. The red-edge-shifting behaviours are also confirmed by researchers utilising spectral reflectance measurements obtained from passive airborne sensors. This phenomenon has been widely employed in vegetation parameter estimation or vegetation biomass modelling (Darvishzadeh et al., 2009).

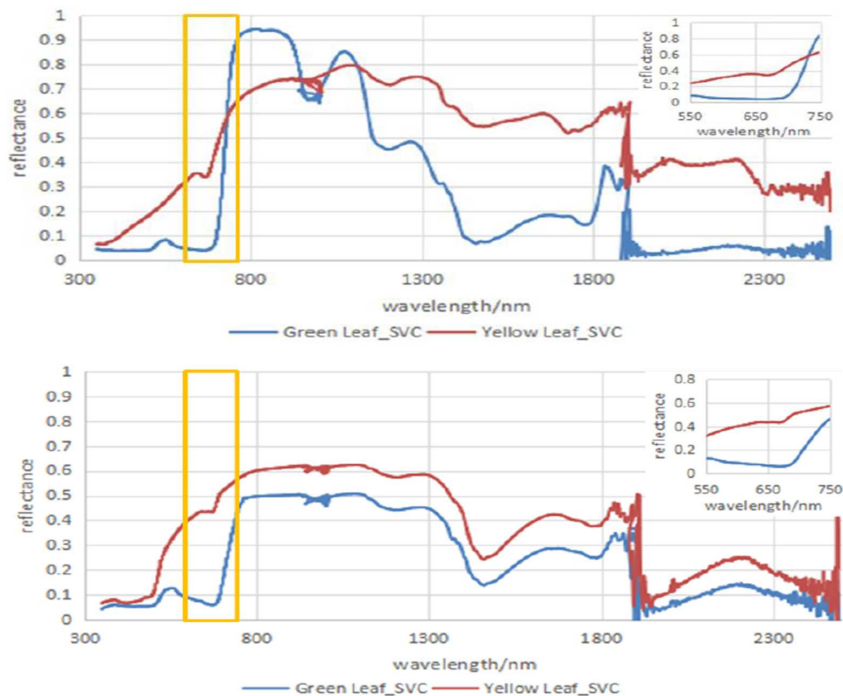
Red-edge position detection experiments with different vegetation were conducted under controlled laboratory conditions with the LCTF-HSL system. The results were evaluated through the spectrometer measurements. The LCTF-HSL system operated with wavelengths ranging from 550 nm to 720 nm at a 10-nm spectral resolution. Two types of vegetation (aloe and dracaena, shown in Figure 4.19) with yellow and green leaves were measured by the two different systems individually (LCTF-HSL and SVC spectrometer) in the laboratory.

Figure 4.20 illustrates the reflectance measurements obtained from the SVC spectrometer. In the figures, the red line represents the reflectance of the green leaf with adequate chlorophyll content; in contrast, the blue line represents the reflectance of the yellow leaf with insufficient chlorophyll content. By observing the reflectance curves, the following results can be observed:

- 1) The red edge of the yellow aloe leaf was 670 nm with a small red-edge slope, and the red-edge position for the green aloe leaf was 690 nm with a more significant red-edge slope. The yellow rectangle marks the spectral range presented in Figure 4.20 (top) with zoomed-out details in the sub-figure;
- 2) The red-edge position for the yellow dracaena leaf was 670 nm with a small red-edge slope, and the red-edge position for the green leaf was 685 nm with a more significant red-edge slope. The yellow rectangle marks the spectral range presented in Figure 4.20 (bottom) with zoomed-out details in the sub-figure.



**Figure 4.19.** Aloe (left) and dracaena (right) plants measured in the laboratory experiments with the LCTF-HSL system



**Figure 4.20** Spectral reflectance curves of the aloë (top) and dracaena (bottom) plants collected by the SVC spectrometer

Supported by the five types of whiteboards (5%, 20%, 40%, 70%, and 99% reflectivity), the spectral reflectance collected by the LCTF-HSL system can be calculated. Figure 4.21 presents the comparison of the reflectance collected by the LCTF-HSL system with the reference value acquired by the SVC spectrometer. The red and blue curves represent the reflectance of the yellow and green leaves, respectively, of each plant obtained by the active LCTF-HSL sensor. The purple and green curves represent the reflectance of the yellow and green leaves of the aloë and dracaena plants, respectively, achieved by the passive SVC spectrometer. By analysing the spectral data from the spectrometer, the following results regarding the red edge were obtained:

1. The red edge of the yellow aloë leaf was 660 nm with a small red-edge slope, and the red-edge position for the green aloë leaf was 690 nm with a more significant red-edge slope from the HSL measurements.
2. The red-edge position for the yellow dracaena leaf was 670 nm with a small red-edge slope, and the red-edge position for the green dracaena leaf was 680 nm with a more significant red-edge slope from the HSL measurements.
3. The two spectral profiles of green leaves collected by LCTF-HSL coincided well with the reference from the overall observed spectral range (550 nm-720 nm), and the difference between the spectral profiles collected with the different active and passive sensors was trivial.
4. The magnitude of the two spectral profiles of yellow leaves collected by LCTF-HSL was slightly higher than the reference value, and the tendency was more evident in the red-band spectrum.

5. Besides, the shift of the red-edge position could be observed from both the passive and active instruments, which shifted towards longer wavelengths for green leaves with high chlorophyll content and towards shorter wavelengths for yellow leaves with low chlorophyll content. The observed behaviour was identical to the results demonstrated in previous works, which indicates that the measurement results of the LCTF-HSL system were reliable for this application.

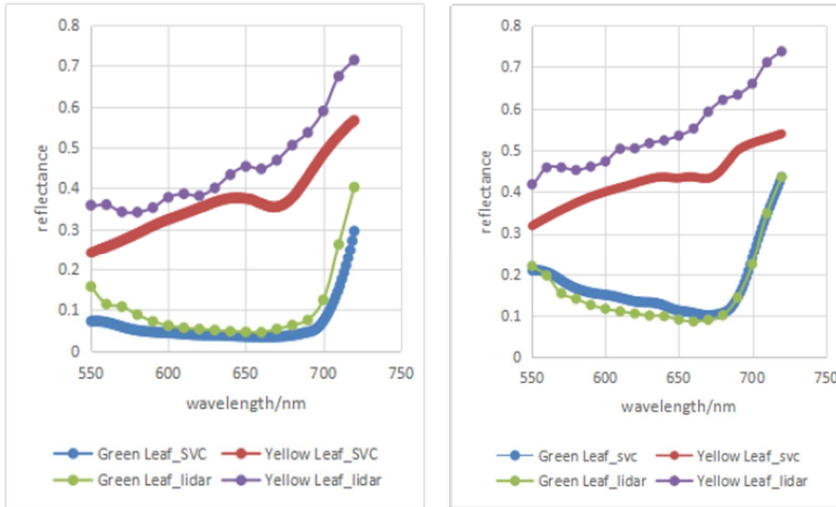


**Figure 4.21.** Comparison of the reflectances of the aloe (left) and dracaena (right) plants from the SVC spectrometer and LCTF-LiDAR system

### C: Spectral profiles collected by the AOTF-HSL system

For the spectral profile test cases, all plant targets shown in Figure 4.22 were measured at a 6-metre distance to ensure that all the spectral channels can collect reliable SNRs of the original waveforms because the sensitivity of the Si APD and the laser intensity of the selected SCL below 650 nm are low. The reference spectral profiles were collected by the SVC spectrometer using sunlight as the light source and were acquired at a 25-cm distance.

The reflectivity of each spectral channel was calibrated based on the method presented (Chen et al., 2019). Figure 4.23 shows the spectral profiles for six leaf samples from 4 species of plants. The “red edge” of the four green leaf cases can be easily discerned. For the yellow leaf cases, higher reflectivity can be observed compared with the corresponding green leaf cases due to the loss of chlorophyll. The four spectral profiles collected by the AOTF-HSL system from the green leaves of each plant are plotted against the reference curves collected by the spectrometer (in Figure 4.24), and we observe that with the proposed calibration method, the results from the AOTF-HSL system are more comparable to those from the spectrometer. The spectral profiles from the active HSL system and the passive spectrometer coincide with each other, especially for the “red edge”, referring to the rapid change region of vegetation reflectance or an inflection point in the reflectance slope in the red-band spectrum. The average spec-

tral differences (absolute value) of the four green leaves for the active and passive measurements are 1.37% (dracaena plant), 0.84% (aloe plant), 1.36% (rubber plant), and 0.77% (Radermachera plant). Figure 4.25 presents the spectral profiles collected from the yellow leaves of the dracaena and aloe plants against the corresponding spectrometer measurements. The average spectral differences are more substantial than those of the green leaf cases, specifically, 8.79% for the dracaena plant and 4.6% for the aloe plant.

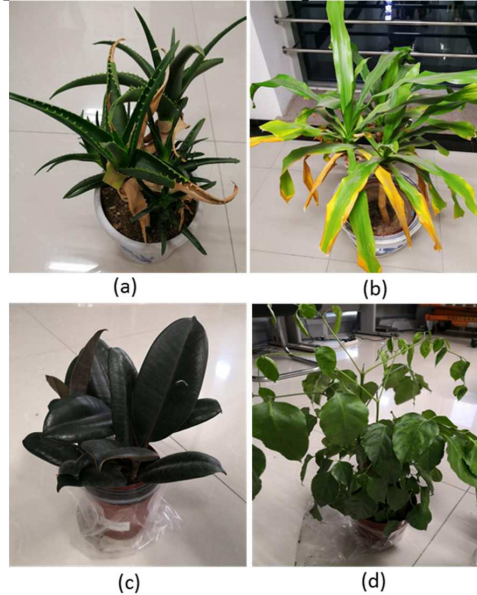


**Figure 4.22** Four plants used in the experiment: (a) an aloe plant with yellow and green leaves, (b) a dracaena plant with yellow and green leaves, (c) a rubber plant and (d) a Radermachera plant.

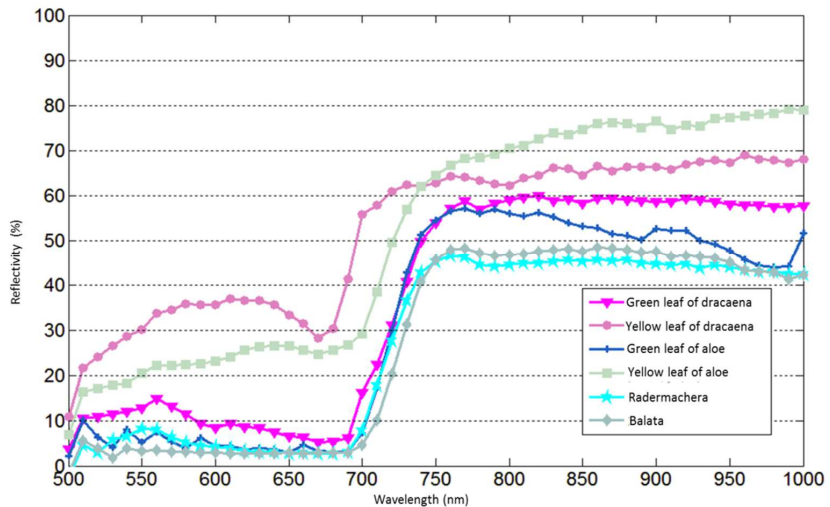


**Figure 4.23** AOTF-HSL-derived spectral profiles of 6 leaves from the four plant species (dracaena, aloe, rubber and Radermachera plants)

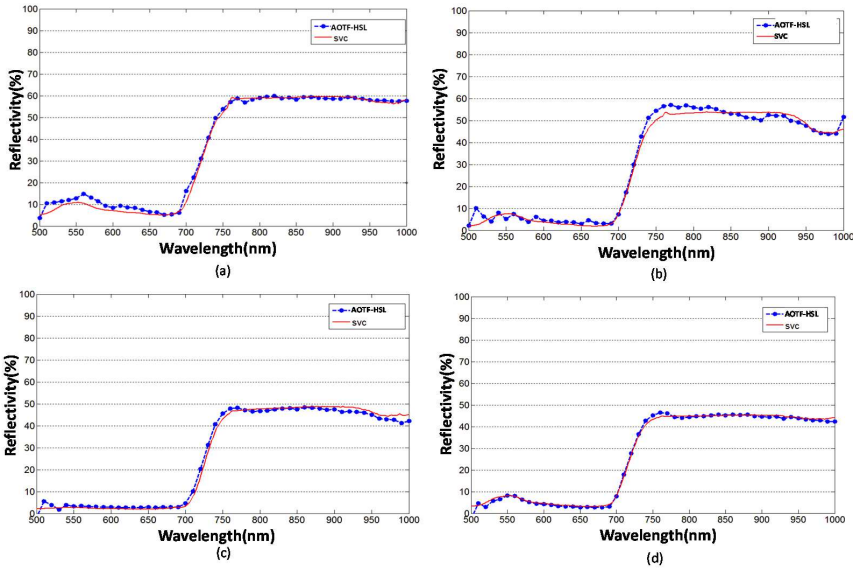


**Figure 4.24.** AOTF-HSL-derived spectral profiles of the green leaves from the (a) dracaena, (b) aloe, (c) rubber, and (d) Radermachera plants compared with the spectrometer measurements.

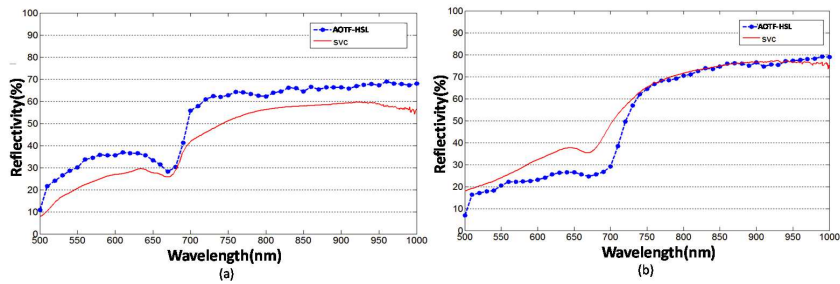


**Figure 4.25.** AOTF-HSL-derived spectral profiles of the yellow leaves from (a) the dracaena plant and (b) the aloe plant compared with the spectrometer measurements.

It can be observed from Figure 4.24 and Figure 4.25 that the backscattered reflectivity produced by the HSL system does not strictly follow the reference values. Three reasons may cause the discrepancies as a synthesised result of multiple factors. First, the illuminated surface area of the HSL system is smaller than the sampled area of the spectrometer (the diameter of the footprint is 12 mm), resulting in a 5.5-cm radius footprint with a 25° field of view for the selected module, and such a mismatch might introduce significant differences, especially if the non-uniformity of the yellow leaf is higher than that of the green leaf. Second, the uniformity of the green leaf is better than that of the yellow leaf, and thus, the location of the sampling area is critical, especially for the yellow leaf cases, and a minor difference exists between the two measurements. Third, the transmitted pulse energy of the SCL source might vary slightly, and according to the specifications of the laser source, the power stability of the SCL source is better than 1% [25]. Some modifications in the optics system should

be made to mitigate the discrepancies in the reflectance estimation, such as adding a beam expander to the exit of the broadband laser source to match the footprint size between two systems.

I compute the distributions of the reflectance from the green leaves of the four plants from the hyperspectral LiDAR system, compare them with the reflectance determined by the spectrometer data, and present the scatterplots of the reflectance from the AOTF-HSL system versus that from the SVC spectrometer in Figure 4.26 with a linear fit. Higher coefficients of determination ( $R^2 > 0.99$ ) in all four cases indicate that the extracted reflectance from the HSL system is highly correlated with the referenced results. For the four green leaf cases, the average value is close to 0.9949, which demonstrates the excellent fitness of the measurements from the two devices. Similar scatter diagrams of the yellow leaf cases from the dracaena and aloe plants are illustrated in Figure 27 and compared with the green leaf cases, the coefficients of determination are poorer ( $R^2 > 0.97$ ) but still promising. It can be preliminarily concluded that the reflectance results of the HSL system using the proposed calibration method are reliable.

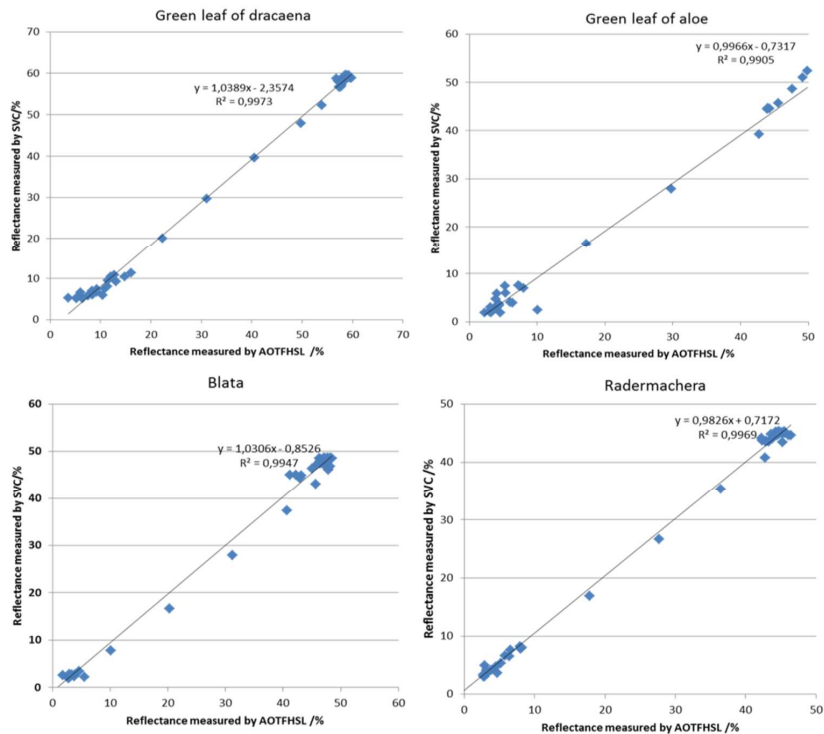


**Figure 2.** Scatter diagrams of the reflectance of the green leaf cases measured by the AOTF-HSL system and the SVC spectrometer.

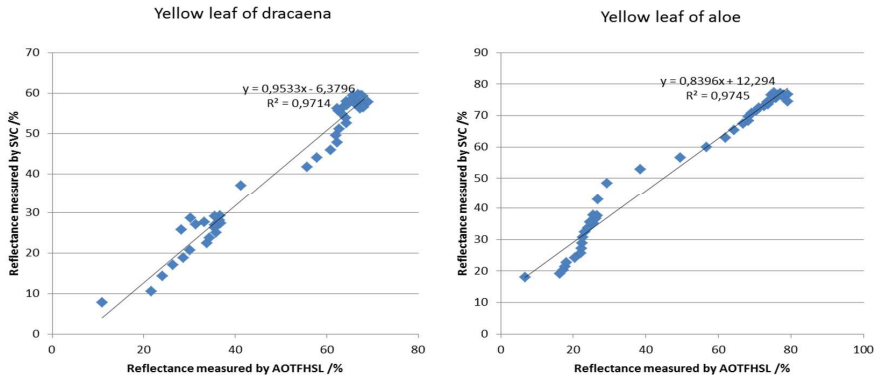


**Figure 4.27.** Scatter diagrams of the reflectance of the yellow leaf cases measured by the AOTF-HSL system and the SVC spectrometer.

### 4.3.3 Mining

I investigated the use of the HSL system for ore classification to explore the possibility of tunnel modelling or mining disaster prevention with the UGV platform (Chen et al., 2016). A plagioclase sample was measured with the 8-channel HSL system covering the VNIR to SWIR bands. The results (Figure 4.28) show that the HSL measurements coincide with the spectrometer measurements. Also, for 3D modelling and navigation, the HSL sensor, can be utilised for material classification with an extended spectral range (Chen et al., 2017). In other words, a 3D model with surface material information can be generated during the operation with a single HSL instrument, which might be financially beneficial for deep-space research. Thus, we also investigated the possibility of using HSL for ore classification.

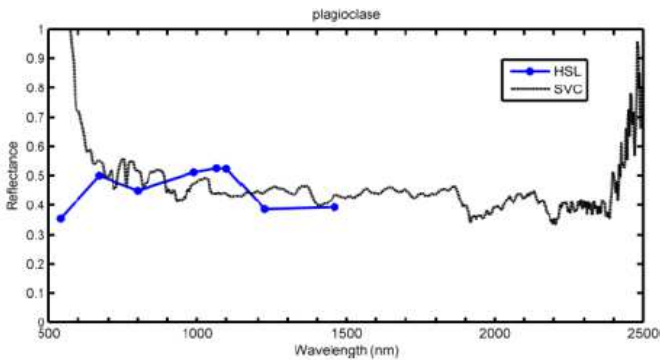


**Figure 4.28.** The spectrum reflectance (blue) of the plagioclase sample collected by the HSL system and by the spectrometer

The AOTF-HSL system collects the original waveforms, from which the hyperspectral reflectance values are calculated, and the calculated reflectance values are used as the input feature vectors of the classifiers. Figure 4.29 shows the initially reflected waveforms collected from the calcite ore. For ease of interpretation, the waveforms were separated into two groups based on their spectral

ranges [Figure 4.29 (a) 450–925 nm and Figure 4.29 (b) 1070–1600 nm]. After processing the raw waveform using Gaussian fitting for each wavelength, we can calculate the reflectance information of the ore samples using the whiteboard with 99% reflectivity as a reference. For each ore sample, the reflectance of each channel is calculated by averaging ten measurements, and the result is used as the final reflectance for classification. Figure 4.20 shows the spectral reflectance of all seven ore samples measured in the laboratory test, and it can be observed that different types of ore samples present unique spectral profiles. The calcite sample has considerably higher spectral reflectance values than the other ores. The olivine, quartz, and apatite samples have similar spectral profiles, especially between 400 and 800 nm. Additionally, the following classification operation is conducted based on their spectral profiles.

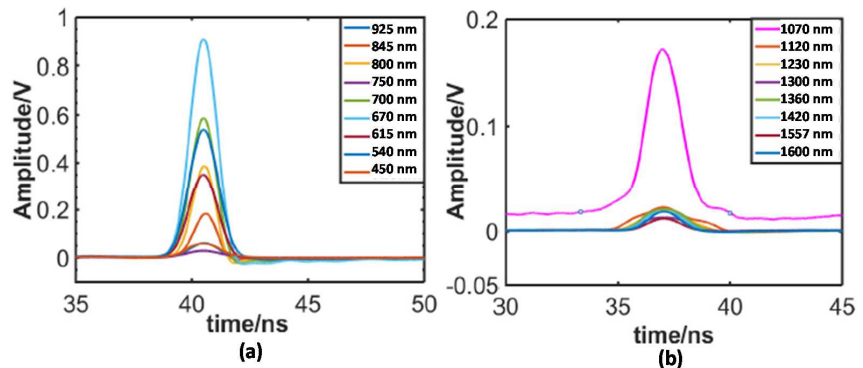


Figure 4.29 Spectral waveforms for calcite: (a) VNIR channels and (b) SWIR channels.

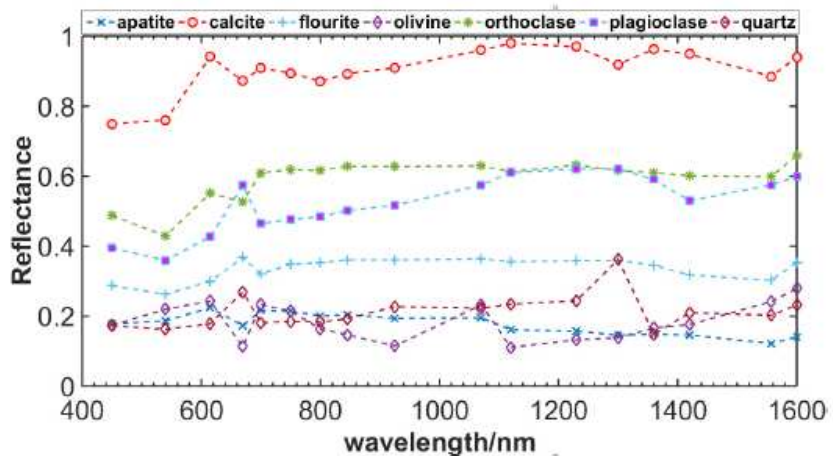


Figure 4.30. Reflectance measurements for the ore samples (average of ten measurements).

When all 17 hyperspectral reflectance values are used as the feature vector for classification operation, the standard multiple-SVM classifiers without parameter optimisation can output satisfactory results, and classification accuracy reaches 100% in our dataset. The results verify that using the spectral reflectance collected by the HSL system for ore classification is feasible, especially when sufficient spectral information is available. Furthermore, the results suggest that the standard multiple SVM can still perform well with fewer spectral

channels. Moreover, such an investigation can assist the design of practical HSL hardware. The use of fewer channels will simplify the HSL hardware design, reduce hardware costs, decrease the complexity of the signal processing method, and reduce the amount of storage space. Therefore, a criterion for channel selection operation or spectral feature selection is necessary for the optimised hardware system design. The standard multiple SVM is used for the ore classification. For the SVM, data with a better dispersion degree are easier to classify and separate (Cherkassky 1997; Lorena et al., 2008).

Thus, the FCD for classification can be created based on the distribution degree of the reflectance at each wavelength. In statistical learning theory, the variance can be regarded as the description of the degree of data dispersion. Therefore, the variances in the reflectance values for all the ore samples at all 17 wavelengths are calculated based on the reflectance measurements, and then the 17 FCD values can be defined by the normalised variance for the classification operation. We calculate the variance in the reflectance values using the average over ten measurements rather than single measurements to mitigate the effect of noise as described in the following equations:

$$FCD_i = \frac{var_i - var_{min}}{var_{max} - var_{min}} \quad (4.12)$$

$$var_i = \sqrt{\frac{\sum_{j=1}^7 (reflectance_{i,j} - reflectance_i)^2}{M}} \quad (4.13)$$

where

$$i = 1 \dots 17, j = 1 \dots 7, M = 7$$

Here,  $i$  is the channel number, and  $j$  denotes the ore sample number. (for each wavelength, there are seven reflectance measurements related to the ore samples).  $var_{min}$  and  $var_{max}$  are the minimum and maximum variances, respectively. Table 4.6 lists the calculated FCD values.

**Table 4.6.** FCD values of the 17 spectral channels

Wavelength /nm	FCD value	Wavelength /nm	FCD value
450	0.025	1070	0.43
540	0	1120	0.98
615	0.42	1230	0.88
670	0.35	1300	0.47
700	0.33	1360	1
750	0.28	1420	0.74
800	0.37	1557	0.48
845	0.46	1600	0.46
925	0.57		

Based on the sorted FCD values, the selected feature vectors in ascending and descending order are listed as follows:

① maxvector 5 = [9,11,12,14,15];

maxvector 6 = [9,11,12,14,15,16];

maxvector 7 = [9,11,12,13,14,15,16];

maxvector 8 = [8, 9,11,12,14,15,16, 17];

maxvector 9 = [8, 9,10,11,12,14,15,16, 17];

maxvector 10 = [3, 8, 9,10,11,12,14,15,16, 17];

maxvector 11 = [3, 7, 8, 9,10,11,12,14,15,16, 17];

② minvector 5 = [1,2, 4, 5, 6];

minvector 6 = [1, 2, 4, 5, 6, 7];

minvector 7 = [1, 2, 3, 4, 5, 6, 7];

minvector 8 = [1, 2, 3, 4, 5, 6, 7, 10];

minvector 9 = [1, 2, 3, 4, 5, 6, 7, 10, 17];

minvector 10 = [1, 2, 3, 4, 5, 6, 7, 8, 10, 17];

minvector 11 = [1, 2, 3, 4, 5, 6, 7, 8, 10, 13, 17];

To demonstrate the effectiveness of the FCD analysis and choose desirable spectral bands sensitive to ore sample classification, seven pairs of vectors (minvectors and maxvectors) are selected with a number of features from 5 to 11 but by different selection rules. When fewer than five features are used, the classification accuracy unexceptionally drops below 50% in the maxvector and minvector groups based on the default SVM parameters. However, it is difficult to obtain a satisfactory classification performance with fewer than five features by the standard multiple SVM. In contrast, when 11 features are used, the classification accuracy of the minvector and maxvector reaches 100%, and the two vectors inevitably share several common spectral features under this condition. Thus, pairs of feature vectors with a number of features varying from 5 to 11 are selected for comparison. The minvectors are in ascending order in which the features are selected based on the FCD from the minimum to the maximum. In contrast, the maxvectors are in descending order in which the features are selected with the FCD from the maximum to the minimum. Figure 4.31 shows the classification accuracy for the two groups of feature vectors.

The x-axis is the number of features, and the y-axis presents the classification accuracy. In the maxvector group, the classification accuracy increases from 60.42% to 100% when the number of features increases from 5 to 11. It is also noted that when the number of features is 7, the classification accuracy already approaches 100%. In the minvector group, the accuracy increases from 59.24% to 100% as the number of features increases from 5 to 11. Moreover, the maxvector group outperforms the minvector group when the same number of features is selected with different strategies. The results ensure the possibility of using the feature selecting criteria based on the FCD to optimise the system design. Besides, we find that the channels with higher FCD values are primarily centred

in the SWIR band. In particular, for the maxvectors, a 100% classification accuracy is obtained using seven selected channels out of all 17 spectral channels, and the seven selected feature channels are primarily in the SWIR band. This finding can be a reference for the optimisation design of the HSL system for similar ore classification applications. Additionally, the spectral range above 1.4  $\mu\text{m}$  is preferable due to eye-safety concerns for the HSL system.

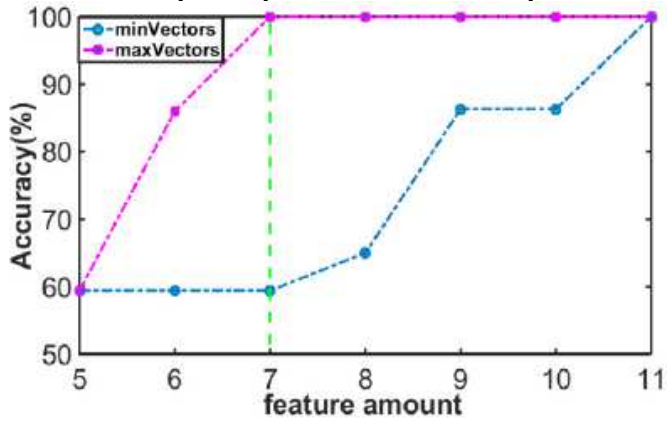


**Figure 4.31** Comparing the classification accuracy for different feature vectors selected according to the FCD

## 5. Discussion

The HSL instrument can use geometry and spectral information on the target from a single laser source without any registration inaccuracy. The system developed in Publication II also enables two-dimensional scanning with an effective range of more than 10 metres. Thus, single-tree-level classification was also carried out by Vauhkonen et al. (2013) to classify spruce and pine trees with laboratory measurements. Nevalainen et al. used the developed system to estimate the chlorophyll content at the leaf level, and the chlorophyll estimates derived from hyperspectral LiDAR linearly correlated with the laboratory-analysed chlorophyll concentrations ( $R^2 = 0.88$ ) (Nevalainen et al. 2014). An outdoor experiment was carried out with the system for detecting manufactured targets over 26 hours of measurements. The overall classification accuracy was 80.9% using the reflectances of four wavelengths located around the red edge (Puttonen et al. 2015). Kaasalainen et al. (2016) studied the effect of the incidence angle on the spectral content of leaf measurements from the developed system. They found that the backscatter signals did not follow the Lambert scattering law, especially in the visible bands, and other vegetation indices might change with the laser incidence angle to the target, which might be determined by the internal structure and surface properties of leaves.

Gaulton et al. (2013) investigated the potential of dual-wavelength laser scanning for estimating vegetation moisture content by determining the relationship between a laser-scanner-derived spectral index, using near-infrared (1063 nm) and middle-infrared (1545 nm) wavelengths and the equivalent water thickness of individual leaves. A strong relationship was found between a normalised ratio of the two wavelengths and measured the equivalent water thickness of leaf samples. Danson et al. (2014) developed a dual-wavelength full-waveform terrestrial laser scanner to characterise a forest canopy structure with near-infrared (1063 nm) and shortwave infrared (1545 nm) measurements using a separated laser source. Wang et al. (2014) studied the potential of using dual-wavelength airborne LiDAR (NIR and SWIR) to classify six types of suburban land cover classes: bare soil, low vegetation, high vegetation, roofs, water bodies, and road and gravel. Based on the major features of the dual-wavelength LiDAR data, the land cover was effectively classified, and the overall classification accuracy reached 97.4%. Morsy et al. (2017) explored the land cover classification of an urban area utilising a multi-spectral LiDAR system consisting of three Riegl LiDARs (532 nm, 1064 nm and 1550 nm), and the overall accuracies of up to 89.9% and 92.7% were achieved from image classification and 3D point classification, respectively.

Li et al. (2014) also designed a hyperspectral LiDAR system with a similar system configuration as Publication 1 to estimate the leaf biochemical content in a vegetation study; thus, the detecting wavelength was initially selected with some spectral bands that are sensitive to the vegetation reflectance, specifically 531, 570, 670 and 780 nm. Three vegetation indices – the simple ratio index, the NDVI and the photochemical reflectance index – were calculated using the reflectance derived from the data collected by the instrument. The significant difference was that it adopted optical fibre to relay the echo on the APD sensor rather than an installed sensor on the focal plane of the telescope. Gong et al. (2015) demonstrated the potential of using the spectral and spatial features derived from the novel MSLS with four wavelengths at 556, 670, 700, and 780 nm to discriminate 7 type of objects (walls, ceramic pots, Cactaceae plants, cartons, plastic foam blocks and healthy and dead *E. aureum* leaves) with an SVM classifier. The results showed that the overall classification accuracy was 88.7%, overwhelming the result derived from any standalone single-wavelength LiDAR system. Later, Chen et al. (2017) also proposed a two-step classification approach to eliminate noise during target classification based on the multi-spectral LiDAR system developed by Gong: a routine classification based on spectral information using the spectral reflectance or a vegetation index followed by neighbourhood spatial reclassification and improvement is promising. A 32-channel hyperspectral waveform LiDAR instrument prototype was designed by Sun et al. to monitor vegetation using a PMT array sensor, and the receiving echo was equally split into 32 bands from 409 to 914 nm by an optical grating system, resulting in a band interval of 17 nm (Sun et al. 2014). However, in addition to published initial performance trials, no further publications related to the new hardware can be found. Du et al. (2015) investigated the potential HSL system for vegetation that worked based on broad-spectrum emission and a 32-channel detector. These spectra collected by the HSL system were used to classify and derive the nitrogen contents of rice under four different nitrogen content levels with SVM regression. Manninen et al. (2014) demonstrated long-distance (1.5-km) active hyperspectral sensing using a high-power near-infrared SC light source without range information, and reflection spectra from several diffusive targets were successfully measured.

Based on studies carried out in the dissertation, with a more powerful laser source, Publication VI reveals that the potential of the effective range can reach approximately 40 metres with a standard reflection board target (20%) from 650 nm to 1000 nm which 10 nm spectral resolution, which is promising for mobile or terrestrial laser scanning applications. By merely adopting receiving optics with a larger aperture telescope, the effective range can be improved to more than one hundred metres which imply the possibility for a helicopter-borne system. Starting from two discrete bands in VNIR spectrum, the researches extend the HSL concept to 8, 17, 51 and even 91 bands with 5 nm spectral resolution in one latest published paper (Shao et al., 2019). The region of the electromagnetic spectrum is originally from VNIR to VNIR-SWIR in Publication III and IV, and the SWIR spectrum region measurements are meaningful for mining application, and the SWIR-enabled HSL is planned to be used for

snow monitoring in further researches. Meanwhile, by placing the spectroscopic device in transmitting optics, the transmitted laser energy can be considerably decreased to improve the usability of the HSL to more extensive applications, concerning the eye safety issue.

## 5.1 More outputs

I also investigated 51-channel AOTF-HSL system in vegetation parameter extraction. Green and yellow leaves from four different plants were employed in laboratory experiments for evaluating spectral profile acquisition and vegetation parameter extraction (Jiang et al., 2019). First, the first-order derivative of the spectral reflectance was employed to extract the “red-edge” position (REP), the “red-edge” slope (RES) and the “red-edge” area (REA) of these leaves, and the results were compared with the reference values from an SVC spectrometer for validation. Second, three different REP extraction methods, first-order reflectance slope (FRS), linear four-point interpolation technology (LFPIT) and linear extrapolation technology (LET), were employed for further evaluation using the AOTF-HSL spectral profile to determine the REP value. Overall, the comparison among the REP results from the three methods supported that the AOTF-HSL system was effective in this application.

We found that the spectral slope curves of the green leaves of all the selected plants extracted from AOTF-HSL system coincide with the corresponding referenced measurements from the SVC spectrometer. Table 5.2, Table 5.3 and Table 5.4 list the quantitative results of the vegetation parameter results and their differences; the percentages are calculated using the difference HSL-derived values divided by the corresponding referenced results from the SVC spectrometer. The differences in the REPs of all green leaf test cases are below 1%; however, for the REP slope, only the difference percentage for the green aloe leaf REP slope is below 1%. Specifically, the REP slope of the green dracaena leaf is higher than 10%. For the green leaf REA results, the green dracaena leaf difference is also the largest, and it is greater than 5%.

However, the yellow leaf curves from the AOTF-HSL measurements are distinctive from those of the SVC spectrometer. Further analysis is also given in Table 5.1, Table 5.2 and Table 5.3. The REP differences of the yellow leaf cases are 9.45 nm and 24.1 nm, respectively, and the corresponding differences are considerably higher than those of the green leaf cases. Moreover, for the REP slope and REA, the results are quite distinctive, with a difference of more than 30%. We think that these following reasons might account for this phenomenon.

- (1) Green leaves have more uniformed spectral reflectivity since the contents affecting the relative “red-edge” parameters are evenly distributed on them; in contrast, yellow leaves have uneven distributions of the contents, and the reflectivity is different for different “yellow” parts of the leaf;
- (2) The hardware design, optic system, and measurement distance determine the diameter of the laser pulse footprint, which is approximately 1 cm in this experiment with a FOV of 0.2 mrad. The sampled area of the spectrometer is considerably larger (resulting in a 5.5-cm radius footprint with a 25° field of

view). The laser-footprint-covered area has a different reflectivity due to the non-uniformity of the yellow leaves.

**Table 2.** “Red-edge” position results based on the FRS technique

	REP (nm)		
	AOTF-HSL	SVC	Difference
Green Dracaena Leaf	725	718.85	6.15 (0.85%)
Yellow Dracaena Leaf	695	685.55	9.45 (1.3%)
Green Aloe Leaf	725	718.85	6.15 (0.85%)
Yellow Aloe Leaf	715	690.9	24.1 (3.4%)
Green Rubber Plant Leaf	725	725.45	0.45 (0.06%)
Green <i>Radermachera</i> Leaf	715	718.85	3.85 (0.53%)

**Table 32.** “Red-edge” slope results

	REP slope		
	AOTF-HSL	SVC	Difference
Green Dracaena Leaf	0.95	1.07	0.12 (11.2%)
Yellow Dracaena Leaf	1.44	1.03	0.41 (39.8%)
Green Aloe Leaf	1.29	1.3	0.01 (0.08%)
Yellow Aloe Leaf	1.1	0.59	0.51 (86%)
Green Rubber Plant Leaf	1.09	1.17	0.08 (6.8%)
Green <i>Radermachera</i> Leaf	1	1.07	0.07 (6.5%)

**Table 43.** “Red-edge” area results

	REA		
	AOTF-HSL	SVC	Difference
Green Dracaena Leaf	47.94	51.36	3.42 (6.7%)
Yellow Dracaena Leaf	36.67	26.34	10.33 (39.2%)
Green Aloe Leaf	52.54	51.1	1.43 (2.8%)
Yellow Aloe Leaf	41.63	31.53	10.1 (32.0%)
Green Rubber Plant Leaf	44	43.68	0.32 (0.7%)
Green <i>Radermachera</i> Leaf	43.39	42.01	1.38 (3.2%)

Also, by comparing the REP between green and yellow leaves from the same plant, it can be discerned that the REP has a distinct shift towards a shorter wavelength called a “blueshift”. The yellow leaves have a lower chlorophyll content than the green leaves, and this tendency or REP behaviour is consistent and identical to previous research results (Pu et al. 2003; Li et al. 2018; Chen et al. 2019).

We also compared the REP results from different calculation methods, and the REP was determined using the FRS technique. There are other methodologies for interpolating the reflectance REP, such as linear four-point interpolation technology (LFPIT) (Shafri and Hamdan. 2009) and linear extrapolation technology (LET) (Liu et al. 2011). To further validate and evaluate the proposed active remote sensing method, the AOTF-HSL spectral information is employed to calculate the REP based on LFPIT and LET. The following are the details of the two popular REP determination methods.

- (1) First, the LFPIT technique is described in Eqs. 5.1-5.2. In this experiment, the method employs four wavelengths for calculating the REP. As illustrated, the 670 nm and 780 nm spectral information is used to calculate the reflectance at the REP, and the 700 nm and 740 nm spectral data are used to determine the REP. In Eq. 5.1-5.2,  $R_{670}$  and  $R_{780}$  are the corresponding reflectance values at 670 nm, and 780 nm, respectively.  $R_{700}$  and  $R_{740}$  are the corresponding reflectance values at 700 nm and 740 nm, respectively.

$$R_{REP} = \frac{(R_{670} + R_{780})}{2} \quad (5.1)$$

$$\lambda_{REP} = 700 + 40 \frac{(R_{REP} - R_{700})}{R_{740} - R_{700}} \quad (5.2)$$

- (2) Second, the LET method can be presented as Eqs. 5.3-5.5, and the REP is determined using the two extrapolation equations. Eq. 5.3 is the extrapolation of the reflectance for spectral ranges of 680 nm and 700 nm. Eq. 5.4 is the extrapolation of the reflectance for spectral ranges of 725 nm and 760 nm. Then, the REP is determined using the parameter from Eqs. 5.3-5.4. In the following equations,  $FDR_1$  and  $FDR_2$  are the spectral reflectance slopes of the spectra ranging from 680 nm to 700 nm ( $FDR_1$ ) and from 725 nm to 760 nm ( $FDR_2$ ).  $m_1$ ,  $m_2$ ,  $c_1$  and  $c_2$  are the parameters for describing the spectral reflectance slope and determining the REP. Eq. 5.5 calculates the REP.

$$FDR_1 = m_1 \lambda + c_1 \quad (5.3)$$

$$FDR_2 = m_2 \lambda + c_2 \quad (5.4)$$

$$\lambda_{REP} = \frac{-(c_1 - c_2)}{m_1 - m_2} \quad (5.5)$$

The selected wavelength spectral reflectance from LFPIT and LET is within the wavelength scope of the AOTF-HSL system. Thus, in this section, the spectral profiles collected by the AOTF-HSL system are utilised for parameter extraction. Tables 5.4-5.9 are the results of the three REP determination methods. Among them, Tables 5.4, 5.6, 5.8 and 5.9 are the REP results from the green leaf study cases, and Tables 5.5 and 5.7 are the REP results from yellow leaves of the dracaena and aloe plants.

First, in terms of the green leaf results, the AOTF-HSL system and the SVC spectrometer yield similar REPs using the four different results, and the difference is trivial and well below 1%, except for the REP of the rubber plant extracted from the LFPIT method. The lower spectral resolution of the AOTF-HSL system (10 nm) may account for such a difference from the SVC measurement, which has a more exceptional spectral resolution (2 nm).

Second, in terms of the yellow leaves (Table 5.6 and Table 5.8), the difference in the results from the LFPIT and LET methods between the AOTF-HSL system and the SVC spectrometer is all greater than 5%, which is slightly higher than the REP results from the FRS method. Compared with the green leaves, the difference between the AOTF-HSL system and SVC spectrometer is more substantial in all the yellow leaf study cases. Besides, the three methods yield similar REP results in the green leaves, including the AOTF-HSL system and SVC spectrometer; however, there is a noticeable difference in the yellow leaf results. In particular, for the AOTF-HSL REP of the yellow dracaena leaf case, the LFPIT and LET methods yield similar results, but they are different from the FRS results. As mentioned above, the spectral resolution influences the operation of the LET and LFPIT methods, and in this experiment, the spectral resolution of

the AOTF-HSL system is set to 10 nm, which might affect the calculation of the results.

**Table 54.** “Red-edge” position results for the green dracaena leaves from the three different methods

	REP (nm)		
	AOTF-HSL	SVC	Difference
LFPIT	717.80	722.32	4.52 (0.63%)
LET	709.42	712.24	2.82 (0.40%)
FRS	725	718.85	6.15 (0.85%)

**Table 65.** “Red-edge” position results for yellow dracaena leaves from the three different methods

	REP		
	AOTF-HSL	SVC	Difference
LFPIT	636.79	692.43	55.64 (8.7%)
LET	628.65	679.91	51.26 (8.2%)
FRS	695	685.55	9.45 (1.3%)

**Table 76.** “Red-edge” position results for green aloe leaves from the three different methods

	REP		
	AOTF-HSL	SVC	Difference
LFPIT	718.68	715.13	-3.55 (0.49%)
LET	720.32	719.95	-0.37 (0.05%)
FRS	725	718.85	6.15 (0.85%)

**Table 87.** “Red-edge” position results for yellow aloe leaves from the three different methods

	REP		
	AOTF-HSL	SVC	Difference
LFPIT	715.61	674.27	-41.34 (5.8%)
LET	721.12	669.01	-52.11 (7.2%)
FRS	715	690.9	24.1 (3.4%)

**Table 98.** “Red-edge” position results for the rubber plant from the three different methods

	REP		
	AOTF-HSL	SVC	Difference
LFPIT	712.63	748.79	36.16 (5.1%)
LET	722.60	726.10	3.5 (0.5%)
FRS	725	725.45	0.45 (0.06%)

**Table 109.** “Red-edge” position results for the green Radermachera leaves from the three different methods

	REP		
	AOTF-HSL	SVC	Difference
LFPIT	712.14	709.25	-2.89 (0.4%)
LET	717.91	718.67	0.76 (0.1%)
FRS	715	718.85	3.85 (0.53%)

## 5.2 The Goal of the Dissertation

From the contents mentioned above, a solid conclusion can be made that the basic hypotheses and primary objectives of this dissertation have been accomplished. Determination of the spectral response of a target is possible with the proposed hyperspectral LiDAR techniques with high accurate range measurement. By collecting geometry and spectral information on the target with a single measurement, the HSL technology is also immune to illumination condition. The acquired spectral response can be compared with passive remote sensing approaches, and the average spectral differences (absolute value) of green leaf (four) and yellow leaf (two) for the HSL and spectrometer measurements are 1.09% and 6.70%, respectively. With the different parameters extracted from the collected waveforms, the feasibility studies in forestry, plant and mining with the proposed HSL techniques shows that the spectral response acquired by HSL-based approaches can be used to objects discrimination and classification. The results based on laboratory is promising, for example, a multiclass SVM classifier without parameter optimisation allows ore classification accuracies to reach 100% (seven different ores) with reflectance measurements from maximum 11 bands. The primary objectives of the research, conducted during 2010-2018, develop six different hyperspectral LiDAR system to tackle environmental awareness using an SCL as a light source and to evaluate the feasibility of the developed method in its application in forestry, plant science and mining.

The concept of HSL provides a novel approach for spectral imaging and laser scanning by producing single-shot topography and spectroscopy. The instrument is capable of producing hyperspectral 3D point clouds both with discrete and continuous spectral coverage from the VNIR to SWIR spectral range with the best spectral resolution equal to 5 nm. The author investigated HSL systems based on various system configurations with different spectroscopic devices in his previous and undergoing research. In addition to the spatial information collected by HSL as a function of traditional LiDAR, spectral information can be used in various environmental awareness applications, e.g., visualisation and automated classification of point clouds and the calculation of spectral indices for extraction of physical properties. The information provided by such an innovative instrument is considerable and will facilitate more efficient and automatic retrieval of distinctive target properties, leading to considerable progress in environmental-monitoring technology for various context-awareness applications.

Both the general range precision and accuracy of the spectral measurement from HSL systems were evaluated, with a similar ToF measurement mechanism based on full-waveform capability. The range precision is comparable to traditional LiDAR systems, even though the range calibration of HSL is more complicated over the full spectral channels. The spectral profiles measured by spectrometers were used as a reference for evaluating the spectral measurements of the HSL systems. The difference between the spectral measurements collected from active and passive instruments was minor, especially after calibration.

Several feasibility studies using the prototype HLS systems for environmental awareness were evaluated in forestry inventory, plant science and ore classification tasks. The collected spectral profiles were compared with the spectrometer-based passive method. Some spectral band selection criteria are preliminarily investigated to optimise the system design with lower costs and system complexity. Such an investigation may accelerate its maturity, and we can anticipate that some commercial manufacturers may release their HSL products soon.

It is of considerable significance to obtain spectral information for developing an active measuring method. The AOTF-HSL system presented in this disserta-

tion has the unique characteristics of a continuous spectrum in the VNIR regions with a 10-nm spectral resolution and further improve to 5 nm (Shao et al., 2019), which is the best spectral resolution in the literature. However, limited by the HSL hardware configuration and the data-processing capacity, compared with the SVC spectrometer, the spectral resolution was still slightly limited. We think that this is the primary reason contributing to the slight differences between the AOTF-HSL and spectrometer measurements of the same targets.

### 5.3 Future Research

Future research on hyperspectral LiDAR for environmental awareness will focus on the following four aspects:

1. Extending the spectrum of the HSL system, the developed HSL covered the spectrum from 500 nm-1700 nm. However, the MIR and LWIR spectra are still not available if a breakthrough in sensor technology does not happen, and from 1000-1700 nm, only discrete spectral channel configurations are available. Nevertheless, integration of the HSL with novel photodetector technique based 2D material is still a promising direction.
2. The maximum range is still limited for further application. In the laboratory test, the targets with reflectivity from 20% to 100% placed at a range of 37.5 metres can be detected with high signal-to-noise ratio waveforms. The results are promising, which reveals that it may be possible to observe brighter ground objects on a helicopter platform with an operating altitude of several tens to one hundred metres with minor modification on the current system configuration. Of course, a larger aperture of receiving optics, more powerful laser sources, and more sensitive receiving electronics can improve the maximum range performance of HSL systems. Among them, improving the receiving electronics design is the most effective and cost-saving method.
3. Improving the mobility of the developed HSL is another critical issue for the field test. Currently, all feasibility studies were carried out in a laboratory environment. Better mobility will trigger a revolution in the remote sensing community by enabling various applications with hyperspectral mobile laser scanning and hyperspectral terrestrial laser scanning techniques. Malkamäki et al. (2019) recently implemented a new robust design of HSL for portable applications together with an improved pulse-digitising scheme. As mentioned in Section 4, the SNR of the AOTF-HSL system is promising. Such observations support the upgrading of the current AOTF-HSL prototype by integrating a georeferenced system and altitude measurement devices into a mobile/helicopter-borne version with an effective range of more than a hundred metres covering continuous spectrum VNIR and with a spectral resolution of more than 10 nm. With such a mobile instrument, the 3D distribution of the chlorophyll or water concentration indices and other vegetation indices along with the vertical structure of forest and vegetation at the plot level, even at the plot level, can be easily monitored and thus, the environmental contexts related to fertilisation, pest control situation, and hydrologic conditions can be detected. Designing a compact HSL will improve its applicability for various environmental awareness applications even with a shorter effective range, and it can decrease the budgets of power consumption, volume and hardware investments in addition to better eye safety. For example, HSL based on a miniature integrated optical filter array (Wang et al., 2007) can considerably simplify the system design for close-range applications, for example, tunnel and underground mining modelling and understanding and indoor/outdoor seamless environmental awareness for robotics by replacing the traditional range sensors, for example, sonars, radars or monochromatic LiDARs.

4. Eye safety is an exceptional but unavoidable issue in laser remote sensing for practical operations. For HSL, the eye-safety issue becomes more critical; the spectroscopic device can be installed both on the transmitting optics and receiving optics, and the former is a better option for eye-safety considerations. Besides, spectral multiplexing in the temporal dimension is an alternative solution.

All future works will improve the applicability of the system by assessing the range accuracy through the whole spectrum with a more sophisticated range calibration method by considering various extrinsic and intrinsic parameters. Radiometric calibration should be designed to facilitate practical field testing generally. Currently, all test cases are carried out in a laboratory environment where all artificial light sources are turned off during the test and sunlight is totally blocked, and the reference targets are positioned at fixed ranges.



## 6. Summary

The objective of this dissertation considers new sensor technology related to hyperspectral LiDAR and its feasibility for various applications in forestry, plant science and mining applications. The study investigates 1) various spectroscopic devices and 2) different photodetectors to build HSLs that offer discrete and consecutive spectral responses of targets from the VNIR to SWIR bands simultaneously with range information. The main results of the dissertation are summarised in the following

1 Hyperspectral LiDAR system development based on supercontinuum laser source.

Total six different hyperspectral LiDARs were prototyped during the research period (2010-2018) using different techniques, with optimised channel selection and spectral coverage for specific applications in forestry, plant and mining.

- By using band-pass optical filters, a two-channel LiDAR system is demonstrated, operating at visual (600 nm) and near-infrared (800 nm) band, with 3 cm range resolution, and the demos are for forestry application.

- An eight-channel spectrograph-based hyperspectral LiDAR enabling full-waveform capability is designed and demonstrated, operating at spectrum region of visual to near-infrared (540 – 981 nm) with 15 cm range resolution; and the channel selection is optimised for vegetation application to detect the “red-edge” (672, 707, 740, 775 nm)

- An optical filter based hyperspectral LiDAR with eight channels covering from visual to short wave infrared (540 to 1460 nm) with 3 cm range resolution is developed and tested at close range (< 10 metres).

- The author designs optical filters based 17 channels hyperspectral LiDAR covering visual to near-infrared (nine channels: 450 – 925 nm) to short wave infrared (eight channels: 1070 – 1600nm) with 3 cm range resolution for close-range sensing. An extra amplifier is used to compensate for the lower sensitivity of the InGaAs avalanche photodiode for short wave infrared signal detection. The channel selection is optimised for mining application.

- A consecutive and 18 channels (550-720 nm) 10 nm spectral resolution hyperspectral LiDAR is prototyped, using liquid crystal tunable filter as the spectroscopic device, and the channel configuration is optimised for “red-edge” detection for vegetation application.

- A consecutive and 51 channels (500-1000 nm) finer spectral resolution (10 nm) hyperspectral LiDAR is prototyped, using acousto-optic tunable filters as the spectroscopic device which is installed on the supercontinuum laser source as a spectral filter to mitigate the transmitted laser energy for better eye-safety.

## 2. Hyperspectral LiDAR for forestry inventory

- The results show that the HSL system, even with two discrete spectral channels, can offer meaningful parameters to discriminate Norway spruce from standard reflection board based on the determination of the normalised difference vegetation index.
- The range resolution of the HSL system is determined by the sampling rate of the selected digitiser and the random quantisation error in the raw measurements of the waveform of both the transmitting pulse and echo collected by the high-speed digitiser, which may cause inaccurate range measurements.
- The signal to noise ratio of the echoes on the different spectral channels varies considerably, which is caused by a combined effect of several factors, the variance in the laser output in the transmitting wavelengths and the spectral response of the avalanche photodiode sensor in the receiving part, which may restrict the maximum range performance of the hyperspectral LiDAR system over the board bandwidth.
- With the hyperspectral LiDAR system with eight discrete spectral channels, more vegetation indices can be obtained from the measured dataset compared with the 2-channel system. Besides, the normalised difference vegetation index, the water concentration index, and the modified chlorophyll absorption ratio index are extracted from the measured dataset.

## 3. Hyperspectral LiDAR in plant science

- An eight-channel hyperspectral LiDAR system covering the visual to short wave infrared bands is preliminarily used to investigate three *Scindapsus* plants (two healthy *Scindapsus* plants grown in soil and water and one dry and withered *Scindapsus* plant). The unhealthy *Scindapsus* plant can be detected from the spectra collected by the hyperspectral LiDAR system, and the difference between the two healthy *Scindapsus* plants can also be observed.
- The hyperspectral LiDAR measurements mainly coincide with the referenced spectrometer measurements. The difference between three *Scindapsus* plants in the short wave infrared band is more obvious to be observed.
- A hyperspectral LiDAR system based on a liquid crystal tunable filter offers continuous and finer spectral resolution (10 nm spectral resolution), and liquid crystal tunable filter is installed before the photodiode sensor and employed as a spectroscopic device capable of electronically and continuously selecting the wavelengths of the backscattered echoes in the temporal dimension. The liquid crystal tunable filter based hyperspectral LiDAR system is feasible for red-edge detection.
- The validation of the reflectance values shows that the magnitude of the reflectance from the liquid crystal tunable filter based hyperspectral LiDAR system is slightly higher than the normalised value collected by the spectrometer, and the tendency is more evident in the red-band spectrum.
- The red-edge position and behaviour extracted from both the spectrometer and the liquid crystal tunable filter based hyperspectral LiDAR system are similar in

two case studies, in which two types of vegetation (aloe and dracaena plants), both with yellow and green leaves, are measured.

- After careful calibration, the average spectral differences (absolute values) between the AOTF-HSL and spectrometer measurements are minimal, especially in the green leaf study cases, and the differences are 1.37% (dracaena plant), 0.84% (aloe plant), 1.36% (rubber plant), and 0.77% (Radermachera plant). For the yellow leaf study cases, the average spectral differences are more substantial than those for the green leaf cases, but still promising, specifically, 8.79% for the dracaena plant and 4.6% for the aloe plant.

#### 4. Hyperspectral LiDAR in mining

- The hyperspectral LiDAR system consists of 17 spectral channels covering the visible–shortwave infrared spectral range and can classify seven ore samples supported by a standard support vector machine classifier.

- The standard deviation of the distance measurements is less than 1.1 cm in different spectral channels for a calcite sample, and the classification accuracy can reach 100% for laboratory test cases with multiple standard support vector machine classifiers when all 17 spectral measurements are used.

- A feature selection criterion is investigated using the normalised variance in the reflectance values for different ore samples at the same wavelength to potentially optimise the practical HSL hardware design. The results show that a proper strategy for feature selection is also critical for achieving better classification accuracy.

- The author finds that the selected channels by optimisation are primarily centred in the short wave infrared band, which might imply that the short wave infrared band is preferable for the ore classification application. The spectral range above 1.4  $\mu\text{m}$  is preferable due to eye-safety concerns.

- Proper data pre-processing, such as Gaussian fitting, can improve both the range accuracy and classification accuracy.



# References

1. Abellán, A., Oppikofer, T., Jaboyedoff, M., Rosser, N. J., Lim, M., & Lato, M. J. (2014). Terrestrial laser scanning of rock slope instabilities. *Earth surface processes and landforms*, 39(1), 80-97.
2. Ackerman, J., Dietrich, G., & Ruddock, K. (1967). An airborne laser terrain profiling system. *IEEE Journal of Quantum Electronics*, 3(6), 233-233.
3. Ahokas E, Hyypä J, Yu X, Liang X, Matikainen L, Karila K, Litkey P, Kukko A, Jaakkola A, Kaartinen H, Holopainen M. TOWARDS AUTOMATIC SINGLE-SENSOR MAPPING BY MULTISPECTRAL AIRBORNE LASER SCANNING. *International Archives of the Photogrammetry, Remote Sensing & Spatial Information Sciences*. 2016 Jul 14:41.
4. Ahokas, E., Kaasalainen, S., Hyypä, J. and Suomalainen, J., 2006. Calibration of the Optech ALTM 3100 laser scanner intensity data using brightness targets. *International Archives of Photogrammetry, Remote Sensing and Spatial Information Sciences*, 36(Part 1), p.1Á6.
5. Aldred, A. H., & Bonnor, G. M. (1985). Application of airborne lasers to forest surveys (Vol. 51).
6. Alonzo, M., Bookhagen, B. and Roberts, D.A., 2014. Urban tree species mapping using hyperspectral and LiDAR data fusion. *Remote Sensing of Environment*, 148, pp.70-83.
7. Amzajerjian, F., Pierrotet, D., Petway, L., Hines, G., & Roback, V. (2011, August). LiDAR systems for precision navigation and safe landing on planetary bodies. In *International Symposium on Photoelectronic Detection and Imaging 2011: Laser Sensing and Imaging; and Biological and Medical Applications of Photonics Sensing and Imaging* (Vol. 8192, p. 819202). International Society for Optics and Photonics.
8. Asrar G, Fuch M, Kanemasu ET, et al. (1984) Estimating absorbed photosynthetic radiation and leaf area index from spectral reflectance in wheat. *Agron J* 76:300-6.
9. Axelsson, A., Lindberg, E. and Olsson, H., 2018. Exploring multispectral ALS data for tree species classification. *Remote Sensing*, 10(2), p.183.
10. Bauer, S. and León, F.P., 2015. Spectral and geometric aspects of mineral identification by means of hyperspectral fluorescence imaging. *Tm-Technisches Messen*, 82(12), pp.597-605.
11. Bork, E. W., & Su, J. G. (2007). Integrating LIDAR data and multispectral imagery for enhanced classification of rangeland vegetation: A meta analysis. *Remote Sensing of Environment*, 111(1), 11-24.
12. Bradbury, Richard B., et al. "Modelling relationships between birds and vegetation structure using airborne LiDAR data: a review with case studies from agricultural and woodland environments." *Ibis* 147.3 (2005): 443-452.
13. Brandtberg, T., Warner, T. A., Landenberger, R. E., & McGraw, J. B. (2003). Detection and analysis of individual leaf-off tree crowns in small footprint, high sampling density LiDAR data from the eastern deciduous forest in North America. *Remote sensing of Environment*, 85(3), 290-303.
14. Briese, C., Pfennigbauer, M., Lehner, H., Ullrich, A., Wagner, W. and Pfeifer, N., 2012. Radiometric calibration of multi-wavelength airborne laser scanning data. *ISPRS Ann. Photogramm. Remote Sens. Spat. Inf. Sci*, 1, pp.335-340.
15. Buchter, S.C., Kaivola, M., Ludvigsen, H. and Hansen, K.P., 2004, May. Miniature supercontinuum laser sources. In *Conference on Lasers and Electro-Optics* (p. CTuP58). Optical Society of America.
16. Buchter S C, Ludvigsen H E, Kaivola M. Method of generating supercontinuum optical radiation, supercontinuum optical radiation source, and use thereof: U.S. Patent 8,000,574[P]. 2011-8-16.

17. Buckley, S.J., Kurz, T.H., Howell, J.A. and Schneider, D., 2013. Terrestrial LiDAR and hyperspectral data fusion products for geological outcrop analysis. *Computers & Geosciences*, 54, pp.249-258.
18. Budei, B. C., St-Onge, B., Hopkinson, C., & Audet, F. A. (2018). Identifying the genus or species of individual trees using a three-wavelength airborne LiDAR system. *Remote Sensing of Environment*, 204, 632-647.
19. Cabral AIR, Martins E, Bartholome' E', et al. (2006) A land cover map of southern hemisphere Africa based on SPOT-4 vegetation data. *Int J Remote Sens* 27:1053–74.
20. Cheng, A. F., Cole, T. D., Zuber, M. T., Smith, D. E., Guo, Y., & Davidson, F. (2000). In-flight calibration of the near earth asteroid rendezvous laser rangefinder. *Icarus*, 148(2), 572-586.
21. Chen X, Chengming YE, Li J, Chapman MA. Quantifying the carbon storage in urban trees using multispectral ALS data. *IEEE Journal of Selected Topics in Applied Earth Observations and Remote Sensing*. 2018 Aug 10;11(9):3358-65.
22. Chen, Y., Li, W., Hyypää, J., Wang, N., Jiang, C., Meng, F., Tang, L., Puttonen, E. and Li, C., 2019. A 10-nm spectral resolution hyperspectral LiDAR system based on an acousto-optic tunable filter. *Sensors*, 19(7), p.1620.
23. Chen, Y., Jiang, C., Hyypää, J., Qiu, S., Wang, Z., Tian, M., ... & Bo, Y. (2018). Feasibility Study of Ore Classification Using Active Hyperspectral LiDAR. *IEEE Geoscience and Remote Sensing Letters*, (99), 1-5.
24. Chen, Y., Räikkönen, E., Kaasalainen, S., Suomalainen, J., Hakala, T., Hyypää, J., & Chen, R. (2010). Two-channel hyperspectral LiDAR with a supercontinuum laser source. *Sensors*, 10(7), 7057-7066.
25. Chen, Y., Tang, J., Feng, Z., Hakala, T., Hyypää, J., Zhou, C., ... & Li, C. (2017). Possibility of applying SLAM-aided LiDAR in deep space exploration. In *3rd International Symposium of Space Optical Instruments and Applications* (pp. 239-248). Springer, Cham.
26. Chen, Y., Tang, J., Hyypää, J., Wen, Z., Li, C., & Zhu, T. (2016, November). Mobile laser scanning based 3D technology for mineral environment modeling and positioning. In *2016 Fourth International Conference on Ubiquitous Positioning, Indoor Navigation and Location Based Services (UPINLBS)* (pp. 289-294). IEEE.
27. Chen Y. W.; Zhang, L.; Hu, Y. H. Zhang, H. M.; Shu, R.; Wang, J.Y. "Array Detection Technology of Echo on Earth Observation Laser Imager." *Journal of Infrared and Millimeter Waves*, 2004, 23 (3), 169-175
28. Cho, M. A., & Skidmore, A. K. (2006). A new technique for extracting the red edge position from hyperspectral data: The linear extrapolation method. *Remote sensing of environment*, 101(2), 181-193.
29. Cherkassky, V. (1997). The nature of statistical learning theory~. *IEEE Transactions on Neural Networks*, 8(6), 1564-1564.
30. Clark ML, Roberts DA, Ewel JJ, Clark DB. Estimation of tropical rain forest aboveground biomass with small-footprint LiDAR and hyperspectral sensors. *Remote Sensing of Environment*. 2011 Nov 15;115(11):2931-42.
31. Collins, W., 1978, Remote sensing of crop type and maturity. *Photogrammetric Engineering and Remote Sensing*, 44, 43±55
32. Dalponte, M., Bruzzone, L. and Gianelle, D., 2008. Fusion of hyperspectral and LIDAR remote sensing data for classification of complex forest areas. *IEEE Transactions on Geoscience and Remote Sensing*, 46(5), pp.1416-1427.
33. Dalponte, M., Bruzzone, L. and Gianelle, D., 2012. Tree species classification in the Southern Alps based on the fusion of very high geometrical resolution multispectral/hyperspectral images and LiDAR data. *Remote sensing of environment*, 123, pp.258-270.
34. Danson, F. M., Gaulton, R., Armitage, R. P., Disney, M. I., Gunawan, O., Lewis, P. E., Ramirez, A. F. (2014). Developing a dual-wavelength full-waveform terrestrial laser scanner to characterize forest canopy structure. *Agricultural and Forest Meteorology*, 198-199, 7-14.
35. Darvishzadeh R, Atzberger C, Skidmore A K, et al. "Leaf Area Index derivation from hyperspectral vegetation indices and the red edge position." *International Journal of Remote Sensing*, vol.30, no.23, pp. 6199-6218, Dec. 2009.

36. Dawson, T. P., and P. J. Curran. "Technical note A new technique for interpolating the reflectance red edge position." (1998): 2133-2139.
37. Dillon, R. F., & Parker Jr, J. F. (1969). A survey of possible hazards to vision from lasers in aerospace operations.
38. Donoghue, D. N., Watt, P. J., Cox, N. J., & Wilson, J. (2007). Remote sensing of species mixtures in conifer plantations using LiDAR height and intensity data. *Remote Sensing of Environment*, 110(4), 509-522.
39. Douglas, E. S., Martel, J., Li, Z., Howe, G. A., Hewawasam, K., Marshall, R. A., ... Chakrabarti, S. (2015). Finding leaves in the forest: the Dual-Wavelength Echidna LiDAR. *Geoscience and Remote Sensing Letters, IEEE*, 12(4), 776-780.
40. Dudley, M.J.; Genty, G.; Coen, S. Supercontinuum generation in photonic crystal fiber. *Rev. Modern Phys.* 2006, 78, 1135-1184.
41. Du, L., Gong, W., Shi, S., Yang, J., Sun, J., & Zhu, B., et al. (2016). Estimation of rice leaf nitrogen contents based on hyperspectral LiDAR. *International Journal of Applied Earth Observation & Geoinformation*, 44, 136-143.
42. Du S., Li X., Liu Z. Chen Y., Wang Z., Tang L., He W. Radiometric Characteristics of the Intensity data of Laser Scanner, *Journal of University of Chinese Academy of Science*, Vol.36, No.3, pp415-423, 2019
43. Eitel, J. U. H., Magney, T. S., Vierling, L. A., & Dittmar, G. (2014). Assessment of crop foliar nitrogen using a novel dual-wavelength laser system and implications for conducting laser-based plant physiology. *ISPRS Journal of Photogrammetry and Remote Sensing*, 97(0), 229-240.
44. Elachi, C., & Van Zyl, J. J. (2006). Introduction to the physics and techniques of remote sensing (Vol. 28). John Wiley & Sons.
45. Erdody, T.L.; Moskal, L.M. Fusion of LiDAR and imagery for estimating forest canopy fuels. *Remote Sens. Environ.* 2010, 114, 725-737.
46. Fernandez-Diaz J, Carter W, Glennie C, Shrestha R, Pan Z, Ekhtari N, Singhania A, Hauser D, Sartori M. Capability assessment and performance metrics for the Titan multispectral mapping LiDAR. *Remote Sensing*. 2016 Nov 10;8(11):936.
47. Fredriksson, K., Galle, B., Nyström, K., & Svanberg, S. (1981). Mobile LiDAR system for environmental probing. *Applied Optics*, 20(24), 4181-4189.
48. Galio KP, Daughtry CST, Bauer ME (1985) Spectral estimation of absorbed photosynthetically active radiation in corn canopies. *Agron J* 78:752-6.
49. Galvao, L.S., Formaggio, A.R. and Tisot, D.A., 2005. Discrimination of sugarcane varieties in Southeastern Brazil with EO-1 Hyperion data. *Remote sensing of Environment*, 94(4), pp.523-534.
50. Gat N. Imaging spectroscopy using tunable filters: a review[C]//Wavelet Applications VII. International Society for Optics and Photonics, 2000, 4056: 50-65.
51. Gaulton R, Danson F M, Ramirez F A, et al. The potential of dual-wavelength laser scanning for estimating vegetation moisture content[J]. *Remote Sensing of Environment*, 2013, 132: 32-39.
52. Geerling, G. W., Labrador-Garcia, M., Clevers, J. G. P. W., Ragas, A. M. J. & Smits, A. J. M. (2007). Classification of floodplain vegetation by data fusion of spectral (CASI) and LiDAR data. *International Journal of Remote Sensing*, 28(19), 4263-4284.
53. Genç, L., Dewitt, B., & Smith, S. (2004). Determination of wetland vegetation height with LIDAR. *Turkish Journal of agriculture and forestry*, 28(1), 63-71.
54. Glenn, E.P.; Huete, A.R.; Nagler, P.L.; Nelson, S.G. Relationship between remotely-sensed vegetation indices, canopy attributes and plant physiological processes: What vegetation indices can and cannot tell us about the landscape. *Sensors*, 2008, 8, 2136-2160.
55. Gong, W.; Song, S. L.; Zhu, B.; Shi, S.; Li, F. Q.; Cheng, X.W. "Multi-wavelength canopy LiDAR for remote sensing of vegetation: Design and system performance." *ISPRS Journal of Photogrammetry and Remote Sensing*, 2012, 69, 1-9.
56. Gong, W., Sun, J., Shi, S., Yang, J., Du, L., Zhu, B. and Song, S., 2015. Investigating the potential of using the spatial and spectral information of multispectral LiDAR for object classification. *Sensors*, 15(9), pp.21989-22002.

## References

57. Goetz, A. F., & Rowan, L. C. (1981). Geologic remote sensing. *Science*, 211(4484), 781-791.
58. Goetz, A. F., Vane, G., Solomon, J. E., & Rock, B. N. (1985). Imaging spectrometry for earth remote sensing. *Science*, 228(4704), 1147-1153.
59. Goetz, S. J., Steinberg, D., Betts, M. G., Holmes, R. T., Doran, P. J., Dubayah, R., & Hofton, M. (2010). LiDAR remote sensing variables predict breeding habitat of a Neotropical migrant bird. *Ecology*, 91(6), 1569-1576.
60. Goswami, J.N. and Annadurai, M., 2009. Chandrayaan-1: India's first planetary science mission to the moon. *Current Science*, pp.486-491.
61. Guoliang Zhao, "Research on Laser Scanner Applied for Landslide Monitoring in West Mining Areas," *MINE SURVEYING*, pp.29-31, June 2009.
62. Haboudane, D., Miller, J.R., Pattey, E., Zarco-Tejada, P.J. and Strachan, I.B., 2004. Hyperspectral vegetation indices and novel algorithms for predicting green LAI of crop canopies: Modeling and validation in the context of precision agriculture. *Remote sensing of environment*, 90(3), pp.337-352.
63. Hakala, T., Suomalainen, J., Kaasalainen, S. and Chen, Y., 2012. Full waveform hyperspectral LiDAR for terrestrial laser scanning. *Optics express*, 20(7), pp.7119-7127.
64. Hare, E.W., Miller, J.R. and Edwards, G.R., 1984, August. Studies of the vegetation red reflectance edge in geobotanical remote sensing in eastern Canada. In *Proceedings of the 9th Canadian Symposium on Remote Sensing* (pp. 433-440). Ottawa: Canadian Aeronautics and Space Institute.
65. Hartzell, P., Glennie, C., Biber, K. and Khan, S., 2014. Application of multispectral LiDAR to automated virtual outcrop geology. *ISPRS Journal of Photogrammetry and Remote Sensing*, 88, pp.147-155.
66. Hamzeh, S., Naseri, A. A., Alavipanah, S. K., Mojaradi, B., Bartholomeus, H. M., Clevers, J. G., & Behzad, M. (2013). Estimating salinity stress in sugarcane fields with spaceborne hyperspectral vegetation indices. *International Journal of Applied Earth Observation and Geoinformation*, 21, 282-290.
67. Hodgetts, D. (2013). Laser scanning and digital outcrop geology in the petroleum industry: a review. *Marine and Petroleum Geology*, 46, 335-354.
68. Horler, D. N. H., Dockray, M., and Barber, J., 1983, The red edge of plant leaf reflectance. *International Journal of Remote Sensing*, 4, 273±288.
69. Huang S, Siegert F (2006) Land cover classification optimized to detect areas at risk of desertification in North China based on SPOT VEGETATION imagery. *J Arid Environ* 67:308–27.
70. Huang, Y., Yu, B., Zhou, J., Hu, C., Tan, W., Hu, Z., & Wu, J. (2013). Toward automatic estimation of urban green volume using airborne LiDAR data and high resolution Remote Sensing images. *Frontiers of Earth Science*, 7(1), 43-54.
71. Hunt G R. Spectral signatures of particulate minerals in the visible and near infrared[J]. *Geophysics*, 1977, 42(3): 501-513.
72. Hyyppä H, Hyyppä J. Comparing the accuracy of laser scanner with other optical remote sensing data sources for stand attribute retrieval[J]. *The photogrammetric journal of Finland*, 1999, 16(2): 5-15. (1999 a)
73. Hyyppä, J. (1999). Detecting and estimating attributes for single trees using laser scanner. *Photogramm J Finland*, 16, 27-42. (1999 b)
74. Hyyppä, J., Yu, X., Rönholm, P., Kaartinen, H., & Hyyppä, H. (2003). Factors affecting object-oriented forest growth estimates obtained using laser scanning. *The photogrammetric journal of Finland*, 18, 16-31.
75. Höfle, B. and Pfeifer, N., 2007. Correction of laser scanning intensity data: Data and model-driven approaches. *ISPRS journal of photogrammetry and remote sensing*, 62(6), pp.415-433
76. H. Araki, S. Tazawa, H. Noda, et al., Lunar global shape and polar topography derived from Kaguya-LALT laser altimetry, *Science* 323 (5916) (2009) 897–900.
77. Irish, J. L., & Lillycrop, W. J. (1999). Scanning laser mapping of the coastal zone: the SHOALS system. *ISPRS Journal of Photogrammetry and Remote Sensing*, 54(2-3), 123-129.

78. Jacquemoud, S., Bacour, C., Poilve, H., & Frangi, J. P. (2000). Comparison of four radiative transfer models to simulate plant canopies reflectance: Direct and inverse mode. *Remote Sensing of Environment*, 74(3), 471-481.
79. Jiang, C., Chen, Y., Wu, H., Li, W., Zhou, H., Bo, Y., ... & Hyypää, J. (2019). Study of a high spectral resolution hyperspectral LiDAR in vegetation red edge parameters extraction. *Remote Sensing*, 11(17), 2007.
80. Johnson, A. E., Klumpp, A., Collier, J., & Wolf, A. (2001). LiDAR-based hazard avoidance for safe landing on Mars.
81. Johnson, B.; Joseph, R.; Nischam, M.; Newbury, A.; Kerekes, J.; Barclay, H.; Willard, B.; and Zayhowski, J.J. A compact, active hyperspectral imaging system for the detection of concealed targets. *Proc. SPIE 1999*, 3710, 144-153.
82. Jones, T. G., Coops, N. C., & Sharma, T. (2010). Assessing the utility of airborne hyperspectral and LiDAR data for species distribution mapping in the coastal Pacific Northwest, Canada. *Remote Sensing of Environment*, 114, 2841-2852.
83. Kaartinen H. Benchmarking of airborne laser scanning based feature extraction methods and mobile laser scanning system performance based on high-quality test fields, Finnish Geodetic Institute, 2013.
84. Kaasalainen, Sanna, Eero Ahokas, Juha Hyypää, and Juha Suomalainen. "Study of surface brightness from backscattered laser intensity: Calibration of laser data." *IEEE Geoscience and Remote Sensing Letters* 2, no. 3 (2005): 255-259
85. Kaasalainen, S., Hyypää, J., Litkey, P., Hyypää, H., Ahokas, E., Kukko, A. and Kaartinen, H., 2007. Radiometric calibration of ALS intensity. *Int. Arch. Photogramm. Remote Sens*, 36, pp.201-205. (Kaasalainen 2007a)
86. Kaasalainen, S.; Lindroos, T.; Hyypää, J. Toward hyperspectral LiDAR - Measurement of spectral backscatter intensity with a supercontinuum laser source. *IEEE Geosci. Remote Sens. Lett.* 2007,4, 211-215. (Kaasalainen 2007b)
87. Kaasalainen, S., Lindroos, T. and Hyypää, J., 2007. Toward hyperspectral LiDAR: Measurement of spectral backscatter intensity with a supercontinuum laser source. *IEEE Geoscience and Remote Sensing Letters*, 4(2), pp.211-215. (Kaasalainen 2007c)
88. Kaasalainen, Sanna, et al. "Radiometric calibration of LIDAR intensity with commercially available reference targets." *IEEE Transactions on Geoscience and Remote Sensing* 47.2 (2009): 588-598.
89. Kamalakar, J.A., Prasad, A.S., Bhaskar, K.V.S., Selvaraj, P., Venkateswam, R., Raja, V.S., Kalyani, K., Goswami, A. and Ravikumar, K., 2010. Design, development and performance of a laser ranging instrument onboard Chandrayaan-1. *Journal of Spacecraft Technology*, 20(1), pp.13-24.
90. Karila K, Matikainen L, Puttonen E, Hyypää J. Feasibility of multispectral airborne laser scanning data for road mapping. *IEEE Geoscience and Remote Sensing Letters*. 2017 Jan 23;14(3):294-8.
91. Ke, Y., Quackenbush, L. J., & Im, J. (2010). Synergistic use of QuickBird multispectral imagery and LIDAR data for object-based forest species classification. *Remote Sensing of Environment*, 114, 1141-1154
92. Klemas, V. (2011). Remote sensing of wetlands: case studies comparing practical techniques. *Journal of Coastal Research*, 27(3), 418-427.
93. Kohlbrecher, S., Meyer, J., von Stryk, O. and Klingauf, U., 2011. A flexible and scalable slam system with full 3d motion estimation. In: *Proc. IEEE International Symposium on Safety, Security and Rescue Robotics (SSRR)*, IEEE.
94. Kokaly, R. F., Asner, G. P., Ollinger, S. V., Martin, M. E., & Wessman, C. A. (2009). Characterizing canopy biochemistry from imaging spectroscopy and its application to ecosystem studies. *Remote Sensing of Environment*, 113, S78-S91.
95. Konolige, K., Grisetti, G., Kummerle, R., Burgard, W., Limketkai, B. and Vincent, R., 2010. Efficient sparse pose adjustment for 2d mapping. In: *Intelligent Robots and Systems (IROS)*, 2010 IEEE/RSJ International Conference on, IEEE, pp. 22-29.

## References

96. Kraus, K., & Pfeifer, N. (1998). Determination of terrain models in wooded areas with airborne laser scanner data. *ISPRS Journal of Photogrammetry and Remote Sensing*, 53(4), 193-203.
97. Kukkonen, M., Maltamo, M., Korhonen, L. and Packalen, P., 2019. Comparison of multispectral airborne laser scanning and stereo matching of aerial images as a single sensor solution to forest inventories by tree species. *Remote Sensing of Environment*, 231, p.111208.
98. Kurz, T.H., Buckley, S.J. and Howell, J.A., 2013. Close-range hyperspectral imaging for geological field studies: workflow and methods. *International Journal of Remote Sensing*, 34(5), pp.1798-1822.
99. Langley SK, Cheshire HM, Humes KS (2001) A comparison of single date and multitemporal satellite image classifications in a semi-arid grassland. *J Arid Environ* 49:401–11.
100. Lefsky, M. A., Cohen, W. B., Parker, G. G., & Harding, D. J. (2002). LiDAR remote sensing for ecosystem studies: LiDAR, an emerging remote sensing technology that directly measures the three-dimensional distribution of plant canopies, can accurately estimate vegetation structural attributes and should be of particular interest to forest, landscape, and global ecologists. *BioScience*, 52(1), 19-30.
101. Li, W., Sun, G., Niu, Z., Gao, S., & Qiao, H. (2014). Estimation of leaf biochemical content using a novel hyperspectral full-waveform LiDAR system. *Remote sensing letters*, 5(8), 693-702.
102. Li L, Ustin SL, Lay M (2005) Application of multiple endmember spectral mixture analysis (MESMA) to AVIRIS imagery for coastal salt marsh mapping: a case study in China Camp, CA, USA. *Int J Remote Sens* 26:5193–207.
103. Li, J.M.; Zhou, M.; Li, C. R. "Research on Point Cloud Calculation Method of Airborne Linear Array Push-broom LiDAR." *Remote Sensing Technology and Application*, 2013, 28(6), 1033-1038.
104. Li, W., Jiang, C., Chen, Y., Hyypä, J., Tang, L., Li, C., & Wang, S. W. (2018). A Liquid Crystal Tunable Filter-Based Hyperspectral LiDAR System and Its Application on Vegetation Red Edge Detection. *IEEE Geoscience and Remote Sensing Letters*.
105. Link, L. E. (1969, October). Capability of airborne laser profilometer to measure terrain roughness. In *Proceedings, 6th Symposium on Remote Sensing of Environment* (pp. 189-196).
106. Little, M. J. (2006, April). Slope monitoring strategy at PPRust open pit operation. In *Proceedings of the international symposium on stability of rock slopes in open pit mining and civil engineering* (pp. 211-230). Johannesburg: Southern African Institute of Mining and Metallurgy.
107. Liu, F., Kong, W., & He, Y. (2011). Nondestructive estimation of nitrogen status and vegetation index of oilseed rape canopy using multi-spectral imaging technology. *Sensor Letters*, 9(3), 1126-1132.
108. Lorena, A. C., & De Carvalho, A. C. (2008). Evolutionary tuning of SVM parameter values in multiclass problems. *Neurocomputing*, 71(16-18), 3326-3334.
109. Malkamäki, T., Kaasalainen, S., & Ilinca, J. (2019). Portable hyperspectral LiDAR utilizing 5 GHz multichannel full waveform digitization. *Optics Express*, 27(8), A468-A480.
110. Manninen, A., Kääriäinen, T., Parviainen, T., Buchter, S., Heiliö, M. and Laurila, T., 2014. Long distance active hyperspectral sensing using high-power near-infrared supercontinuum light source. *Optics express*, 22(6), pp.7172-7177.
111. Martin, M. E., Newman, S. D., Aber, J. D., & Congalton, R. G. (1998). Determining forest species composition using high spectral resolution remote sensing data. *Remote Sensing of Environment*, 65(3), 249-254.
112. Maselli, F. and Chiesi, M., 2006. Integration of multi-source NDVI data for the estimation of Mediterranean forest productivity. *International Journal of Remote Sensing*, 27(1), pp.55-72.
113. Matikainen, L., Karila, K., Hyypä, J., Litkey, P., Puttonen, E., & Ahokas, E. (2017). Object-based analysis of multispectral airborne laser scanner data for land cover classification and map updating. *ISPRS Journal of Photogrammetry and Remote Sensing*, 128, 298-313.

114. Meyera, P., Staenzb, K., & Ittena, K. I. (1996). Semi-automated procedures for tree species identification in high spatial resolution data from digitized colour infrared-aerial photography. *ISPRS Journal of Photogrammetry and Remote Sensing*, 51(1), 5-16.
115. Miller, J.R., Hare, E.W. and Wu, J., 1990. Quantitative characterization of the vegetation red edge reflectance 1. An inverted-Gaussian reflectance model. *Remote Sensing*, 11(10), pp.1755-1773.
116. Morsdorf, F., C. Nichol, T. Malthus, and I. H. Woodhouse. 2009. "Assessing Forest Structural and Physiological Information Content of Multi-Spectral LiDAR Waveforms by Radiative Transfer Modelling." *Remote Sensing of Environment* 113: 2152–2163. DOI:10.1016/j.rse.2009.05.019.
117. Morsy, S., Shaker, A., & El-Rabbany, A. (2017). Multispectral LiDAR data for land cover classification of urban areas. *Sensors*,17(5), 958-.
118. Muirhead, K., & Cracknell, A. P. (1986). Airborne LiDAR bathymetry. *International Journal of Remote Sensing*, 7(5), 597-614.
119. Muller J; Yuen PC. *Imaging LiDAR Simulator Interface*, NERC-CEOI: Hyperspectral Imaging LiDAR (LADAR).2008
120. Murphy, R.J., Monteiro, S.T. and Schneider, S., 2012. Evaluating classification techniques for mapping vertical geology using field-based hyperspectral sensors. *IEEE Transactions on Geoscience and Remote Sensing*, 50(8), pp.3066-3080.
121. Nag, S., Hewagama, T., Georgiev, G. T., Pasquale, B., Aslam, S., & Gatebe, C. K. (2017). Multispectral snapshot imagers onboard small satellite formations for multi-angular remote sensing. *IEEE Sensors Journal*, 17(16), 5252-5268.
122. Nelson, R., Krabill, W., & MacLean, G. (1984). Determining forest canopy characteristics using airborne laser data. *Remote Sensing of Environment*, 15(3), 201-212.
123. Naesset, E. (1997). Estimating timber volume of forest stands using airborne laser scanner data. *Remote Sensing of Environment*, 61(2), 246-253.
124. Nevalainen, O., Hakala, T., Suomalainen, J., Mäkipää, R., Peltoniemi, M., Krooks, A., & Kaasalainen, S. (2014). Fast and nondestructive method for leaf level chlorophyll estimation using hyperspectral LiDAR. *Agricultural and Forest Meteorology*, 198, 250-258.
125. Ni-Meister, W., Lee, S., Strahler, A. H., Woodcock, C. E., Schaaf, C., Yao, T., ... & Blair, J. B. (2010). Assessing general relationships between aboveground biomass and vegetation structure parameters for improved carbon estimate from LiDAR remote sensing. *Journal of Geophysical Research: Biogeosciences*, 115(G2).
126. Nordberg ML, Evertson J (2003) Vegetation index differencing and linear regression for change detection in a Swedish mountain range using Landsat TM and ETM+ imagery. *Land Degradation & Development* 16:139–149.
127. Oparin, V. N., Seredovich, V. A., Yushkin, V. F., Ivanov, A. V., & Prokop'eva, S. A. (2007). Application of laser scanning for developing a 3D digital model of an open-pit side surface. *Journal of Mining Science*, 43(5), 545-554.
128. Palamara, D. R., Nicholson, M., Flentje, P., Baafi, E., & Brassington, G. M. (2007). An evaluation of airborne laser scan data for coalmine subsidence mapping. *International Journal of Remote Sensing*, 28(15), 3181-3203.
129. Pan S, Guan H, Yu Y, Li J, Peng D, 2019. A comparative land-cover classification feature study of learning algorithms: DBM, PCA and RF using multispectral LiDAR data, *IEEE Journal of Selected Topics in Applied Earth Observations and Remote Sensing*, 12(4), 1314-1326.
130. Penasa, L., Franceschi, M., Preto, N., Teza, G., & Polito, V. (2014). Integration of intensity textures and local geometry descriptors from Terrestrial Laser Scanning to map chert in outcrops. *ISPRS Journal of Photogrammetry and Remote Sensing*, 93, 88-97.
131. Peñuelas, J., Filella, I., Biel, C., Serrano, L. and Save, R., 1993. The reflectance at the 950–970 nm region as an indicator of plant water status. *International journal of remote sensing*, 14(10), pp.1887-1905.
132. Pfennigbauer M, Ullrich A. Multi-wavelength airborne laser scanning[C]//Proceedings of the International LiDAR Mapping Forum, ILMF, New Orleans. 2011.

133. Popescu, S.C., Wynne, R.H. and Scrivani, J.A., 2004. Fusion of small-footprint LiDAR and multispectral data to estimate plot-level volume and biomass in deciduous and pine forests in Virginia, USA. *Forest Science*, 50(4), pp.551-565.
134. Pu R L, et al. "Extraction of red edge optical parameters from Hyperion data for estimation of forest leaf area index." *IEEE Transactions on Geoscience & Remote Sensing*, vol. 41, no. 4, pp. 916-921, Apr. 2003.
135. Purkis, S. and Klemas, V., 2011. *Remote Sensing and Global Environmental Change*. Oxford: Wiley-Blackwell.
136. Puttonen, E. (2012). *Tree Species Classification with Multiple Source Remote Sensing Data*.
137. Puttonen E, Hakala T, Nevalainen O, Kaasalainen S, Krooks A, Karjalainen M, and Anttila K, "Artificial target detection with a hyperspectral LiDAR over 26-h measurement." *Opt. Eng.*, vol. 54, no.1, Jan. 2015.
138. Ramsey, E., 1995. Monitoring flooding in coastal wetlands by using radar imagery and ground-based measurements. *International Journal of Remote Sensing*, 16, 2495-2502.
139. Rautiainen, M., Nilson, T., & Lökk, T. (2009). Seasonal reflectance trends of hemiboreal birch forests. *Remote Sensing of Environment*, 113(4), 805-815.
140. Rosso, P.H., Ustin, S.L. and Hastings, A., 2005. Mapping marshland vegetation of San Francisco Bay, California, using hyperspectral data. *International Journal of Remote Sensing*, 26(23), pp.5169-5191.
141. Schlerf, M., Atzberger, C., & Hill, J. (2005). Remote sensing of forest biophysical variables using HyMap imaging spectrometer data. *Remote Sensing of Environment*, 95(2), 177-194.
142. Schreier, H., Loughheed, J., Tucker, C., & Leckie, D. (1985). Automated measurements of terrain reflection and height variations using an airborne infrared laser system. *International Journal of Remote Sensing*, 6(1), 101-113.
143. Schroeder TA, Canty MJ, Yang Z, et al. (2006) Radiometric correction of multi-temporal Landsat data for characterization of early successional forest patterns in western Oregon. *Remote Sens Environ* 103:16-26.
144. Shafri, H. Z., & Hamdan, N. (2009). Hyperspectral imagery for mapping disease infection in oil palm plantation using vegetation indices and red edge techniques. *American Journal of Applied Sciences*, 6(6), 1031.
145. Shao H, Chen Y, Yang Z, Jiang C, Li W, Wu H, Wen Z, Wang S, Puttnon E, Hyyppä J. A 91-Channel Hyperspectral LiDAR for Coal/Rock Classification. *IEEE Geoscience and Remote Sensing Letters*. 2019 Sep 12.
146. Sheng, Y. H., Zhang, K., Zhang, K., & Wang, Y. B., (2010). Seamless multi station merging of terrestrial laser scanned 3D point clouds. *Journal of China University of Mining & Technology*, 39(2), 233-237.
147. Shuang, L. (2011). Application of 3D Laser Scanning Technology in Difficult Arrival Region Survey of Coal Gangue Dump [J]. *Site Investigation Science and Technology*, 3.
148. Sjogren, W. L., & Wollenhaupt, W. R. (1973). Lunar shape via the Apollo laser altimeter. *Science*, 179(4070), 275-278.
149. Slob, S., Hack, R., van Knapen, B., & Kemeny, J. (2004, October). Automated identification and characterization of discontinuity sets in outcropping rock masses using 3D terrestrial laser scan survey techniques. In *Proceedings of the ISRM regional symposium EUROCK* (pp. 439-443).
150. Slob, S., Van Knapen, B., Hack, R., Turner, K., & Kemeny, J. (2005). Method for automated discontinuity analysis of rock slopes with three-dimensional laser scanning. *Transportation Research Record*, 1913(1), 187-194.
151. Slob, S., Hack, H.R.G.K., Feng, Q., Röshoff, K. and Turner, A.K., 2007, August. Fracture mapping using 3D laser scanning techniques. In *Proceedings of the 11th Congress of the International Society for Rock Mechanics*, Lisbon, Portugal (Vol. 1, pp. 299-302).
152. Smith, D.E., Zuber, M.T., Neumann, G.A., Mazarico, E., Lemoine, F.G., Head III, J.W., Lucey, P.G., Aharonson, O., Robinson, M.S., Sun, X. and Torrence, M.H., 2017. Summary of the results from the lunar orbiter laser altimeter after seven years in lunar orbit. *Icarus*, 283, pp.70-91.

153. Sturzenegger, M., & Stead, D. (2009). Close-range terrestrial digital photogrammetry and terrestrial laser scanning for discontinuity characterization on rock cuts. *Engineering Geology*, 106(3-4), 163-182.
154. Sturzenegger, M., Yan, M., Stead, D., & Elmo, D. (2007, May). Application and limitations of ground-based laser scanning in rock slope characterization. In *Proceedings of the first Canadian US rock mechanics symposium* (Vol. 1, pp. 29-36).
155. St-Onge, B.; Budei, B.C. Individual tree species identification using the multispectral return intensities of the Optech Titan LiDAR system. In *Proceedings of the SilviLaser 2015, La Grand Motte, France, 28–30 September 2015*; pp. 71–73.
156. Sun, G., Niu, Z., Gao, S., Huang, W., Wang, L., Li, W., & Feng, M. (2014, November). 32-channel hyperspectral waveform LiDAR instrument to monitor vegetation: design and initial performance trials. In *Multispectral, Hyperspectral, and Ultraspectral Remote Sensing Technology, Techniques and Applications V* (Vol. 9263, p. 926331). International Society for Optics and Photonics.
157. Sun, J., Shi, S., Gong, W., Yang, J., Du, L., Song, S., Chen, B. and Zhang, Z., 2017. Evaluation of hyperspectral LiDAR for monitoring rice leaf nitrogen by comparison with multispectral LiDAR and passive spectrometer. *Scientific Reports*, 7, p.40362.
158. Sun, X. et al. HgCdTe avalanche photodiode detectors for airborne and spaceborne LiDAR at infrared wavelengths. *Optics Express* 25, 16589, (2017).
159. Sun, Z., Martinez, A. & Wang, F. Optical modulators with two-dimensional layered materials. *Nature Photonics* 10, 227 - 238, (2016).
160. Tabirian A M, Jenssen H P, Buchter S, et al. Multi-wavelengths infrared laser: U.S. Patent 6,567,431[P]. 2003-5-20.
161. Tong, X., Liu, X., Chen, P., Liu, S., Luan, K., Li, L., ... & Hong, Z. (2015). Integration of UAV-based photogrammetry and terrestrial laser scanning for the three-dimensional mapping and monitoring of open-pit mine areas. *Remote Sensing*, 7(6), 6635-6662.
162. Tooma Jr, S. G., & Tucker, W. B. (1971). Statistical comparison of airborne laser and stereophotogrammetric sea ice profiles. *Remote Sensing of Environment*, 2, 261-272.
163. Townshend, J., Justice, C., Li, W., Gurney, C., & McManus, J. (1991). Global land cover classification by remote sensing: present capabilities and future possibilities. *Remote Sensing of Environment*, 35(2-3), 243-255.
164. Van Aardt, J. A. (2000). Spectral separability among six southern tree species (Doctoral dissertation, Virginia Tech).
165. Van Rees, E. (2015). The first multispectral airborne LiDAR sensor. *GeoInformatics*, 18(1), 10.
166. Varshney, P.K. and Arora, M.K., 2004. *Advanced image processing techniques for remotely sensed hyperspectral data*. Springer Science & Business Media.
167. Vauhkonen, J., Hakala, T., Suomalainen, J., Kaasalainen, S., Nevalainen, O., Vastaranta, M., ... & Hyypä, J. (2013). Classification of spruce and pine trees using active hyperspectral LiDAR. *IEEE Geoscience and Remote Sensing Letters*, 10(5), 1138-1141.
168. Volker, W., Bremer, M., Joachim, L., Martin, R., Christian, G., & Frederic, P. M. . (2015). Evaluating the potential of multispectral airborne LiDAR for topographic mapping and land cover classification. *Geospatial Week, Laserscanning Workshop*.
169. Vosselman, G. (2000). Slope based filtering of laser altimetry data. *International Archives of Photogrammetry and Remote Sensing*, 33(B3/2; PART 3), 935-942.
170. Wagner, W., Hollaus, M., Briese, C., & Ducic, V. (2008). 3D vegetation mapping using small-footprint full-waveform airborne laser scanners. *International Journal of Remote Sensing*, 29(5), 1433-1452.
171. Wan, X., Shu, R., & Huang, G. (2013). Effects of rocket engines on laser during lunar landing. *Physics Letters A*, 377(38), 2598-2603.
172. Wang C K, Tseng Y H, and Chu H J. "Airborne Dual-Wavelength LiDAR Data for Classifying Land Cover." *Remote Sensing*, vol.6, no.1, pp. 700-715, Jan 2014.
173. Wang, C. K., & Philpot, W. D. (2007). Using airborne bathymetric LiDAR to detect bottom type variation in shallow waters. *Remote Sensing of Environment*, 106(1), 123-135.

## References

174. Wang, J., Shu, R., Chen, W., Jia, J., Wang, B., Huang, G., Hu, Y. and Hou, X., 2010. Laser altimeter of CE-1 payloads system. *Science China Physics, Mechanics and Astronomy*, 53(10), pp.1914-1920.
175. Wang, S. W., Xia, C., Chen, X., Lu, W., Li, M., Wang, H., ... & Zhang, T. (2007). Concept of a high-resolution miniature spectrometer using an integrated filter array. *Optics Letters*, 32(6), 632-634.
176. Wang, Z., Chen, Y., Li, C., Tian, M., Zhou, M., He, W., ... & Zhou, H. (2018, July). A Hyperspectral LiDAR with Eight Channels Covering from VIS to SWIR. In *IGARSS 2018-2018 IEEE International Geoscience and Remote Sensing Symposium* (pp. 4293-4296). IEEE.
177. Wang, Z., Sang, T., Wang, L., Jiao, H., Wu, Y., Zhu, J., ... & Lu, W. (2008). Narrowband multichannel filters and integrated optical filter arrays. *Applied Optics*, 47(13), C1-C8.
178. Wallace, A. M., McCarthy, A., Nichol, C. J., Ren, X., Morak, S., Martinez-Ramirez, D., ... Buller, G. S. (2014). Design and evaluation of multispectral LiDAR for the recovery of arboreal parameters. *IEEE Transactions on Geoscience and Remote Sensing*, 52(8), 4942-4954.
179. Wehr, A., & Lohr, U. (1999). Airborne laser scanning—an introduction and overview. *ISPRS Journal of photogrammetry and remote sensing*, 54(2-3), 68-82.
180. Williams, K.K. and Zuber, M.T., 1998. Measurement and analysis of lunar basin depths from Clementine altimetry. *Icarus*, 131(1), pp.107-122.
181. Woodhouse, I.H., Nichol, C., Sinclair, P., Jack, J., Morsdorf, F., Malthus, T.J. and Patenaude, G., 2011. A multispectral canopy LiDAR demonstrator project. *IEEE Geoscience and Remote Sensing Letters*, 8(5), pp.839-843.
182. Yang, J., & Artigas, F. J. (2010). Mapping salt marsh vegetation by integrating hyperspectral and LiDAR remote sensing. *Remote Sensing of Coastal Environment*, 173-190.
183. Yu, X., Hyyppä, J., Kaartinen, H., & Maltamo, M. (2004). Automatic detection of harvested trees and determination of forest growth using airborne laser scanning. *Remote Sensing of Environment*, 90(4), 451-462.
184. Zhang, H., Wang, J., Shu, R., Hu, Y. and Fang, K., 2006, February. Optical system integration of near infrared laser altimeter. In *2nd International Symposium on Advanced Optical Manufacturing and Testing Technologies: Optical Test and Measurement Technology and Equipment* (Vol. 6150, p. 61503E). International Society for Optics and Photonics.
185. Zhang, H.; Wu, H.; Zhang, D. "Application of high-precision matching about multisensor in fast stereo imaging." *Sensors, Systems, and Next-Generation Satellites XIX*. International Society for Optics and Photonics, 2015
186. Zhao, J., Huang, J., Qiao, L., Xiao, Z., Huang, Q., Wang, J., He, Q. and Xiao, L., 2014. Geologic characteristics of the Chang'E-3 exploration region. *Science China Physics, Mechanics and Astronomy*, 57(3), pp.569-576.
187. Zeng, X., Rao, P., DeFries, R.S. and Hansen, M.C., 2003. Interannual variability and decadal trend of global fractional vegetation cover from 1982 to 2000. *Journal of Applied Meteorology*, 42(10), pp.1525-1530.
188. Zhou, H., Chen, Y., Hyyppä, J., & Li, S. (2017). An overview of the laser ranging method of space laser altimeter. *Infrared Physics & Technology*, 86, 147-158.
189. Zhu, X., & Liu, D. (2014). Accurate mapping of forest types using dense seasonal Landsat time-series. *ISPRS Journal of Photogrammetry and Remote Sensing*, 96, 1-11



ISBN 978-952-64-0076-1 (printed)  
ISBN 978-952-64-0077-8 (pdf)  
ISSN 1799-4934 (printed)  
ISSN 1799-4942 (pdf)

**Aalto University**  
**School of Science**  
**Department of Computer Science**  
[www.aalto.fi](http://www.aalto.fi)

**BUSINESS +  
ECONOMY**

**ART +  
DESIGN +  
ARCHITECTURE**

**SCIENCE +  
TECHNOLOGY**

**CROSSOVER**

**DOCTORAL  
DISSERTATIONS**